Experimental Analysis of Transient Water Fluxes in PEM Fuel Cells

by

James Richard Kracher

A thesis submitted in partial fulfillment of the requirements for the degree of

Master of Science

Department of Mechanical Engineering

University of Alberta

Abstract

Understanding the movement of water within a polymer electrolyte membrane (PEM) fuel cell is critical for improving performance at high loads. In this work, an experimental setup was designed and assembled for monitoring the in situ distribution of water contained within the anode and cathode of an operating PEM fuel cell. Relative humidity, temperature, and pressure sensors, housed within a heated water bath, characterize the water vapour levels evaporated in the reactant streams entering and leaving an operational fuel cell to provide transient measurements of the net movement of water across the PEM in addition to correlating operating anomalies with two-phase flow.

Manufacturer accuracies were propagated with experimental uncertainties calculated from auxiliary experiments to estimate the setup's overall ability to correctly identify the water content of a gas stream, found to be $\leq$12.9%. Experimental validation comparing to conventional water collection techniques employed extensively in literature demonstrate the setup can successfully reproduce net crossover flux magnitudes and trends identified in other publications as well as reconcile the cumulative amount of water entering and leaving the cell.

The setup was then used to investigate the effects of adding a microporous layer (MPL) to the net crossover flux across 5 cm^2 membrane electrode assemblies with varying Nafion membrane thicknesses. The addition of a single MPL to the cathode significantly improved performance in the mass transport region. Results indicated MPLs have negligible impact on electronic resistances and instead encourage the transport of water across the PEM in the direction normal to the MPL. All tested

membranes showed an increase in water transport towards the anode when the cathode was assembled with an MPL with thinner membranes exhibiting higher crossovers. Unprecedented high current densities for low loaded electrodes with NR211 membranes were achievable after the addition of an MPL to the cathode and by increasing the anode flow rate to accelerate convective drying, thereby establishing a concentration gradient that increased back diffusion and mitigated flooding in the cathode.

Keywords: PEM fuel cell, water transport, transient, net crossover flux, microporous layer, two-phase flow

Dedicated to my parents

Acknowledgements

I would like to thank Dr. Marc Secanell for awarding me this opportunity, for his unwavering academic and financial support, but above all, for his mentorship and friendship. It has been a privilege and a pleasure to work under his guidance for my Master's degree. To my colleagues, thank you for making this an amazing experience I will never forget. You have always been there for support, whether its a difficult problem or a difficult time. I look forward to what our future may bring. I am grateful for the University of Alberta, which has been my academic home for the past eight years, and for the support staff and technicians whose invaluable experience and behind-the-scenes assistance made this possible. And most importantly, to my family, a thank you is not enough. You are behind every written word. None of this would be possible without you.

Table of Contents

List of Tables

List of Figures

Chapter 1

Introduction

1.1 Background and Motivation

The desire to reduce particulate and greenhouse gas emissions has led to the development of several alternative energy conversion technologies. In stationary and transportation applications, Canadian scientists and industrial researchers have shown polymer electrolyte membrane fuel cells (PEMFCs), fuelled with hydrogen, could be used to displace diesel generators and internal combustion engines while achieving zero local emissions. PEMFCs benefits include high efficiency, high power density, quick startup capabilities, and low operating temperatures [1].

Originally developed as part of NASA's Gemini missions, PEMFC technology fell out of favour after unsettled issues impeded their performance. They experienced renewed interest from the late 1980's to the present after the economic climate and public opinion emphasized the need for alternative domestic energy solutions [2]. Currently, they have been implemented in transportation applications, such as vehicles and buses, standalone stationary power solutions, and small scale combined heat and power systems [3].

Figure 1.1 illustrates a single PEMFC during operation. Pure hydrogen gas is introduced into the anodic bipolar plate and passed through a flow field of small channels providing access to the gas diffusion layer (GDL). The GDL is a porous media comprised of electrically conductive carbon fibres and is designed to evenly distribute the gas to the catalyst layer (CL), transfer the charge and heat from the CL to the current collectors, and wick condensed water built up within the layers. Pressed against the GDL, is the catalyst layer. Recently, this interface has also included an intermediate microporous layer (MPL) [4], constructed from carbon black powder and a hydrophobic agent. Although the mechanisms are disputed, the smaller pore network of the MPL and hydrophobicity of the pores are intended to improve water

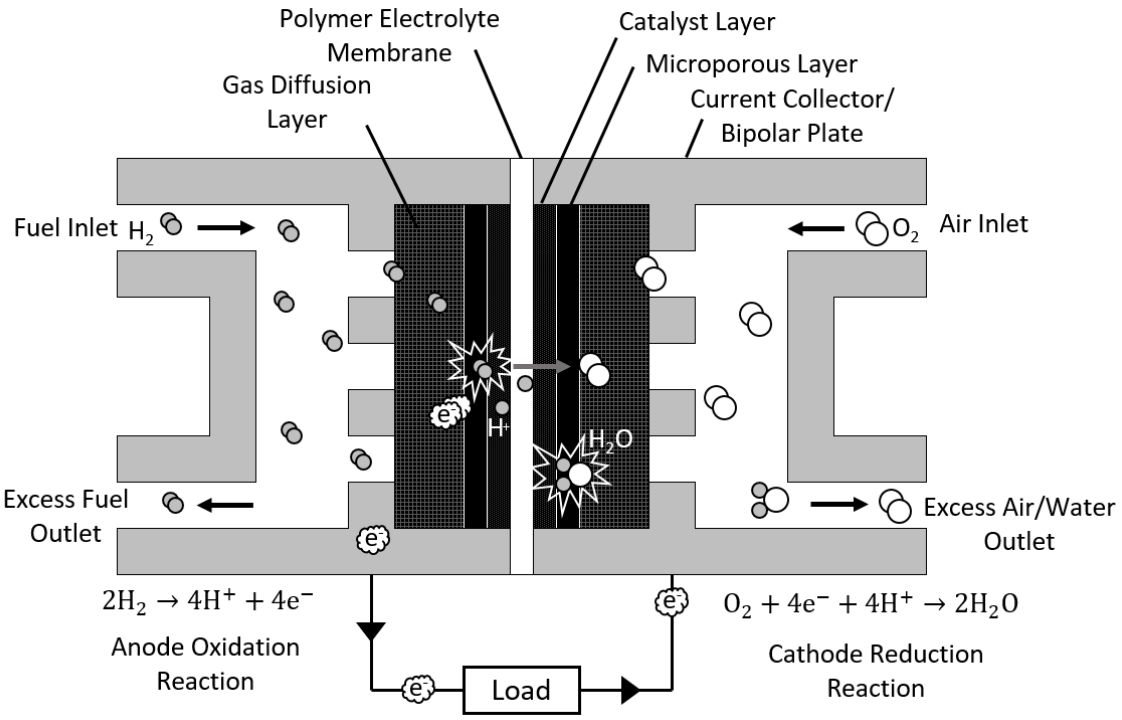

Figure 1.1 – Electrochemical operation and structure of a PEMFC

management and reduce contact resistance [5–7].

The original CLs installed in the Gemini power plants consisted of unsupported platinum deposited onto titanium screens with a loading of 28 mg_{Pt}/cm^2/electrode [2]. Today, conventional CLs are comprised of platinum nanoparticles supported on carbon black using either the GDL or the membrane as a substrate. If the CL is adhered to the GDL, the assembly is referred to as a gas diffusion electrode (GDE) whereas if the CL is adhered to the membrane, the assembly is called a catalyst coated membrane (CCM). Together, they are both considered membrane electrode assemblies (MEA). Improvements in catalyst synthesis and deposition have reduced the expensive platinum loading per electrode to less than 0.2 mg_{Pt}/cm^2 while improving fuel cell performance [1].

The PEMFC electrochemical reaction can be summarized as follows. In the presence of platinum, hydrogen is separated into electrons and protons as per the hydrogen oxidation reaction (HOR),

$$2H_2 \rightleftharpoons 4H^+ + 4e^- \tag{1.1}$$

The protons permeate through the proton conductive and electrically insulating polymer electrolyte membrane (PEM) and the electrons are transferred through the GDL,

towards the current collectors, and passed through a external circuit. The membrane is commonly made of Nafion, an ionomer noted for its unique charge transport properties, and mechanical and chemical stability [8]. The species then reunite at the cathode CL and react with oxygen to form water by means of the oxygen reduction reaction (ORR),

$$O_2 + 4H^+ + 4e^- \rightleftharpoons 2H_2O \tag{1.2}$$

Oxygen is transported to the cathode CL by means of its own flow field and GDL however it is typically supplied as air. The overall reaction for a PEMFC is therefore,

$$2H_2 + O_2 \rightleftharpoons 2H_2O \tag{1.3}$$

The electrochemical consumption or production of each species j, in mol/s, is determined with the application of Faraday's law of electrolysis,

$$\dot{n}_j = \frac{I}{FN_j} \tag{1.4}$$

where I is the current extracted from the cell, F is Faraday's constant (96485 C/mol), correlating total charge to a number of electrons, and N_j is the moles of electrons produced per mole of species j. In a hydrogen PEMFC, N_j is two for hydrogen and water and four for oxygen as per the half cell reactions above. When operating a cell, the required minimum flow rates are supplemented by a factor, called the stoichiometric ratio, to decrease the cell's sensitivity to fuel availability at the reaction sites. Although this improves performance, only a stoich of one is reacted with the rest being waste.

Irreversibilities aside, the theoretical electrical work that can be harnessed from the above reaction is equivalent to the Gibbs free energy released. Considering there are two electrons released for every decomposed hydrogen molecule, the reversible open circuit voltage (OCV) at 1 atm and 25°C is given as,

$$E = -\frac{\Delta\overline{g}}{2F} \tag{1.5}$$

where $-\Delta\overline{g}$ is the change in the Gibbs free energy of formation between the products and reactants. Modifying the equation to correct for the activity, a, of the reactants and products, the temperature, T, at which the reaction occurs, and the final phase of the water, one obtains the Nernst equation,

$$E = E^o + \frac{\Delta\overline{s}}{2F}(T - T^o) + \frac{RT}{2F}\ln\left(\frac{a_{H_2}\, a_{O_2}^{1/2}}{a_{H_2O}}\right) \tag{1.6}$$

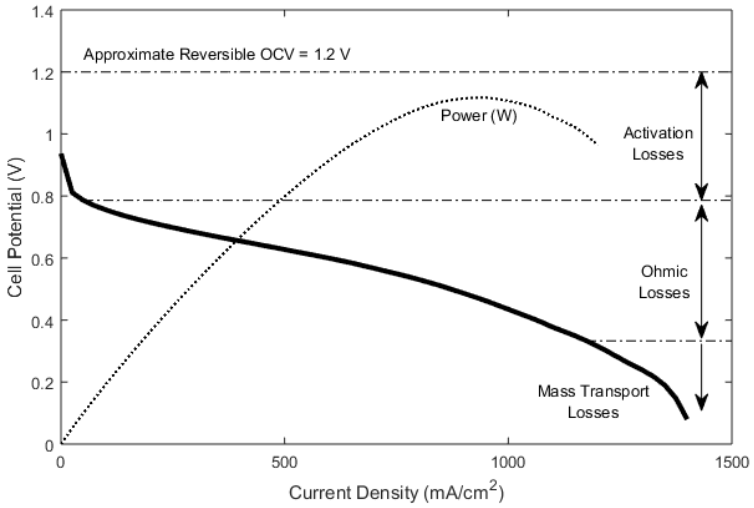

Figure 1.2 – Typical fuel cell polarization curve

where E^o is the open circuit voltage calculated with equation (1.5) at standard conditions, R is the ideal gas constant, and $\Delta\overline{s}$ is the additional entropy generated at the revised temperature.

Fuel cell performance is evaluated by comparing cell voltage with current density to form a polarization curve as shown in Figure 1.2. The curve is characterized by three distinct losses: activation, ohmic, and mass transport. During fuel cell operation, these irreversible losses compound, reducing the cell potential. Each is noted by a distinguishable trend in the polarization curve.

The sharp non-linear initial drop, known as the activation or kinetic loss, results mainly from the sluggishness of the ORR reaction occurring at the cathode electrode [9]. There is a minimum energy threshold that must be overcome before the reaction will occur, amounting to a drop in cell voltage. This can be reduced by increasing the temperature, surface area, reactant concentration, or by selecting a more reactive catalyst.

The following linear region is called the ohmic region phrased after Ohm's law. It arises from the inherent resistances to electron and proton transport of the different fuel cell components and the cumulative contact resistance between each of the components. Reducing the thickness of different parts, selecting better conductive materials, and improving the contact area would minimize ohmic losses.

The latter region, characterized by a sudden non-linear asymptotic fall in cell potential, is a result of mass transport losses. At high current densities, the reaction proceeds faster than fuel can be transported through the porous network and the

reaction begins to starve until it can no longer sustain a potential. In addition to the physical limitation on how much gas can pass through the finite number of pores in the GDL, the accumulation of condensed liquid water in the same pores can further impede mass transport by blocking the pathways essential for gaseous transport. The same principle can be applied to liquid water accumulation in the flow field channels. Increasing pressure and flow rates tend to reduce these losses by increasing the presence of fuel at the reactive sites and improving the volume of water ejected from the cell.

Despite recent advances, PEMFCs continue to be too costly for large-scale commercialization. Platinum, by nature of its properties, prevalence, and status as a commodity, is unaffected by economies of scale, contributing the largest fraction of cost for large production fuel cell systems [10]. In the interest of reducing the overall cost, fuel cell performance must increase while using the same or less expensive catalysts. Efforts to improve PEMFC performance and reduce production costs have all focused on minimizing these three types of losses.

Notably, insufficient water levels are known to reduce the membrane's protonic conductivity while excessive water disrupts gaseous mass transport. Both extremes, which are large contributors to ohmic and mass transport losses, are indicative of the need for an optimized water balance.

1.2 Literature Review

1.2.1 Importance of Water Management

One of the first notable adoptions of PEMFC technology was for NASA's Gemini missions. The technology provided power, heat, and potable water for the crew for extended missions in Earth's orbit as a proof of concept for the penultimate Apollo missions. However, chronic difficulties maintaining adequate water levels inside the polymer membrane prompted NASA to pursue alkaline fuel cells for all subsequent missions. Even in its infancy, poor water management was identified as a limiting factor in PEMFC performance [2].

The mechanisms behind poor performance and dry conditions are well understood [11]. In 1987, Rieke et al. [12] found that proton conductivity of the membrane was influenced by temperature and water content. This was followed up by Zawodzinski et al. [13] in 1993, who measured a variety of transport properties of Nafion membranes with different absorbed water contents and concluded the protonic conductivity increased linearly with increasing water content; matching results reported

earlier by Pourcelly et al. [14]. Reduced membrane conductivity or equivalently, a higher resistivity, translates into increased cell voltage losses, as framed by Ohm's law, i.e.,

$$\Delta V = I\ R \tag{1.7}$$

Zhang et al. [15] experimentally supported Zawodzinski's conclusions after the cell performance was shown to significantly decrease with a reduction of the humidity of the gases entering the cell, credited as a drop in the amount of water introduced into the cell. In addition to a higher membrane resistance, the reaction kinetics were also found to have slowed, later attributed to a restructuring of the ionomer's PTFE backbone under dry conditions [16].

Dry operating conditions have also been linked to long-term performance loss due to both chemical and mechanical degradation. Insufficient water promotes the production of peroxides and other radicals that chemically degrade the cell by reacting with the ionomer in the membrane and CLs, accelerating their degradation [17–19]. Mason et al. [20] determined an MEA is capable of changing its thickness by 25% of its nominal size if compared between its wet and dry states. This large fluctuation in thickness, arising from hydration cycles, imposes mechanical stresses that contributes to the mechanical degradation of the membrane. As a result, the membrane conductivity can further decrease and it can become thinner and more brittle, increasing its susceptibility to pin hole and crack formation and further exasperating parasitic hydrogen crossover. Hydrogen crossover is the transfer of diatomic hydrogen through the membrane from the anode to the cathode. These hydrogen atoms carry electrons that would otherwise be carried through the external circuit, contributing to an overall loss in potential, thereby shifting the entire polarization curve down [1].

Although there is substantial evidence suggesting there is a positive correlation between water content and performance, the opposite is also true. Because the production of water is often insufficient to resist the convective drying imposed by the pure feed gases, it is commonplace to humidify the feed gases prior to entering the cell to prevent the membrane from drying. This additional source of water together with the large amount of water produced in the cathode at high current densities, increases the likelihood the gas stream will become saturated and water vapour will condense. Accumulation of this liquid water in the pores of the CL, MPL, GDL, and flow fields has been attributed to premature mass transport losses because it can block the pathways essential for gaseous mass transport [21–29]. Effective removal of liquid water is the first step to achieving higher current densities.

This has been demonstrated experimentally by He et al. [29] who correlated

the sudden drop in cell performance to a pressure drop across a fuel cell utilizing interdigitated flow fields. The channels of interdigitated flow fields are dead-ended, forcing the reactant gases to pass through the porous GDL before they are able to leave the cell. Liquid water accumulation in the pores throttled the gas flow through the remaining unblocked pores, causing a noticeable pressure drop across the inlet and outlet of the fuel cell.

Researchers have noticed treating the GDL with PTFE to create hydrophobic pores improves performance by preventing these pores from accumulating liquid water and leaving them exclusively available for gaseous transport [25, 26, 30]. This same idea has been extended to the development of MPLs. Wilson et al. [4] noted the addition of a hydrophobic microporous layer reduced the likelihood of flooding and offered improved performance over a similar macroporous layer.

Kim et al. [31] investigated the effect of MPL coated GDLs on water transport, concluding the hydrophobic properties of the MPL and the increased capillary pressure of the smaller pore size, encouraged water generated in the cathode CL to diffuse across the membrane and eject with the anode stream. This lead to reduced flooding in the cathode GDL, unobstructing oxygen transport, and improving performance at high current densities.

However, other groups have posited other theories on why the MPL improves performance. Owejan et al. [32] suggested the small pore size and hydrophobicity of the MPL forms a protective barrier preventing liquid water accumulated in the GDL from contacting and forming a liquid film on the CL interface. Without such blockage, they propose oxygen is free to transit through the MPL and react at the CL. This concept is further discussed in the following section.

Mughal et al. [28] approached liquid water accumulation from another perspective, comparing the effect of orientation, agitation, and pressure gradients on liquid water removal. A combination of all three led to the highest liquid water ejection rates and subsequently improved ohmic performance by 25% and mass transport performance by 30%.

Experimental evidence is also supported by numerical models. Zhou et al. [22–24] has developed and validated a multi-dimensional, non-isothermal, two-phase MEA model that predicts local saturation inside the MEA. Under wet conditions, the model predicts significant performance losses at high current densities when liquid water formation is favourable. The same models forecast these losses are reduced when an MPL is present in the cell.

Flooding is not exclusive to the porous media. Liu et al. [27] qualitatively monitored the accumulation of liquid water in different flow field designs using transparent

PEMFCs. Parallel channels were found to have the highest incidence of flooding and the poorest performance when compared to interdigitated and serpentine flow fields (when not taking into consideration systematic losses from the larger pressure drop they create). The other plate designs benefit from a higher pressure buildup if a channel is blocked and perpendicular flow between the channels shears accumulated liquid water from the pores, reducing the buildup of liquid water in the GDL [33].

In addition to mass transport limitations, liquid water is also considered a transport mechanism for impurities [34] and a contributing factor to platinum dissolution and migration [35, 36], leading to long-term performance degradation as the active area is reduced.

1.2.2 Water Balance Measurements

Although the need to maintain a proper balance of water inside the cell is apparent, accomplishing this is complicated by numerous internal transport mechanisms across the membrane. At any given moment, four different mechanisms may be at play: electro-osmotic drag (EOD) [13, 37–40], back diffusion [39, 41–43], hydraulic permeation [39, 43–45], and thermal osmosis [46–48]. Further, water leaves the cell in liquid and vapour form. Experimentally quantifying the individual mechanisms is difficult and so it is often experimental convention to report a single combined value called, among other names, the effective drag coefficient [40, 49–51] or water crossover flux [43–45, 52] (denoted as α [$\text{mol}_{H_2O}/\text{mol}_{H^+}$] in most literature). Typical convention defines the crossover flux as positive in the direction of the cathode, consistent the direction protons travel.

EOD is the accompanied drawing of water molecules through the membrane as protons transfer from the anode to the cathode. Temporary hydrogen bonds form between water molecules and protons, forming intermediate ion species such as hydronium, H_3O^+, that assist the transfer of protons through nano-sized water channels in the membrane [8, 53]. This water flux is quantified with a coefficient that corresponds to the number of water molecules dragged per proton transferred. Establishing an EOD coefficient for different cell architectures, pretreatments, and operating conditions is important to prevent the anode from drying at high current densities where the flux of protons towards the cathode is at its highest. Efforts to experimentally determine this coefficient motivated the development of early water transport setups.

Zawodzinski et al. [13] published one of the first EOD coefficients while detailing the transport properties of Nafion membranes with different water uptake levels (denoted as λ [$\text{mol}_{H_2O}/\text{mol}_{SO_3H}$]; a ratio of absorbed water molecules to sulfonic acid

groups in the ionomer). The number of water molecules transported across the membrane was determined from the change in height of a capillary on the anode side with the membrane exposed to liquid water on both sides to eliminate any concentration gradients. With a $\lambda = 22$, the EOD coefficient was measured to be 2.5 H_2O/H^+. The experiment was then repeated with saturated water vapour in place of liquid water, changing the water content to $\lambda \leq 14$ and dropping the EOD coefficient to 1.0 H_2O/H^+; agreeing with results published by Fuller et al. [38].

The fundamental setup for measuring EOD has largely remained the same. The membrane has to be exposed to the same water activity, pressure, and temperature on either side to eliminate the other transport mechanisms, isolating the water molecules dragged by only protons. The EOD coefficient can then be extrapolated from the current knowing the stoichiometry of the hydrogen decomposition reaction.

In a similar fashion, modifying the operating conditions allows other transport mechanisms to be isolated [39]. Inducing a water activity gradient by exposing the membrane to different humidities on each side and maintaining a uniform pressure, temperature profile and open circuit, allows back diffusion to be exclusively measured. With water produced by the ORR, the cathode typically has a higher water concentration than the anode, encouraging the diffusion of water towards the anode, compensating the EOD to some degree [11, 13]. The same principle can be extended for isolating pressure and thermal gradients. What remains is to find a method that can accurately measure the amount of water that crosses the membrane during operation.

Zawodzinski et al. [13] measured the EOD coefficient using a custom ex situ setup that translated the change in height of a water column in a capillary with a known diameter to the number of water molecules that crossed the membrane. While favourable for its simplicity and accuracy, the experimental setup required an unconventional fuel cell mockup comprised of wire electrodes and water reservoirs that resulted in a poor representation of a true fuel cell. Ex situ experiments remain important for experimentally deriving unique transport quantities that assist the development of fuel cell models [43, 54–56], however in situ investigations of water distributions inside a fuel cell and under realistic operating conditions are required to validate the models. This has lead to the development of several unique experimental approaches for elucidating water movement inside an operating fuel cell.

Most procedures reported in literature for measuring water crossover in operating cells have utilized water collection [13, 31, 49, 51, 54, 57–59]. This involves condensing and collecting the water from a fuel cell's effluent gas streams while maintaining strict control on the amount of water entering the cell. Water crossover across the PEM

can then be extrapolated from a mass balance applied to each side of the cell.

One of the earliest implementations of this technique was Zawodzinski et al. [13] whereby their previously calculated EOD coefficient was contrasted to the net water transport across the membrane during operation. The paper does not discuss their water collection setup in detail. A 50 cm^2 cell was operated at a steady state current of 0.5 A/cm^2 with flow rates of 0.3 and 0.15 lpm for the hydrogen and oxygen respectively. The net crossover was calculated from the water "collected" and weighed on each side of the cell. Their results concluded $\alpha = 0.2$ mol_{H_2O}/mol_{H^+} indicating back diffusion substantially offsets EOD.

Janssen et al. [49] used a cold trap as a condenser to measure the net crossover flux for a wide range of operating conditions and cell architectures. The net crossover flux was defined as,

$$\alpha = \frac{\dot{n}_{H_2O,A,i} - \dot{n}_{H_2O,A,o}}{I/F} \tag{1.8}$$

where $\dot{n}_{H_2O,A}$ is the molar flow rate of water entering and exiting the anode, and I is the cell current. Values were only reported from the anode for simplicity because it eliminates the water generated by the reaction from the numerator. The results were compared to the cathodic measurements with a noted difference ranging from 4% to 7%.

A large active area (50 cm^2), long experimental duration (6 hours), and low dry flow rates (stoich of 2) had to be used to generate an appreciable difference between the water crossing the membrane and the water introduced by the humidified reactant streams. The most notable conclusions showed the net crossover flux is a function of the humidity of the inlet gases, conditions that determine the humidity along the gas channel, and the thickness of the membrane.

Kim et al. [31] borrowed the cold trap design from Janssen et al. [49] but also included electrochemical impedance spectroscopy (EIS) to investigate the role of the MPL. Water collection was used to measure the net crossover flux and to determine how the MPL impacted water movement inside the cell whereas EIS was used to measure changes in cell resistance.

Kim et al. [31] investigated three different cell constructions. One where both the anode and cathode had MPLs, the second where only the cathode had an MPL, and the third where neither did. The water collection experiments were repeated five times for each cell construction, with the average reported with a relative error of +/- 1.5%. Not all the water can be condensed from a gas stream by lowering the temperature. The small portion of water that remained trapped in the gas after passing through the

cold trap was accounted for by assuming the gas left fully saturated at its dew point temperature. A sensitivity analysis indicated high gas flow rates strongly influence net water drag coefficient measurements. This prompted them to only report anodic measurements where lower flow rates are tolerated.

The group concluded the addition of an MPL(s) improved performance, predominately in the mass transport region, with the cell containing only an MPL on the cathode side performing the strongest. Furthermore, the water collection experiments concluded the addition of an MPL on just the cathode side increased water transport towards the anode. Both conclusions imply the performance improvements result from a decrease in liquid saturation in the cathode or equivalently, an increase in oxygen concentration at the cathode reaction site.

Colinart et al. [59] were another group who used a cold trap to monitor water crossover in a PEMFC stack in response to changes to different operating conditions. Again, for simplicity, only measurements performed at the anode were reported. They found the net crossover flux was dependent on current density, flow rates (primarily of the anode), and the humidification of the inlet gases.

Karan et al. [51] performed a similar experiment but chose an air-cooled knock-out drum and a water-chilled condenser downstream of a fuel cell to collect water. The knock-out drum, an artifact from their fuel cell test station, managed any liquid water ejected from the fuel cell while the condenser collected the vapour retained in the effluent streams.

Combining these two measures of water with the water retained in the gas downstream of the condenser (as per the same assumption), provided a picture for how the water moved inside the cell, given as the net crossover flux,

$$\alpha = \frac{F(\dot{n}_{H_2O,C,o} - \dot{n}_{H_2O,C,i}) - I/2}{I} \tag{1.9}$$

where $\dot{n}_{H_2O,C}$ is the flow of water leaving and entering the cathode side of the cell in mol/s, and I is the cell current in A. Their setup was verified by comparing the sum of the inlet water and generated water to the amount of water exiting the cell, proceeding when the values fell with a 95% confidence limit.

Contrary to Kim et al. [31], the group found no statistically significant correlation between the net drag coefficient and the presence of an MPL on the cathode side. Their choice of only reporting cathode values is not expressed in the paper but it may be because only the porous layers of the cathode were modified as part of the investigation. Atiyeh et al. [58] reached the same conclusions using the same setup.

Thomas et al. [47, 48] continued investigating the effect of an MPL on water

transfer but from a thermal perspective. They observed that the addition of an MPL raised the thermal resistance of the cell which in turn caused the electrode temperature to increase, generating a thermal gradient across the cell that influenced water movement and raised the saturation pressure of the gas. A thermoelectric condenser and a scale, accurate to 0.01 g, was used in the same capacity as the previously mentioned setups to monitor the net water flux inside the cell. It was concluded that an MPL did not affect the net water flux but did increase the electrode temperature, raising the saturation limit, and facilitating water removal in the vapour phase.

Adachi et al. [43, 54] used a water-cooled condenser to investigate the permeability of Nafion membranes with varying thickness after the membranes were exposed to concentration and pressure gradients. The results were then correlated with ex situ measurements of water transport properties for different activity gradients across the same membrane.

In situ testing was performed on a 25 cm^2 MEA with anode and cathode stoichiometry ratios of 2 and 3, and a minimum flow rate of 0.25 L/min. Prior to the first measurement, the cell was held at a constant current for 60 minutes with subsequent measurements taken after 20 minutes. The experiment was run until more than 3.0 g of water was collected at the anode. Only anodic values were reported for the same reason as Janssen et al. [49]. There is no mention of the accuracy of their setup.

It was observed that the largest magnitude of back diffusion occurred when liquid water was present on one side of the membrane and water vapour on the other; assuming the EOD from the ex situ and in situ experiments were equivalent. This suggests the accumulation of liquid water has a large influence on regulating the water balance of an operating fuel cell.

One other noteworthy technique for extracting water from a gas besides lowering the temperature is to make use of a desiccant. Ye et al. [60] used a commercial gas drying unit with a known mass of Drierite, a desiccant capable of lowering the dew point temperature of gas to $\approx -73°C$, and was able to monitor the water collected from the gas stream with a scale accurate to 0.01 g. In most cases, they were able to achieve a water balance between the anode and the cathode of greater than 98.5%. Reported results were then the average of anode and cathode values to further improve the accuracy of their setup.

The study looked into the EOD of GORE-Select membranes, an alternative to conventional Nafion membranes. Because of their increased thickness, back diffusion was considered negligible compared to EOD, so results were taken directly from a

water balance of an operating hydrogen pumping cell. A hydrogen pumping cell also benefits from the lack of water production minimizing the likelihood of a concentration gradient and back diffusion. The experimental methodology was validated after the same experiment was repeated with Nafion membranes and compared with Zawodzinski et al. [13].

In situ fuel cell results were then performed with thinner GORE-Select membranes and borrowing the EOD from before, it was found the water diffusion coefficient of GORE-Select membranes is roughly half that of Nafion with similar water contents. The same setup has also been used to investigate the effective water diffusivity of different GDL's [61].

Numerous reviews have been published on water management issues [8, 62–65]. Water collection remains the favoured means for studying water balance issues and experimentally quantifying the different transport coefficients owed to its simplicity and accuracy. However there are inherit setbacks to water collection that limit its universal applicability. Foremost are the long collection times needed to discern a measurable amount of crossover. A single PEMFC operating at 80°C, 90% RH, a stoich ratio of 2, and a steady current density of 2 A/cm^2 generates approximately 1.9×10^{-4} g/(s cm^2) of water with an additional 6.3×10^{-4} g/(s cm^2) of water leaving the cell because of the humidified inlet streams. Even with large MEA active areas, the long time required for collection fail to resolve transient behaviour.

This shortfall has spurred the development of transient water measurements. Sauriol et al. [52] completed a comprehensive evaluation of different real-time measuring techniques emphasizing resolution, accuracy, response time, cost, and engineering risk. Their conclusion led to the development of an experimental setup utilizing infrared adsorption sensors and syringe pumps.

The chosen LI-COR Bioscience LI-7000 infrared analyzer is capable of measuring the water content of the gas stream directly to within 1% of its reading and the syringe pump allows strict control over the volume of water entering the cell. Overall the group claimed the setup could measure the water transfer factor (also denoted as α defined as the net water flux across the membrane divided by the production of water) to within ±0.01.

Systematic errors were eliminated by bypassing the fuel cell and passing the gas mixture comprised from the main syringe pump and dry gas supply directly to the infrared analyzer. The syringe pump and dry mass flow controller are then "calibrated" with the downstream measurement equipment. During acquisition, the main gas mixture is redirected through the fuel cell and diluted downstream with a known flow rate of dry gas to evaporate any condensed liquid water, lower the mixture temperature,

and throttle the pressure to match ambient conditions, so as to accommodate the infrared analyzer's operating specifications.

Mixing chambers are then required for the syringe pump and infrared analyzer for proper operation. This creates its own concerns. In both cases, it is imperative all the water properly mixes and evaporates into the gas stream. There is also a physical capacitative nature to the downstream mixing chamber, potentially blending spontaneous events with the steady state ejection of water vapour, making it difficult to discern the extent of those transient events. The setup has been used extensively by Yau et al. [42, 44, 45] to investigate the relationship between net water crossover and a variety of imposed gradients.

One publication from Yau et al. [42] noted improved performance with the addition of an MPL which correlated with an increase in back diffusion towards the anode. This was attributed to an MPL-created resistance reducing water removal from the cathode flow fields.

Another group interested primarily in two-phase flow measurements decided in favour of a combined capacitive relative humidity and band-gap temperature sensor for water content measurements. Niroumand et al. [66] placed a Sensirion SHT75 sensor in a heated vessel with an absolute pressure transducer and took live measurements of the vessel's dew point to determine the flux of water in the gas stream as per,

$$\dot{n}_{vap} = \frac{\dot{n}_{gas}\, P_{vap}}{P_{gas}} \tag{1.10}$$

The vessel, placed downstream of a fuel cell, has a small volume intended to gravimetrically capture any liquid water entrained in the gas stream. The vessel is heated sufficiently above the anticipated dew point of the gas leaving the fuel cell to evaporate the liquid water that was either ejected from the fuel cell or condensed in the piping connecting the vessel with the cell. The humidity sensor is only sensitive to water vapour and will malfunction if comes into contact with liquid water. The liquid water content is therefore detected by the sensor as a momentary increase in the dew point of the vessel as the water evaporates. Although the authors proposed this method as a way for quantifying two-phase flow, it had unrealized potential for measuring water transport inside the cell.

Other noteworthy methods for measuring in situ water distributions were explored by Mench and Dong [67, 68]. Originally the group used an Agilent 3000 MicroGC Gas Chromatograph to measure the water vapour, oxygen, and nitrogen molar fraction at eight sample extraction points along a single serpentine flow channel [67]. The

chromatograph required 2 minutes of steady state operation before the species profile could be accurately reported. Their setup was later upgraded to an Agilent G3163A real-time gas analyzer [68], greatly reducing the sample time to the order of seconds. This setup was used to characterize the change in water activity along the channel length and did not explore the movement of water across the membrane.

Although not used to measure net water fluxes, neutron radiography and transparent PEMFCs have been used to quantify liquid water distributions inside the cell. Neutron radiography has been used extensively for visualizing liquid water inside a regular fuel cell [69–73]. Neutron attenuation is not influenced by material density giving it the ability to pass almost unimpeded through metallic surfaces, such as the structural components of fuel cells, whereas hydrogen, in particular that bonded in water, has a large scattering effect. This allows the in situ real-time imaging of water movement inside a fuel cell without compromising the cell's architecture. The large difference in density between liquid water and water vapour makes it difficult to discern the distribution of water vapour, so neutron radiography is used almost exclusively for imaging liquid water. Furthermore, the complexity and availability of neutron radiography facilities make this technique exceedingly expensive for regular experiments.

Transparent PEMFCs are a partial alternative to neutron imaging [30, 74]. While simple in principle, a custom transparent fuel cell has to be machined and even then, the electrical conductivity of the transparent materials requires the introduction of conductive interfaces which would otherwise not be present in a regular cell. The transparent window provides a qualitative view of water desorption from the GDL and water accumulation in the flow field channels. This can then be correlated with operating conditions but is more commonly used to provide a perspective on the evolution of liquid water along the channel path.

1.2.3 MPL Investigations

It is widely recognized that the presence of an MPL between the CL and GDL improves cell performance at high current densities and under wet conditions [4, 6, 7, 22–24, 31, 32, 51, 54, 58, 75–78]. The reason for the improved performance however remains unresolved. Different groups have reached contradictory conclusions with some evidence suggesting the MPL encourages back diffusion and water removal from the anode [31, 42, 54], while other evidence indicates higher water removal rates from the cathode CL to its respective channel [48, 79]. It has also been proposed the MPL acts as a barrier preventing liquid water accumulated in the GDL from flooding the

CL [32].

The performance improvement is almost exclusively exhibited in the mass transport region [31]. One might expect the addition of a physical barrier would inhibit mass transport but evidence suggests the MPL positively influences water management at moderate to high current densities, providing an overall net benefit [32, 75]. Recent studies have also shown MPLs reduce the variability of the polarization curve at high current densities [51, 58, 75], providing a measure of stability for when conditions are favourable for flooding.

Malevich et al. [75] used electrochemical impedance spectroscopy (EIS) to investigate the change in ohmic, charge transfer, and mass transport resistances of an operating PEMFC. The group observed no statistically significant differences in ohmic or charge transfer resistance between cells with and without an MPL, however those with an MPL demonstrated a lower mass transport resistance, which further analysis correlated with gas transport inside the porous transport layers. This was further supported by Ramasamy et al. [76], where it was demonstrated the addition of an MPL and hydrophobic treatments to the GDL reduced the mass transfer resistance. In both instances, the researchers proposed the MPL reduced the likelihood of flooding but in using EIS, were unable to confirm how the water was moving.

Studies into the movement of water inside fuel cells with and without MPLs have failed to reach a consensus. Kim et al. [31], using a cold trap for water collection, concluded placing an MPL on the cathode encourages water to move from the cathode to the anode. Numerical models support Kim's conclusion predicting an assymetric cell with an MPL on the cathode side will develop a pressure gradient effectively driving water towards the anode [6, 79]. However Atiyeh et al. [58] was unable to observe a statistically significant enough change to the net crossover flux with a similar cell construction; a conclusion reaffirmed by other publications [51, 80].

However, it should be noted the former studies were performed on Gore membranes with a thickness less than 25 μm whereas the latter studies used Nafion N112 membranes with a thickness of 51 μm. Adachi et al. [43] noted the water permeation across Nafion membranes is inversely proportional to the membrane thickness. Although the change in concentration driven water permeation was more pronounced for changes in membrane thickness above 56 μm, water flux across thinner membranes was highly susceptible to a pressure gradient. Given that the small pore size and hydrophobicity of the MPL appears to increase the breakthrough pressure of the GDL, introducing an MPL on only one side of a cell might generate a hydraulic gradient across the membrane. Therefore the thickness of the membrane may play an integral role in complementing the MPL.

Furthermore, the catalyst loading of the commercial MEAs used in each of the prior studies was greater than 0.3 mg_{Pt}/cm^2. Low-loaded inkjet printed electrodes from the University of Alberta have a scalable loading and are not restricted by the type or thickness of membrane [81–83]. This provides flexibility for the types of MEA architectures that can undergo water balance investigations. The MEA architectures used for published in situ MPL studies are summarized in Table 1.1.

Table 1.1 – Literature MEA architectures for MPL investigations

Reference	MEA	Thickness	Catalyst Loading
Kim et al. [31]	Gore-PRIMEA-18	18 μm	0.4 mg_{Pt}/cm^2
Owejan et al. [32]	Gore-Select-5510	25 μm	0.4 mg_{Pt}/cm^2
Karan et al. [51]	IonPower N112	50 μm	0.3 mg_{Pt}/cm^2
Atiyeh et al. [58]	Fuel Cell Store N112	50 μm	0.3 mg_{Pt}/cm^2
Malevich et al. [75]	IonPower N112	50 μm	0.3 mg_{Pt}/cm^2
Ramasamy et al. [76]	Gore-PRIMEA-57	(R) 18 μm	0.4 mg_{Pt}/cm^2
Pharoah et al. [80]	IonPower N112	50 μm	0.3 mg_{Pt}/cm^2

R - Reinforced

1.3 Objectives

The aim of this research is to develop an experimental procedure and setup for actively monitoring the water distribution throughout an operating PEMFC. This will provide a means for understanding the mechanisms behind changes in performance for differing cell architectures and operating conditions. More specifically, the major contributions of this work are towards furthering our understanding of water management in PEMFCs; a critical avenue towards realizing the full potential of PEMFC technology. In particular, the following areas will be addressed:

1. Design and construct an affordable, user-friendly experimental setup for accurately monitoring transient water fluxes inside operating PEMFCs

2. Validate the experimental setup with physical expectations and established literature results

3. Investigate the effect MPLs have on the net crossover flux for PEMFCs with varying membrane thicknesses

Furthermore, this work will become the foundation for future endeavours in this research field and assist with the development of multi-phase flow numerical fuel cell models [22–24]. The combined experimental and numerical results will facilitate the

development of novel inkjet printed GDE and CCM constructions pioneered by the University of Alberta.

1.4 Thesis Outline

This thesis has been organized into six chapters. Chapter 1 provides a technical overview of PEMFCs before discussing, within an extensive literature review, the importance of water management and recent experimental efforts to understand it. A brief literature review follows providing insight into the effects of MPLs on overall cell performance. Chapter 2 begins with an outline of the experimental theory and continues by guiding the reader through the design process for the water balance setup. The chapter concludes with instructions on operating the setup and how to fabricate and characterize MEAs. Chapter 3 contains a thorough analysis of the setup's accuracy based on sensor specifications and auxiliary experiments. Chapter 4 details the setup's successful comparison to established physical laws and published literature results to experimentally validate the setup. With the full potential of the setup realized, Chapter 5 investigates the effect of MPLs on MEAs with varying membrane thicknesses. The thesis then concludes with Chapter 6 summarizing the main contributions and a discussion regarding potential future work.

Chapter 2

Experimental Setup

This chapter describes the development, construction, and operation of a transient water balance experimental setup for monitoring the internal water fluxes of an operational PEMFC. Section 2.1 outlines the theory and calculations providing the framework for the setup's measurements. Section 2.2 discusses the target design parameters as well as addressing hardware features that were considered and in some cases ultimately abandoned, providing justifications for both. Section 2.3 details the selection of different sensors with emphasis on their advantages. And in conclusion, Section 2.4 outlines the operating procedure, fabrication and assembly of fuel cells, and baseline characterization for acquiring consistent and repeatable results.

2.1 Experimental Approach

To determine the overall water distribution and net water flux inside an operating PEMFC, the anode and cathode are treated as two coupled control volumes, shown in Figure 2.1.

The net crossover flux of water across the membrane, $\dot{n}_{crossover}$, is found by the difference in the molar flow rates of water entering and leaving the anode. A net crossover flux towards the cathode is considered positive convention to coincide with the direction of protons across the membrane. Because the control volumes are coupled, the crossover flux can also be found by considering the same difference applied to the cathode provided the inclusion of the water generated as a product of the ORR, $\dot{n}_{H_2O,rxn}$, (equation (1.4)),

$$\dot{n}_{crossover} = \dot{n}_{H_2O,A,i} - \dot{n}_{H_2O,A,o} \tag{2.1}$$

$$\dot{n}_{crossover} = \dot{n}_{H_2O,C,o} - \dot{n}_{H_2O,C,i} - \dot{n}_{H_2O,rxn} \tag{2.2}$$

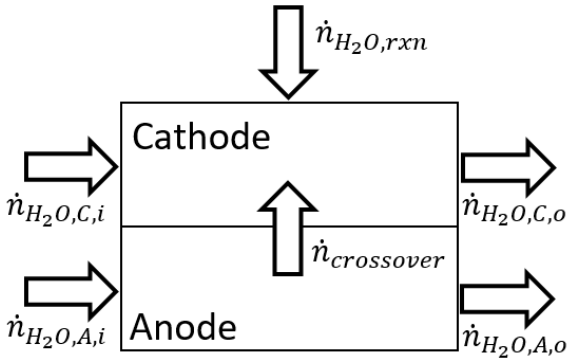

Figure 2.1 – Coupled control volumes of a PEMFC. Positive crossover denoted as towards the cathode

where $\dot{n}_{H_2O}$ denotes a molar flux of water and subscripts A, C, i, and o represent anode, cathode, in, and out respectively.

These are simplified versions of the continuity equation. Although it is acknowledged some measure of water will be absorbed by the membrane and remain trapped in the GDLs, the accumulation of mass inside the system is considered negligible because the combined volume of the membrane and porous layers displaced with water amounts to about 0.25 g; equivalent to the amount of water that enters the cell over approximately six and a half minutes when the cell is heated to 60°C and fed hydrogen and air at 0.2 slpm and a humidity of 50%. The duration of most experiments is on an hourly basis and only initiated after the cell has undergone a conditioning procedure conducted to hydrate the membrane and GDLs.

The molar flow rates of water entering the cell can be calculated from the parameters inputted into the Scribner 850e fuel cell test station. The test station contains built in mass flow controllers, bubble humidifiers, and process controllers for modifying the cell and gas properties. Assuming the gas leaving the bubble humidifier is fully saturated and there are no entrained liquid droplets, the molar flow rate of water entering the cell can be found from,

$$P_{vap} = P_{sat} = 0.61121 \exp\left(\left(18.678 - \frac{T_{gas}}{234.5}\right)\left(\frac{T_{gas}}{257.14 + T_{gas}}\right)\right) \tag{2.3}$$

$$\dot{n}_{H_2O,i} = \dot{n}_{gas,i} \frac{P_{vap}}{P_\infty - P_{vap}} \tag{2.4}$$

where T_{gas} is the temperature of the gas leaving the humidifier in °C, $\dot{n}_{gas,i}$ is the dry molar flow rate of gas entering the cell in mol/s, and P_∞ is the absolute pressure

at the water level inside the humidifier in kPa. Equation (2.3) is the Buck experimental correlation for the saturation pressure of moist air over liquid water published originally in 1981 [84] and later revised in 1996 [85].

The temperature of the gas and dry gas flow rate are prescribed by the test station software. The dry flow rate is inputted in standard litres per minute (slpm), corrected to a temperature and pressure of 0°C and 760 mmHg respectively. Conversion between slpm and the molar flow rate is found using the Ideal Gas Law,

$$\dot{n}_{gas,i} = \frac{(101.325 \text{ kPa})(\dot{V}[\text{slpm}])}{R(273.15 \text{ K})(60 \text{ sec})} \tag{2.5}$$

Because there is no practical way to measure the pressure at the liquid-gas interface inside the humidifier, this approach does not provide very accurate values for the inlet water content. Bypass lines, similar to those used by Sauriol's group's design [52], circumvent the fuel cell and allow the inlet gas properties to be measured directly by the water balance setup. Provided the system has reached steady state, this shifts the local pressure measurement away from the humidifier to the water balance setup with the added benefit of eliminating systematic measurements errors when measuring the net crossover flux (see Section 3.1 for more discussion). With the bypass approach, T_{gas}, RH, and P_{∞} are all measurands of the water balance setup and not assumed test station inputs, thereby providing a more accurate assessment of the gas properties entering the cell. As is later demonstrated, the test station often does not meet its set point values.

Calculating the water content of the gas entering and exiting the fuel cell is then identical. Following the principles in equations (2.3) and (2.4), the same temperature, relative humidity, and pressure measurements are recorded, however the vapour pressure is derived from the relative humidity. Furthermore, when determining the water content of the effluent gas downstream of the fuel cell, the dry molar flow rate leaving the cell, $\dot{n}_{gas,o}$, has to also be corrected to account for reactant consumption due to the ORR and HOR (equation (1.4)):

$$P_{vap} = RH \cdot P_{sat} \tag{2.6}$$

$$\dot{n}_{gas,o} = \dot{n}_{gas,i} - \dot{n}_{rxn} \tag{2.7}$$

This methodology only applies provided all the water leaving the cell remains in the vapour phase and there is negligible gas crossover between the anode and cathode.

For hydrogen, the most permeable gas, the crossover rates are on the order of 10^{-7} mol/(cm^{2}s), measured in-house with cyclic voltammetry, whereas the lowest

inlet flow rates are on the order of 10^{-5} mol/(cm^{2}s), reaffirming that the membrane is objectively impermeable to gas crossover.

2.2 Hardware Design and Construction

In addition to being capable of accurately measuring the aforementioned measurands, the setup's final design had to overcome several other technical and physical constraints. An illustration of the final product can be seen in Figure 2.3. At its most fundamental level, exhaust gases from a fuel cell travel inside gas tight piping immersed in an externally controlled heated water bath and proceed past relative humidity, temperature, and pressure sensors before being vented through a back-pressure regulator and a forced-air cooled condenser to a fume hood. The anode and cathode have separate but identical pathways and measurement equipment.

The water balance setup has to be able to manage the gases vented from an operational PEMFC. This defines the temperatures, pressures, moisture levels, and gas mixtures that can be expected. The normal operating conditions for PEMFC characterization are summarized in Table 2.1.

The most hazardous conditions occur when the fuel cell is hot and wet, defined as 80°C and 90% RH. Here the gases leaving the cell, which are near or at complete saturation, have the largest thermal gradient relative to the ambient atmosphere resulting in large thermal losses through the auxiliary piping. At these conditions, a small decrease in the gas temperature forces water vapour to condense, contradicting the required assumption that all water passing the sensors is vapour. Should that be the case, the humidity sensor will falsely under-report the moisture profile of the gas. The presence of liquid water is also a concern for the electrical sensors,

Table 2.1 – Typical PEMFC operating conditions

Operating Conditions	**Value**
Cell Temperature	60-80 °C
Anode RH (Temp.)	50-90% (46-77 °C)
Cathode RH (Temp.)	50-90% (46-77 °C)
Anode Flow Rate	0.10-0.40 slpm
Cathode Flow Rate	0.20-1.75 slpm
Pressure[1]	0-100 kPa(g)
Anode Gases	Hydrogen, Nitrogen, Water
Cathode Gases	Air, Nitrogen, Oxygen, Water

1: Approx. barometric pressure of Edmonton: 91-96 kPa

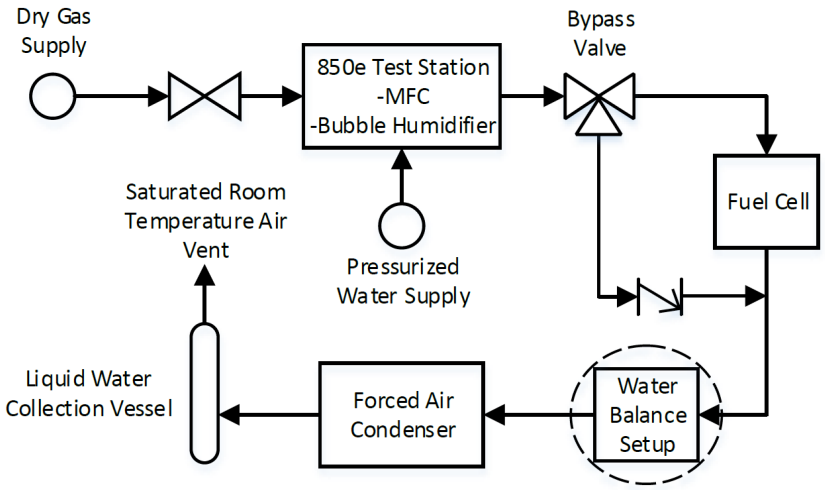

(a)

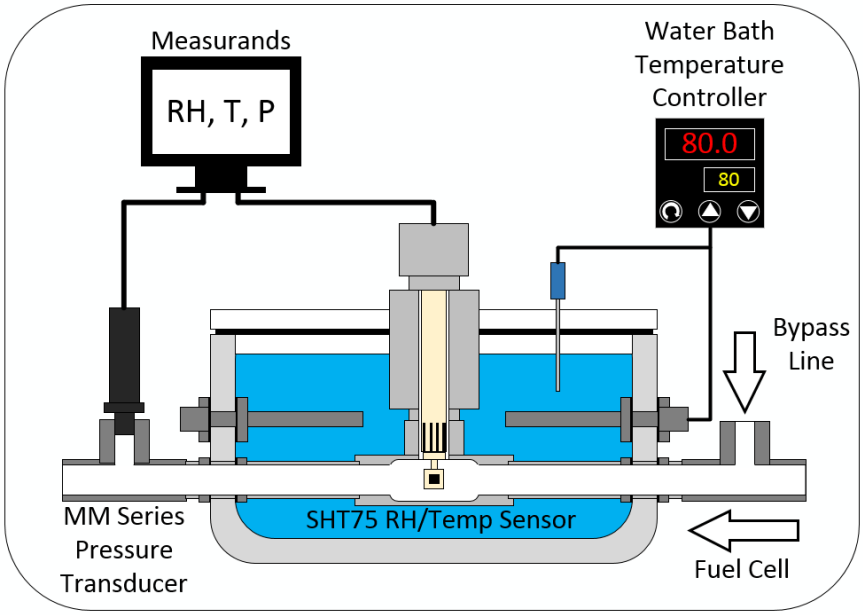

(b)

Figure 2.3 – Process flow diagram (a) and illustration of the water balance setup (b)

possibly causing them to short if they are to come into contact with liquid water. To prevent condensation and to evaporate any liquid water ejected from the cell, the gas surrounding the sensors has to be heated above the dew point of the gas leaving the cell. Given the warmest the cell is expected to operate is 80°C, the measurement apparatus has to be capable of warming the sensors to a *minimum* of 80°C.

The test station and fuel cell hardware utilize 316 stainless steel (SS) Swagelok branded 1/4" couplings, renowned for their corrosion resistance and gas tight connections. Owing to the same justifications, especially in the presence of hydrogen where leaks are a critical safety hazard, and to maintain compatibility with the existing equipment, Swagelok fittings were used in the setup, where possible, for all gas tight and pressurized lines. Wherever a Swagelok branded coupling could not be used, NPT fittings with Teflon thread tape were used instead. The setup was then tested with a surfactant leak solution and monitored with a Dräger Pac III hydrogen gas detector to ensure there were no leaks.

The complicated geometry of the large diameter sensor housings and the necessity for uniform heat distribution justified the design of a heated water bath heated with three 250 W SS immersion heaters and controlled with an OMEGA CN7800 series process controller and a T-type probe thermocouple. Because of the large thermal mass of the sensor housing, a thermal gradient is established across the fittings' walls when gas is flowing. As a result, the gas travelling through the housing tends to be a few degrees cooler than the surrounding water. There is no exact measure dictating how warm the water needs to be, however from experience, a 5-10°C increase above the cell temperature is sufficient to ensure the sensors are heated above the anticipated dew point regardless of the flow rates.

This increases the required water temperature up to 90°C. The basin was constructed out of clear polycarbonate, rated to a temperature of 100°C. A higher temperature rating would have been preferable but selection was limited because very few easily machinable thermoplastic containers are thermally stable at high temperatures. That being said, all other chosen construction materials were rated for higher temperatures. The lid and submersed supporting bracket, constructed from UHMW PE, are rated up to 135°C and all the gasket material is silicone rubber, rated to temperatures above 230°C. The design includes a lid which acts as both a safety measure, preventing accidental exposure to near boiling water, and as an insulator, greatly reducing heat loss from evaporation. A silicone sheet placed between the water basin and table further reduced heat loss due to conduction. All ports through the basin walls were sealed with similar silicone gaskets and SS bulkhead fittings.

The three immersion heaters were installed symmetrically at the lowest practical

point through the basin wall with the intention of using natural convection to its fullest potential to facilitate heat distribution. The supporting bracket has a reduced profile for the same reason. Evenly distributing the heat sources removed the need for agitation or circulation to achieve a uniform temperature.

Critical dimensions were determined from the pre-existing equipment, pictured in Figure 2.5. The water balance setup's nominal pipe and external coupling size matched those used by the test station and the position of the setup's inlet and outlet were dictated by the spacing and height of a fuel cell's respective connections. The overall size of the setup was mildly flexible however it did have to share the work bench surface already partially occupied with the test station and fuel cell.

(a) Scribner 850e Fuel Cell Test Station **(b)** Fuel cell hardware

Figure 2.5 – Standard fuel cell testing equipment

Figure 2.7 shows the water balance setup complete with a fuel cell during operation. Between the fuel cell and setup are a pair of tees converging the gas flow from one side of the fuel cell and its respective bypass loop. The fuel cell flows uninhibited into the tee whereas the bypass loop travels through a check valve first. This prevents the recirculation and condensation of gas inside the bypass loop when measurements are being performed on the fuel cell. The same concern is not as imperative when taking measurements from gas intentionally directed through the bypass loop. Upstream of the fuel cell is a three way valve responsible for directing flow from the

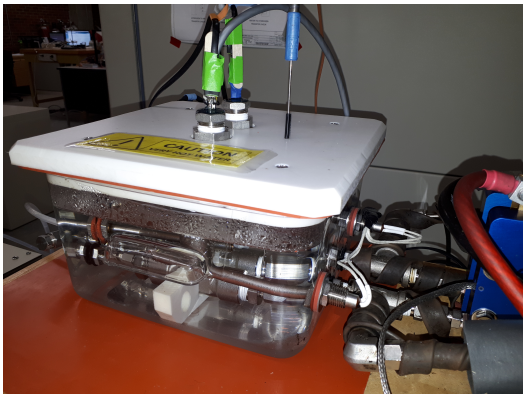

(a) Heated water bath and sensor housing

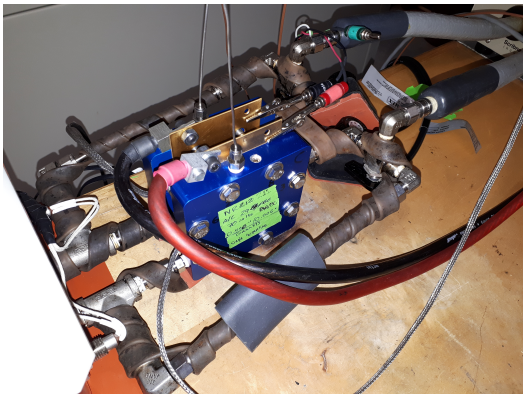

(b) Fuel cell and heated bypass lines

Figure 2.7 – Complete water balance setup during operation

test station into either the fuel cell or the bypass loop. The additional fittings and piping needed for the bypass loop were wrapped with an OMEGA HTWAT051-004 heat tape. During operation, the heat tape is arbitrarily heated above the cell temperature to minimize heat loss and reduce the likelihood of condensation. All fittings were also oriented is such a way that the downstream ports were physically below their inlets to prevent any unintended water accumulation.

2.3 Sensor Selection and Specifications

Relative humidity is meaningless without indicating the temperature so often the two sensors are coupled. The affordability, size, simplicity, robustness, and accuracy of the Sensirion SHT75 RH\T sensors used by Niroumand et al. [66] prompted the same sensors to be used in this work. They are a combination of a silicon bandgap temperature sensor and a relative humidity capacitive element mounted together on a manufacturer developed PCB. They are exceedingly affordable (<$100), less than 6 mm^3 in volume, recoverable after exposure to liquid water, and have a typical accuracy of $\pm$ 2.0% RH over their operating temperature range (with an accuracy of $< \pm$ 0.3 - 1.2°C). Temperature and relative humidity data acquisition was performed with Sensirion's own software and communication box as part of their EK-H4 plug and play developer kit.

Early designs had the sensors suspended and oriented by their wires. Inconsistent temperature measurements before and after removing the sensor from the housing suggested the alignment of the sensor relative to the housing walls adversely affected the measurements. This was partially remedied by reinforcing the position of the sensor relative to housing walls with concentric layers of rigid shrink tubing and

insulating the sensor from contact with the wall. However the need to maintain a repeatable position was apparent. The solution was to mount the PCB onto the end of a hollow dowel with an outer diameter that matched the inner diameter of the sensor housing, thereby maintaining concentricity and flow immersion between experiments, and reducing the dead volume above the sensor. The center of the dowel contains a patterned breadboard (VectorBord® 8019) and is filled with LORD® 305-1/2 epoxy to hermetically seal the chamber. The dowel is mounted inside a NPT coupling with the same epoxy. With the dowels machined to the same length, the NPT thread standard ensures the height of the PCB is adjustable. A schematic and a picture of the feed through assembly can be seen in Figure 2.9.

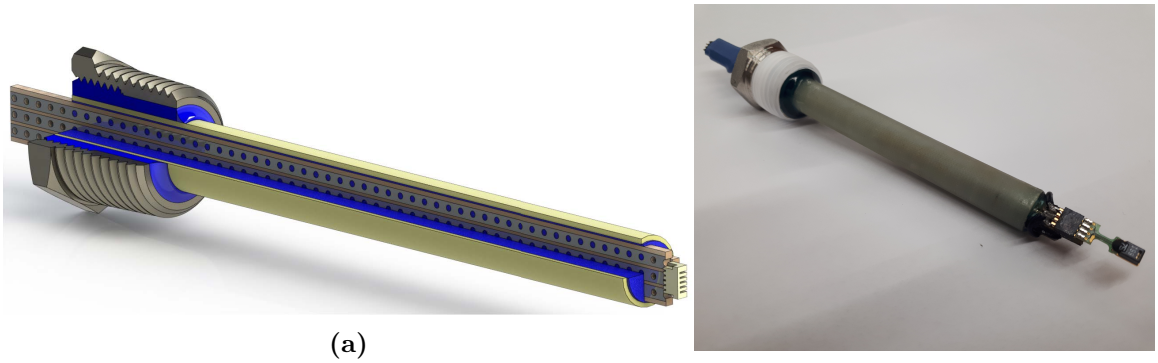

(a) **(b)**

Figure 2.9 – CAD section view (a) and finished picture (b) of the sensor feed through assembly

Most characterization experiments performed on PEMFCs in the ESDLab are operated at a pseudo-atmospheric pressure. There is approximately 16 feet of smooth bore 1/4" tubing downstream of the fuel cell which contributes some amount of pressure drop resulting in a slightly above atmospheric pressure inside the cell. There are also additional pressure losses from the bipolar plate flow field. These losses are negligible when back pressure is applied on the order of kilopascals, but cannot be disregarded during low pressure experiments, especially considering the ratio of water content to dry gas is more sensitive at lower pressures (Figure 2.11). To improve the accuracy of the setup, a pressure transducer was included with the RH\T sensors. The theory outlined in the previous section is only valid if all three measurands are recorded near simultaneously at the same location. Attempts to place a pressure sensor inside the water bath were hindered by the extreme conditions inside the sensor housing and space constraints. CFD performed with SOLIDWORKS Flow Simulation was used to determine whether the pressure sensor could be shifted away from the SHT75 sensor and outside the water bath without adversely affecting the

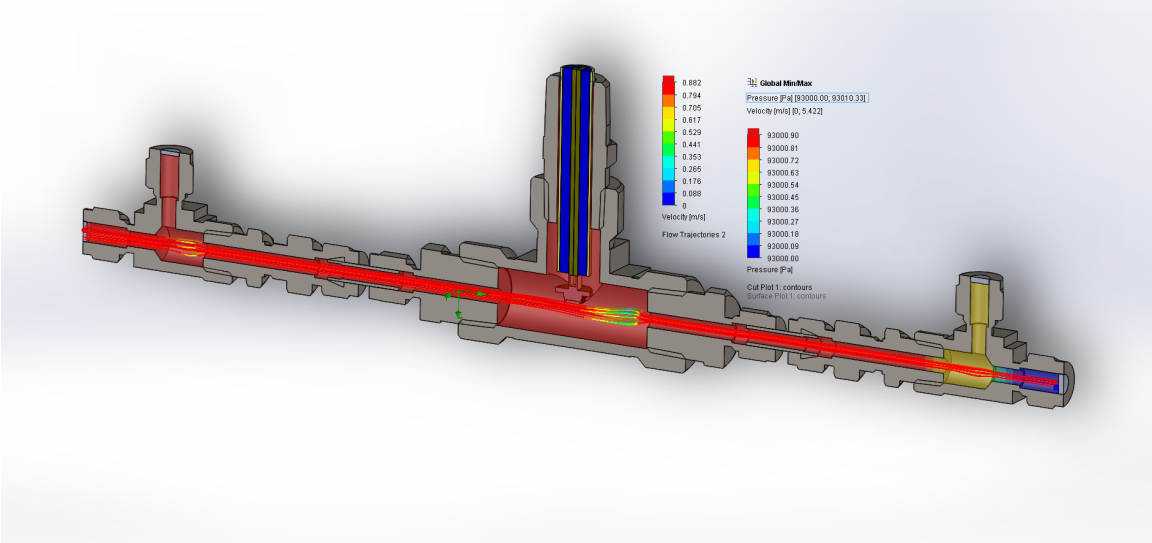

Figure 2.10 – Flow simulation of sensor housing estimating pressure drop between sensor locations

measurements.

The flow study, shown in Figure 2.10, was an estimation of the anticipated conditions inside the sensor. The inlet conditions prescribed hydrogen gas at 80°C enters the left port at a flow rate of 0.4 slpm. The hydrogen flows around the SHT75 sensor and exits through the right port held at an atmospheric pressure of 93 kPa. The walls were considered adiabatic and given a surface roughness of 0.5 μm based on values reported by Swagelok for their stainless steel fittings. Under these conditions the difference in pressure between the SHT75 sensors, located in the main tee, and the pressure transducer, to be located 5 cm downstream on the right vertical port, was negligible, i.e. on the order of ten pascals, justifying the separation between the two different measurements. Placing the pressure sensor outside the water bath softened the temperature, water proofing, and spatial requirements for the pressure transducer.

The criteria for choosing the pressure transducer included the ability to operate in a hot and humid environment, accurate to within 50 Pa, and measure upwards of 200 kPa absolute. This led to the selection of two custom OMEGA MM Series pressure transducers (Part no. MMA015V10K2C0T4A6CE, MMA030V10K2C0T4A6CE) with a range of 100 kPa(a) and 200 kPa(a), temperature compensated to 105°C, and an accuracy of +/- 0.05%. Calibration documents for the pressure transducers are contained in Appendix D. All wetted parts are 316SS meaning it is fully resistant to liquid water. Two transducers were purchased because the capacity to measure higher

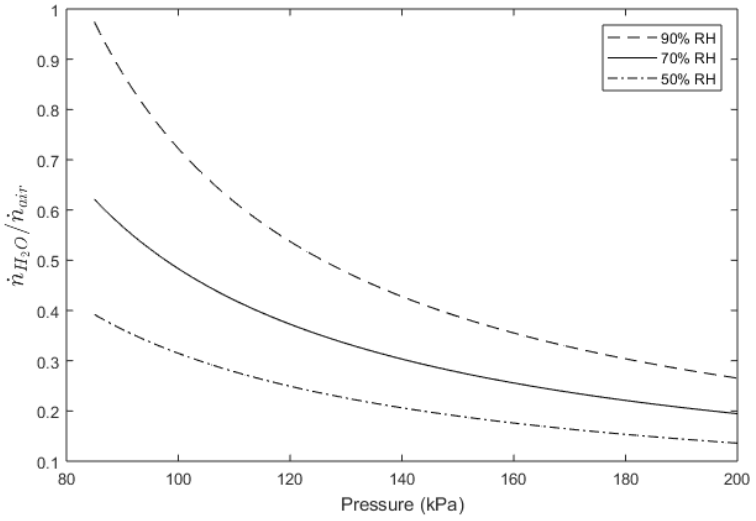

Figure 2.11 – Sensitivity of water content to changes in local pressure

pressures sacrifices resolution. Currently, the 0-10 V analog transducers communicate with an Arduino Genuino developer board after passing the signal through a voltage divider. Future plans would be to transition away from the the Arduino and use a 0-10 V DAQ instead.

Ideally, the sensors would share the same printed circuit board (PCB). This has many benefits not limited to increased accuracy, reduced cost, and simplified data processing. The idea was prototyped with the improved Sensirion SHT35 RH/T sensor and a TE Connectivity MS5803-01BA miniature variometer module. Much work was invested into redeveloping the setup with the improved sensors however reliability and time constraints prevented it from being implemented. Appendix A further explores this issue.

2.4 Setup Operation

2.4.1 Startup/Shutdown Procedures

A startup and shutdown procedure was developed to safeguard the sensors from any residual water that may build up as the water bath is cooled between experiments. During operation, humid gases are cycled through the sensor housing and upon completion, may not have an opportunity to evacuate the sensor housing before the water bath returns to room temperature. Any water vapour retained in the housing will then condense on the housing walls or the sensors themselves, putting the sensors at

risk of an electrical short if they are powered.

Therefore, the foremost part of the startup procedure is to ensure the water bath is heated and flushed with pure nitrogen prior to powering the sensors. Any liquid water retained by the sensor housing between experiments will evaporate and be replaced with dry nitrogen. Depending on the intended temperature of the water bath, this may take between 15-30 minutes. If there is a fuel cell upstream of the setup, it is important to direct the purge gas through the bypass lines to avoid needlessly drying the fuel cell.

After the temperature of the water bath has stabilized approximately 5-10°C above the anticipated cell temperature, the sensors can be turned on and begin communicating with the computer. The humidifiers can now be activated as they require approximately an additional hour for them to warm and their temperatures to stabilize. Once the temperature, relative humidity, and pressure readings through the bypass lines are steady, those values are recorded and later used to determine the water content entering the cell. It is assumed that provided the test station set points are not changed, these values will remain fixed for the duration of the experiment. Gas flow can then be directed through the fuel cell, requiring an additional hour of steady state operation to ensure the MEA reaches equilibrium for the prescribed operating conditions. The same process as before applies and the experiment and data acquisition can begin when the temperature, relative humidity, and pressure leaving the fuel cell begin to stabilize.

The sampling rate of the sensors was set to match the approximate residence time of the gas inside the sensor housing. Calculations in Appendix B show a sampling rate of one or two seconds is appropriate depending on the operating conditions to capture any transient events that pass through the sensor housing.

Upon completion of an experiment, gas flow should be redirected through the bypass lines. Same as before, the temperature, relative humidity, and pressure should be recorded and compared to the same values recorded before the experiment. If these values are outside the expected uncertainty (Section 3.4), the experimental results are inconclusive and should be repeated. Some minor drift within the accuracy of the setup is expected. Examples of acceptable before and after dew points noted by the sensors from actual experiments three hours in duration are summarized in Table 2.2.

The sensors can then be powered down. To facilitate the next startup, it is beneficial to purge the system for 15-20 minutes with dry nitrogen to flush any remaining water from the system before allowing the water bath to cool. The bath and test station can then both be powered down.

Table 2.2 – Acceptable test station dew point variations measured before and after experimentation

	#1	#2	#3
Before	48.82 °C	48.70 °C	49.03 °C
After	48.94 °C	48.99 °C	48.99 °C

2.4.2 MEA Fabrication

Fabrication of different MEA architectures at the Energy Systems Design Laboratory at the University of Alberta is made possible because of proprietary ink formulations and a commercially available Fujifilm Dimatix 2831 inkjet printer, shown in Figure 2.12. The printer uses 16 independently programmable piezo-electric nozzles for depositing individual ink droplets on a substrate of your choosing. This method is favourable over other conventional low catalyst loading fabrication methods, such as spray coating, because of its high precision, repeatability, negligible waste, and the ability to print patterned electrodes.

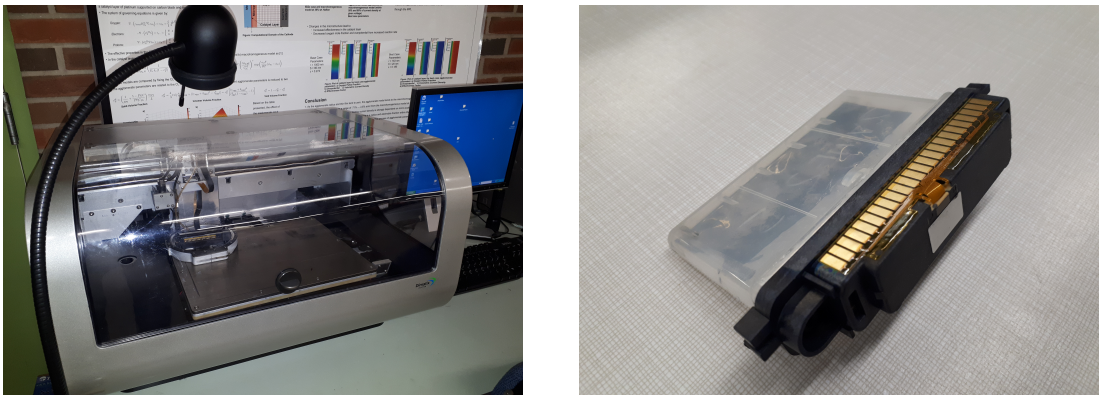

(a) **(b)**

Figure 2.12 – The ESDLab's Fujifilm Dimatix 2831 inkjet printer (a) and the ink cartridge and 16 nozzle printing head (b)

The ink is a slurry of nano particles of platinum supported on carbon black suspended in a solution of alcohols, glycols, and ionomer suspensions. In addition to being a proton conductor, the ionomer acts a dispersion agent preventing particle agglomeration and settling. After deposition, the volatile components are evaporated away leaving a porous catalyst layer.

Commonly, multiple CCMs are printed simultaneously onto a cast Nafion membrane in combination with a single aluminium foil square to determine loading. Catalyst loading, w_{Pt}, is estimated gravimetrically by inferring the change in mass, Δm, of an aluminium sample coated with a catalyst layer using the following formula,

$$w_{Pt}\ [\mathrm{mg_{Pt}/cm^2}] = \frac{\Delta m\,(1 - w_N)\,c_{Pt}}{A} \tag{2.8}$$

where w_N is the final ionomer loading expressed as a percentage of the final weight (i.e. 10-30%), c_{Pt} is the platinum content of the catalyst expressed as a mass fraction of the total weight, and A is the area of the printed sample. Different catalyst and ionomer loadings can be achieved by modifying the ink recipe or increasing the number of printed layers. Furthermore, any substrate may be used provided it fits within the printer's spatial constraints. This allows CCM fabrication with membranes of varying thickness and composition. For more information, refer to the work of S. Shukla [81–83].

At least one CCM was also prepared using a doctor blade and hot press. This method is favourable for large area CCMs that require high loading. From ink formulation to the final CCM takes substantially less time with doctor-blading than with the inkjet printer however there is significant waste, poorer repeatability, and less control of the final properties.

A more viscous ink is drawn across a PTFE substrate with the doctor blade to form a thin film and left to dry beneath a heat lamp. Samples matching the desired surface area are then cut from the bulk substrate. The individual samples are weighed with their PTFE backing prior to being assembled into a sandwich with a Nafion membrane. The sandwich, with the catalyst layers in contact with the membrane, is then placed into a hot press. After exposure to a predetermined temperature and pressure, the PTFE backings are removed, leaving the catalyst layers adhered to the Nafion membrane. The loading is determined from the final weight of the backings.

The ink compositions used for the preparation of different CCMs as part of this work are summarized in Table 2.3.

Table 2.3 – ESDLab CCM ink compositions

Constituent	**Type**
Inkjet Platinum Catalyst	HyPlat 40% Pt supported on Ketjenblack
Doctor Blade Platinum Catalyst	TKK 46.7% Pt supported on carbon black
Ionomer Solution	Liquion LQ-1105 1100EW 5% wt Nafion
Ionomer Loading	30% wt
Solvents	Isopropyl alcohol-2 & Propylene glycol

2.4.3 Fuel Cell Assembly

After printing, the CCM is laminated using conventional 3 mil lamination sheets with a window removed where the lamination sheet would overlap the catalyst layers, shown in Figure 2.13a. This is primarily to assist with handling of the CCM. Gaskets with the same window removed flank the MEA on both sides. Two GDLs specific to the experiment are cut to the same size as the catalyst layer and placed inside the window of the gaskets and in contact with the catalyst layer. The entire assembly is then placed between two bipolar plates guided with pilot holes to assist with the alignment and sandwiched inside a set of current collectors and end plates. The end plates are held in place by eight bolts arranged in a circular pattern.

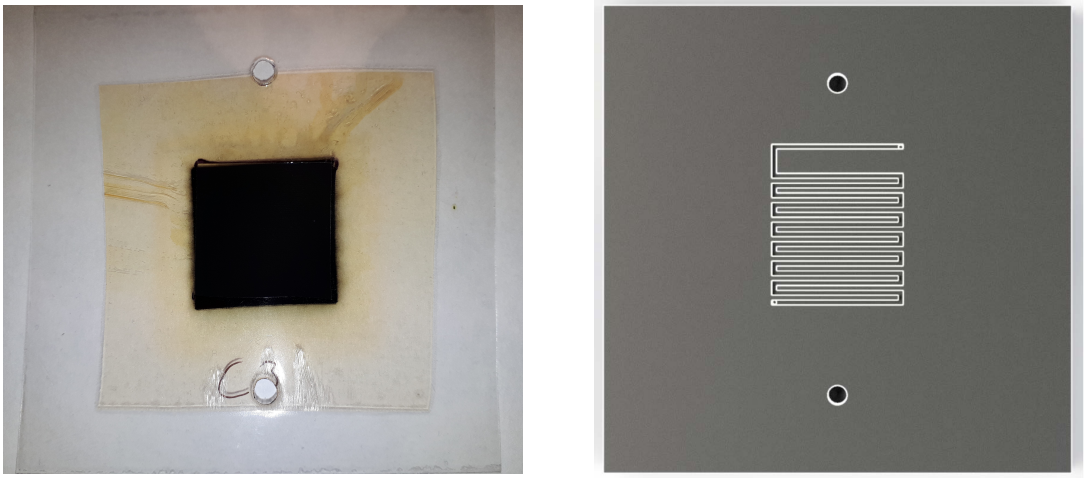

(a) **(b)**

Figure 2.13 – A laminated 5 cm^2 inkjet printed CCM (a) and a 5 cm^2 serpentine flow field bipolar plate (b)

The thickness of the gaskets is determined by the combined thickness of the lamination sheets and chosen GDLs. The pressure applied to the GDL inside the assembly is qualitatively checked with Fujifilm pressure measurement film. Ideally, the raised edges of the flow field channels should be subtly visible on the pressure film where the GDL should be in contact with the catalyst layer. An example of sufficient contact is shown in Figure 2.14. Too much pressure will collapse the porous structure of the GDL and lead to premature mass transport losses and too little pressure will result in higher contact resistance and higher ohmic losses. Large adjustments to the amount of pressure applied can be corrected by changing the gasket and minor adjustments can be corrected by modifying the amount of torque applied to the each bolt. In this work, the type of GDLs and gaskets assembled with a cell are discussed as part of the introduction for each experiment.

Figure 2.14 – Pressure film illustrating proper compression resulting in acceptable contact between the GDL and the flow field

The bipolar plates have a flow field machined into the surface for reactant supply and removal. 5 cm^2 single channel serpentine flow fields, such as that shown in Figure 2.13b, were used for the majority of the experimentation in this work. Noted for their superior performance over parallel flow fields, the design is however difficult to approximate with numerical modelling because gas properties are not uniform in the channel. One exception was for Section 4.3, where a larger 25 cm^2 three channel serpentine flow field was used for a comparison to a literature result.

2.4.4 Characterization

Before any experiments are conducted on a newly assembled fuel cell, it must undergo a conditioning procedure intended to hydrate the membrane and activate the catalyst. Although acknowledged for its importance, there is no standard approach to conditioning a fuel cell [86]. The ESDLab has developed an in-house conditioning protocol that utilizes a combination of constant current and potential cycling. This establishes a baseline for comparing between in-house fabricated MEAs. Unless noted otherwise, the ESDLab's standard conditioning protocol operates the fuel cell for 16 hours at incremental currents ranging from 0.02 to 1.0 A/cm^2 with a cell temperature of 80°C and inlet humidities of 80%. At the conclusion of every hour, an open circuit is applied for 30 seconds before resuming the applied current.

After completing the conditioning, the cells are characterized with a series of galvanostatic polarization curves at a temperature of 80°C and with inlet relative

humidities varying from 50 to 90%. The final reported polarization curve is the average of three curves measured as the current is scanned from 0 A to until the cell exhibits a potential of 0.2 V. A cell resistance is recorded at each data point comprising the polarization curves automatically by the test station using the current interrupt method [87].

Lastly, cyclic voltammetry (CV) is conducted on each cell from which the hydrogen crossover flux and electrochemical surface area (ECSA) can be extracted. A potential is scanned from 0 to 1.2 V and returned to 0 V at a rate of 40 mV/s while the cell is maintained at a temperature of 30°C and fed fully humidified hydrogen and nitrogen. The actual protocols for conditioning, polarization curves, and CVs as well as the theory behind calculating hydrogen crossover and ECSA is summarized in Appendix C.

The information garnered from these tests comprise a basic cell characterization and provide a complete means to compare between different cell constructions. The water balance experiments discussed in the latter part of this work are extraneous tests performed only after the aforementioned tests have been completed.

Chapter 3

Uncertainty Analysis

This chapter details the statistically derived accuracy of the water balance setup based on manufacturer provided accuracies and auxiliary experiments designed to characterize the independent variables of the setup. Section 3.1 outlines the fundamental equations and theory applied throughout this chapter. Sections 3.2, 3.3, and 3.4 detail the systematic and precision uncertainty of the test station flow rate, local pressure, and vapour pressure measured by the setup. The combined uncertainty of each independent variable is then propagated in Sections 3.5 and 3.6 to provide an estimate of the overall uncertainty of the water content and the subsequent net water flux across the membrane as reported by the anode sensors. A discussion on the statistical limitations of the setup is also explored throughout the chapter indicating the optimal conditions for obtaining accurate results.

3.1 Theory

The following uncertainty analysis is based on the procedures outlined by Wheeler (2004) [88] and Taylor (1997) [89]. The uncertainty for a function of multiple measured variables, $f(x_1, x_2, ...)$, is a combination of the individual variable uncertainties. A small perturbation in a dependent variable, δx, is propagated to the global variable by using a Taylor series expansion:

$$\delta f = \delta x_1 \frac{\partial f}{\partial x_1} + \delta x_2 \frac{\partial f}{\partial x_2} + \frac{1}{2}\left(\delta x_1^2 \frac{\partial^2 f}{\partial x_1^2} + 2\frac{\partial^2 f}{\partial x_1 \partial x_2}\delta x_1 \delta x_2 + \delta x_2^2 \frac{\partial^2 f}{\partial x_2^2}\right) + \dots \tag{3.1}$$

Assuming the individual uncertainties are small and uncorrelated, the higher order terms contained within the brackets can be neglected. Furthermore, considering it is not very probable the independent uncertainties will be at their maximum or positive

simultaneously, the Taylor expansion simplifies using least-sum-squares to become [88]:

$$w_f = \left(\sum_{i=1}^{n} \left[w_{x_i} \frac{\partial f}{\partial x_i} \right]^2 \right)^{1/2} \tag{3.2}$$

where w is the overall uncertainty, replacing δ in equation (3.1).

There are two categories of uncertainties, systematic (or bias) and precision (or random). Systematic uncertainties, exhibited as a deviation away from the true mean, arise from the experimental setup (such as equipment offsets and thermal effects) and do not vary with repeated measurements whereas precision uncertainties, seen as a wide standard deviation, arise from unknown random variations in the measurement process. Equation (3.2) is only applicable provided all individual uncertainties were obtained at the same confidence level. Manufacturer provided accuracies are typically for a level of confidence above 95% and while they were likely derived considering both systematic and precision uncertainties, without a clear description of how they are calculated, Wheeler recommends taking a conservative approach and treating manufacturer *accuracies* solely as systematic uncertainties.

Precision uncertainty is defined by a sample set of measurements' distribution around its mean, regardless of whether the central tendency matches the true value of the parameter (accounted for in the manufacturer's accuracy). For system behaviour best described by a Gaussian distribution, the precision uncertainty is statistically described as,

$$P_{\bar{x}} = \begin{cases} t \dfrac{S_x}{\sqrt{N}} & \text{for} N \leq 30 \\ \\ z \dfrac{S_x}{\sqrt{N}} & \text{for} N > 30 \end{cases} \tag{3.3}$$

where, depending on the sample size, N, the t and z scores are taken from their respective probability charts for a given level of confidence, and S_x is the sample standard deviation of the sample mean, $\bar{X}$, calculated as per,

$$S_x = \frac{1}{\sqrt{N-1}} \sqrt{\sum_{j=1}^{N} (X_j - \bar{X})^2} \tag{3.4}$$

Note precision uncertainty is a function of the sample size, decreasing as the number of measurements increases. Despite the steady state operating conditions imposed on the fuel cell, the true behaviour of the cell is dynamic. For example,

liquid water ejection from the diffusion layers is characterized by unpredictable capacitative events. Because the sensors cannot record at a fast enough frequency to capture momentary static behaviour, the precision uncertainty determined from the measurements performed as part of the experiments outlined in Chapters 4 and 5 are based on too small of a sample to reliably describe the system. Instead, for these types of situations, auxiliary experiments, representative of the final experiment, can be performed to capture the random nature of the measurement process and help to further characterize the measurement equipment [88]. The analysis remains the same and the uncertainties from each auxiliary experiment can then be propagated using equation (3.2).

The overall uncertainty for a single independent measurand is then the root sum squared of the two different uncertainties, calculated as per:

$$w_x = \sqrt{B_x^2 + P_x^2} \tag{3.5}$$

where B_x is the systematic uncertainty or the manufacturer's provided accuracy and P_x is the precision or random uncertainty determined from the sample standard deviation of a set of measurements.

3.2 Flow Rate Uncertainty

Scribner Inc. installs MKS Type M100B Mass-Flo® controllers in their test stations. The anode flow controller is calibrated for hydrogen and is limited to flow rates below 2 slpm whereas the cathode flow controller is calibrated for nitrogen and air, and can operate at up to 5 slpm. As previously mentioned, standard conditions for the flow controllers refer to 760 mmHg and 0°C. The manufacturer accuracy for both flow controllers is ±1% of full scale, which includes non-linearity, hysteresis, and non-repeatability. Therefore the anode and cathode have different absolute accuracies; ± 0.020 slpm for the anode and ± 0.050 slpm for the cathode.

Both flow rate calibrations were reviewed with a Gilian Gilibrator-2 bubble calibrator. It carefully measures the time it takes for a bubble, formed as the inputted dry flow rate is passed through a surfactant solution, to travel through a cylinder with a tightly toleranced diameter using a pair of infrared sensors. The calibrator was installed downstream of the test station and recorded 15 measurement samples for different steady state dry mass flow rates. The mean of each sample set was compared to the prescribed set point and the sample standard deviation was calculated as per equation (3.4).

For the anode, each sample set mean fell within the acceptable values determined by the manufacturer's accuracy. The largest sample standard deviation for set anode flow rates less than < 0.8 slpm was 2.16×10^{-3} slpm which corresponded to a precision uncertainty of $\pm 4.63 \times 10^{-3}$ slpm (equation (3.3) with a 95% confidence interval).

Although the water content downstream of the cell has to compensate for the reduction in the dry mass flow rate consumed in the reaction, the accuracy of the current measured by the test station is substantially greater than the flow rate accuracy. Therefore, the current measurements and the resultant dry mass consumption can be treated as absolutes, thereby having a negligible effect on the overall uncertainty of the downstream flow rate. This allows the upstream and downstream flow rate uncertainties to be entirely dependent on the same mass flow controller. As a result, because the water content measured by the setup, defined in equation (2.4), is linearly proportional to the dry mass flow rate, any systematic error introduced by the flow controller is eliminated when taking the difference in equation (2.7) [52]. Note, this only applies when the internal crossover is measured. For simple water content measurements, the bias is reintroduced and the flow rate uncertainty grows.

The uncertainty of the anode flow controller, dependent on the type of measurement, is then:

$$w_{\dot{n}^a_{gas}} = P_{\dot{n}^a_{gas}} = 2.145 \cdot 2.16 \times 10^{-3} = \pm 4.63 \times 10^{-3} \text{ slpm} \tag{3.6}$$

for measuring the internal flux of water across the membrane using equation (2.7) and,

$$w_{\dot{n}^a_{gas}} = \sqrt{B^2_{\dot{n}^a_{gas}} + P^2_{\dot{n}^a_{gas}}} = \sqrt{0.020^2 + (4.63 \times 10^{-3})^2} = \pm 0.021 \text{ slpm} \tag{3.7}$$

for measuring just the water content of a gas stream as per equation (2.4).

For the cathode, the sample means measured using the bubble calibrator for two different flow rate set points failed to fall within the flow controller's accuracy. The recalibration procedure for the flow controllers requires the test station to be returned temporarily to Scribner Inc. and the shipping costs and down time were considered to be too costly. Instead, a calibration curve was generated from 165 measurements taken over the course of 11 different set point flow rates. The curve, shown in Figure 3.1, plots the relationship between the true flow rate outputted from the test station and the set point inputted into the test station software. A correlation equation was generated with the y-intercept forced through the origin as would be expected if the controller was operating correctly:

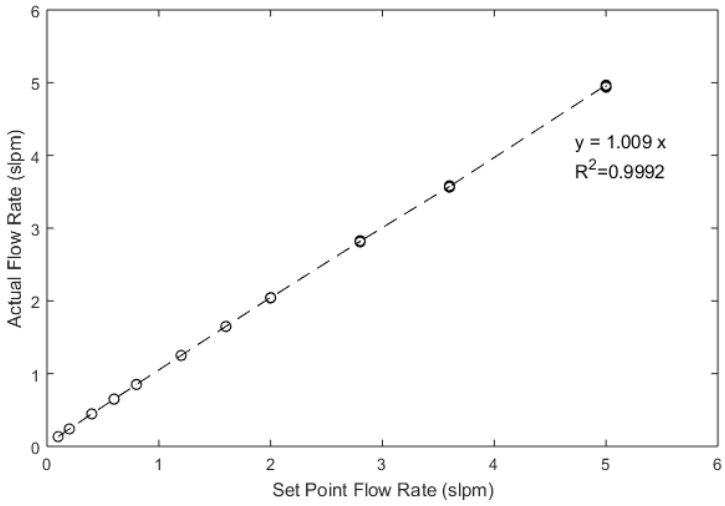

Figure 3.1 – Calibration curve and linear fit for the test station cathode flow controller

$$\dot{m}_{real} = 1.0009\,\dot{m}_{set} \tag{3.8}$$

$$R^2 = 0.9992 \tag{3.9}$$

The uncertainty in the slope was calculated as per equation (3.10) and the accuracy of the flow controller was expressed as an equivalent uncertainty in the slope as per equation (3.11) [89].

$$\sigma_y = \sqrt{\frac{\sum (y_i - Y_i)^2}{n-2}} \tag{3.10}$$

$$\sigma_{ye} = a\,\sigma_x \tag{3.11}$$

Here, y_i is the value measured by the calibrator, Y_i is the value predicted by the correlation equation, a is the slope prescribed by the correlation equation, and σ_x is the uncertainty in the independent variable or for this situation, the cathode flow rate accuracy. The systematic uncertainty in the cathode mass flow rate is then calculated similarly to equation (3.5):

$$B_{\dot{n}^c_{gas}} = \sqrt{\sigma_y^2 + \sigma_{ye}^2} = \sqrt{0.047^2 + 0.050^2} = \pm 0.069 \text{ slpm} \tag{3.12}$$

The largest sample standard deviation for set cathode flow rates less than $<$ 1.75 slpm was 0.012 which corresponded to a precision uncertainty of $\pm$0.027 slpm

(equation (3.3) with a 95% confidence interval). Using the same reasoning discussed for the anode flow rate's uncertainty's dependency on the type measurement being performed, the cathode flow rate uncertainty is best summarized with two values. For measuring the internal flux of water across the membrane using equation (2.7), the overall cathode flow rate uncertainty is:

$$w_{\dot{n}^c_{gas}} = P_{\dot{n}^c_{gas}} = 2.145 \cdot 0.012 = \pm 0.027 \text{ slpm} \tag{3.13}$$

and for just measuring the water content of a gas stream with equation (2.4), the uncertainty becomes:

$$w_{\dot{n}^c_{gas}} = \sqrt{B^2_{\dot{n}^c_{gas}} + P^2_{\dot{n}^c_{gas}}} = \sqrt{0.069^2 + 0.027^2} = \pm 0.074 \text{ slpm} \tag{3.14}$$

The large disparity between the cathode and anode uncertainties further justifies only reporting values based on measurements performed on the anode side of the cell. The larger flow rates experienced in the cathode contribute higher sources of error; a conclusion supported by a sensitivity analysis performed by Kim et al. [31].

3.3 Pressure Uncertainty

OMEGA's MM series custom pressure transducers use piezoresistive silicon pads to measure pressure. They are available with a wide range of pressures, accuracies, operating limits, and functionalities. The exact properties of the two transducers used in this work are summarized in Table 3.1.

The analog output from the transducers is interpreted with an Arduino Genuino analog to digital voltage converter. Because the A/D converter is only rated to maximum of 5 V, the signals from the transducers have to pass through a voltage divider before they can be measured. The voltage divider was assembled with two 10 kOhm (+/-1%) resistors connected to a functional ground shared with the Arduino

Table 3.1 – OMEGA MM Series pressure transducer specifications

Property	**Value**
Range	100 kPa(a)/200 kPa(a)
Output	0-10 Vdc
Accuracy	+/- 0.05%
Fitting	1/4-18 NPT Male
Temp. Compensation	-40 - 105 °C
Thermal Accuracy	+/- 0.30% zero, span

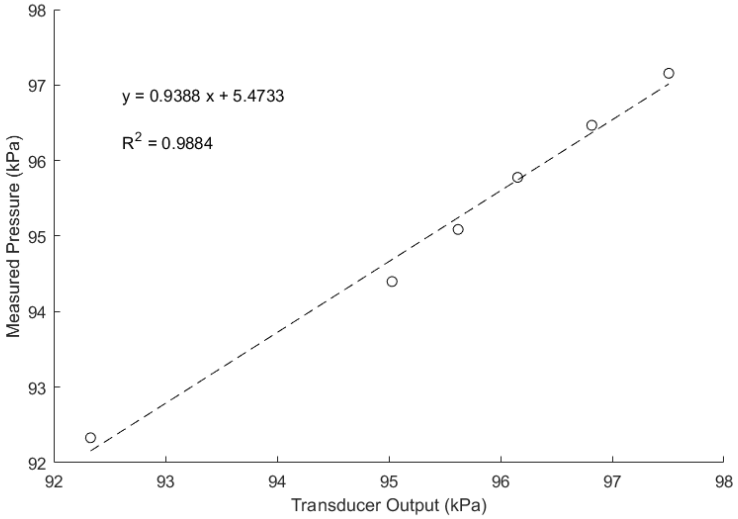

Figure 3.2 – Calibration curve and linear fit for the 100 kPa(a) pressure transducer

and the transducer. Although the transducer has 5-point NIST calibration, subtle differences in the resistance of the resistors and transducer linearity errors can be interpreted by the Arduino as incorrect measurements.

To account for any systematic errors introduced by the acquisition equipment, two independent calibration curves, shown in Figures 3.2 and 3.3, were prepared for the transducers. A Cole Parmer differential pressure controller (model # 00307OX) was installed downstream from a transducer and applied a prescribed back pressure ranging from 0.3 psi to 3.0 psi relative to atmospheric pressure (0.3 psi was the lowest back pressure attainable) . The 100 kPa(a) transducer could only accommodate back pressure up to 0.7 psi before exceeding its upper operating limit.

The output from the transducer was compared to the sum of the applied back pressure reported by the controller and the barometric pressure measured by a generic barometer installed in a Samsung smartphone (previously calibrated with a mercury barometer). In the absence of inclement local weather, barometric pressure fluctuates on the order of 0.1 kPa over the course of an hour. Therefore, the barometric pressure will appear constant with small enough time samples. For the calibration curves, each data point represents the average taken from pressure measurements recorded every 2 seconds for 30 seconds.

The uncertainty in the linear fit was found using the same approach discussed in Section 3.2. Equation (3.10) was applied to each data set and equation (3.11) was based on the absolute uncertainty of each transducer, taken as the accuracy

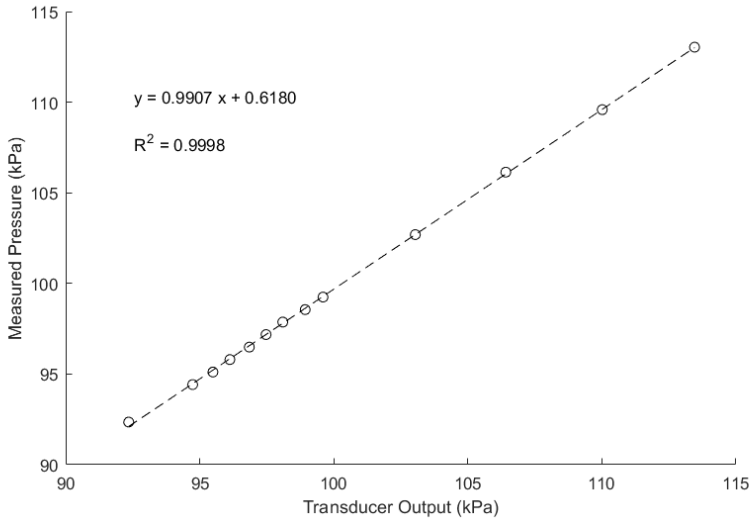

Figure 3.3 – Calibration curve and linear fit for the 200 kPa(a) pressure transducer

percentage of the full scale. Therefore the bias uncertainty of each transducer was found to be,

$$B_{P_{100kPa}} = \sqrt{\sigma_y^2 + \sigma_{ye}^2} = \sqrt{0.476^2 + 0.047^2} = \pm 0.478 \text{ kPa} \tag{3.15}$$

$$B_{P_{200kPa}} = \sqrt{\sigma_y^2 + \sigma_{ye}^2} = \sqrt{0.346^2 + 0.099^2} = \pm 0.360 \text{ kPa} \tag{3.16}$$

The precision uncertainty was derived using equation (3.3) from the largest sample standard deviation of all the different data sets for each transducer. The resultant overall uncertainties were determined to be:

$$w_{P_{100kPa}} = \sqrt{B_{P_{100kPa}}^2 + P_{P_{100kPa}}^2} = \sqrt{0.478^2 + 0.088^2} = \pm 0.486 \text{ kPa} \tag{3.17}$$

$$w_{P_{200kPa}} = \sqrt{B_{P_{200kPa}}^2 + P_{P_{200kPa}}^2} = \sqrt{0.360^2 + 0.137^2} = \pm 0.385 \text{ kPa} \tag{3.18}$$

These uncertainties are largely dependent on the quality of the voltage dividers used to report their measurements. A 0-10V DAQ in place of the Arduino board would greatly reduce the uncertainty. However for this work, unless specified otherwise, the 200 kPa pressure transducer was used because of its lower uncertainty.

3.4 Vapour Pressure Uncertainty

The Sensirion SHT75 determines the relative humidity by correlating the change in capacitance of a dielectric material to the amount of moisture absorbed onto the surface and therefore to the humidity of the surrounding atmosphere. The temperature is measured using a silicon bandgap temperature sensor which correlates the change in the ambient temperature to a change in voltage across a junction of a silicon diode. Although the two phenomena are coupled, their measurements are performed independently.

The typical accuracies of the sensor reported by the manufacturer are ± 1.8% and ± 0.3°C. However these values change as the sensor is exposed to conditions that approach the extreme operating limits of the sensor. In a discussion with Sensirion technical representatives, the relative humidity accuracy was amended to ± 2.0 % for all temperatures above 40°C. For the same temperature range, the temperature accuracy is approximated with equation (3.19), extrapolated from figures provided in the sensor specification documents.

$$w_T = 0.02\, T_{gas} - 0.4 \tag{3.19}$$

In theory, for vapour pressure and water content measurements, any localized temperature differences near the sensors is compensated by the coupled behaviour of temperature and relative humidity. Although the temperature and relative humidity of an enclosed atmosphere may not appear stable, that may not apply to the vapour pressure and therefore the water content as illustrated in Figure 3.4. Previously thought instabilities smooth out. Rather than quantify the precision uncertainties of temperature and relative humidity independently, they were extrapolated together using equations (2.3) and (2.6), to find the vapour pressure uncertainty. To do so, the vapour pressure of an enclosed atmosphere exposed to a saturated salt solution was compared to the anticipated vapour pressure calculated from the temperature and relative humidity values reported by L. Greenspan [90].

Two saturated salt solutions were chosen; potassium carbonate and potassium chloride. Potassium carbonate was chosen because it exhibits a stable relative humidity of approximately 43.16% at and around room temperature, which is representative of dry and low temperature conditions. A more accurate empirical fit for the relative humidity at temperatures between 0 and 30°C is as follows [90]:

$$\mathrm{RH}_{K_2CO_3} = 43.1315 + 0.00147523\, T_{soln} \tag{3.20}$$

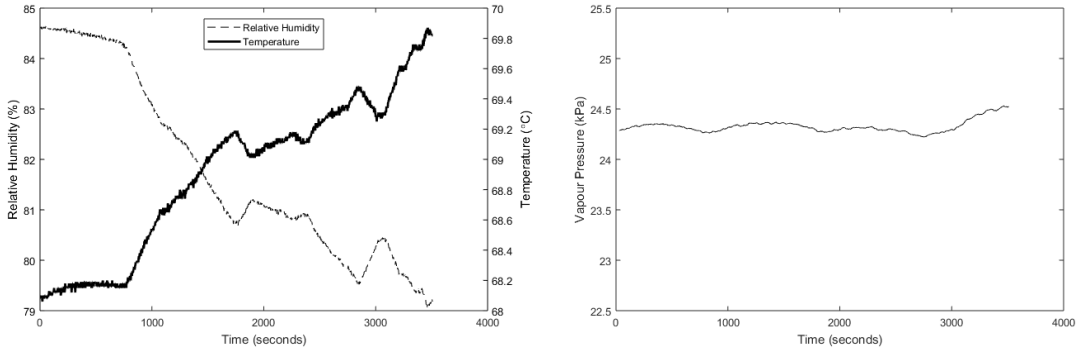

(a) **(b)**

Figure 3.4 – Behaviour of the atmosphere above a sealed saturated salt solution of potassium chloride over the course of an hour. Relative humidity and temperature exhibit mirrored behaviour (a) which is not extended to vapour pressure (b)

Conversely, potassium chloride was chosen because it exhibits a higher relative humidity of 78-80% for temperatures between 60 and 90°C, conditions similar to those expected during regular testing. More specific relative humidities for temperatures ranging from 0 to 90°C were calculated using the following empirical fit [90]:

$$\mathrm{RH}_{KCl} = 88.6190 - 0.193340\, T_{soln} + 0.899706 \times 10^{-3}\, T_{soln}^2 \tag{3.21}$$

A third flask containing Drierite, a desiccant, was briefly used to ensure the sensor did not have a zero offset.

The saturated salt solutions were prepared by mixing each granular salt with heated distilled water until the salt no longer dissolved and began to form a paste. The sensor and a T-type thermocouple were passed through a rubber stopper. The sensor was positioned arbitrarily above the solution and the thermocouple was lowered just enough for a meniscus to come in contact with tip of the thermocouple probe, capturing the temperature of the solution at the liquid/gas interface. The solutions were then left overnight, with the potassium carbonate solution placed on the counter at room temperature and the potassium chloride placed in an oven with an approximate temperature of 72.5°C.

Afterwards, both temperatures and the relative humidity were monitored until it appeared the environment had reached equilibrium. For both solutions, the solution temperature measured by the thermocouple and an OMEGA HH506 thermometer was stable, fluctuating occasionally on the order of $\pm$ 0.1°C. The average temperature was recorded and used in the aforementioned empirical equations (3.20) and (3.21) to determine the expected relative humidity and resultant vapour pressure. Similarly,

Table 3.2 – Vapour pressure measured above saturated salt solutions

Property	**Potassium Carbonate**		**Potassium Chloride**	
	Thermocouple	SHT75	Thermocouple	SHT75
Temperature	25.0°C	25.34°C	71.4°C	71.51°C
Relative Humidity	43.2%[1]	44.12%	79.4%[1]	84.16%
Vapour Pressure[2]	1.4 kPa	1.43 kPa	26.3 kPa	28.02 kPa
Percent Difference	2.1%		6.5%	

1: Calculated using equations (3.20) and (3.21)
2: Calculated using equation (2.3)

the Sensirion SHT75 recorded the temperature and relative humidity every 3 seconds with the results used to determine the vapour pressure. Both sets of results are summarized in Table 3.2.

The vapour pressure precision uncertainty was determined from the random variation in the measurements after each system had reached equilibrium. Equations (3.3) and (3.4) were applied to the two data sets with the results summarized in Table 3.3.

The relative uncertainty of the potassium chloride solution, normalized to the size of measured value, was chosen for future calculations. The bias uncertainty of the vapour pressure can be calculated by applying equation (3.2) to equation (2.6). From observation, the highest uncertainty will occur at large saturation pressures, which is a function of temperature, and high humidities. The same hot and wet operating conditions previously mentioned.

$$B_{P_{vap}} = \sqrt{(B_{P_{sat}}\ \mathrm{RH})^2 + (B_{RH}\ P_{sat})^2} \tag{3.22}$$

Recall the experimental approach outlined in Section 2.1. The individual uncertainties for each measurand have to be propagated through each calculation using equation (3.2) to determine the accuracy of the setup. Applying this methodology to equation (2.3), the partial derivative of the saturation pressure with respect to the gas temperature measurement is:

Table 3.3 – Precision uncertainty of vapour pressure measurements

	Potassium Carbonate	**Potassium Chloride**
Mean	1.43 kPa	28.02 kPa
Std. Dev.	0.002	0.117
Sample Size	63	47
Uncertainty, $P_{P_{vap}}$	$\pm 3.92 \times 10^{-3}$ kPa ($\pm$0.27%)	$\pm$0.23 kPa ($\pm$0.82%)

$$P_{sat} = c \exp[a\ b] \tag{3.23}$$

$$\frac{dP_{sat}}{dT_{gas}} = c \exp[a\ b]\left[\left(-\frac{b}{234.5}\right) + \left(\frac{257.14\ a}{(257.14 + T_{gas})^2}\right)\right] \tag{3.24}$$

where a, b, c are defined as,

$$a = 18.678 - \frac{T_{gas}}{234.5} \tag{3.25}$$

$$b = \frac{T_{gas}}{257.14 + T_{gas}} \tag{3.26}$$

$$c = 0.61121 \tag{3.27}$$

The saturation pressure's dependency on the exponential of the gas temperature complicates the uncertainty analysis because the exponential is retained after the derivative is performed. Therefore, as illustrated in Figure 3.5, the uncertainty changes as the measured temperature fluctuates, with higher temperatures contributing to a progressively larger absolute uncertainty.

As an example, consider that 85°C is the warmest temperature the sensors are expected to experience (5°C above max cell temp.). At that temperature, the bias uncertainty of the saturation pressure will be less than or equal to:

$$B_{P_{sat}} = w_T \frac{dP_{sat}}{dT_{gas}} \leq 1.3 \cdot 2.27 \leq \pm 2.95 \text{ kPa} \tag{3.28}$$

The 2% relative humidity accuracy provided by Sensirion does not change depending on the magnitude of the humidity measurement. Should the gas leaving the fuel cell heated to 80°C reach full saturation, at a gas temperature of 85°C, this corresponds to a relative humidity of approximately 82%.

$$B_{P_{vap}} \leq \sqrt{(2.95 \text{ kPa} \cdot 82\%)^2 + (2\% \cdot P_{sat,85°C})^2} \leq \pm 2.68 \text{ kPa } (\pm 5.65\%) \tag{3.29}$$

Combining the bias uncertainty with the previously measured precision uncertainty finds the overall uncertainty in the vapour pressure at those conditions to be:

$$w_{P_{vap}} = \sqrt{(2.68 \text{ kPa})^2 + (0.82\% \cdot 47.4 \text{ kPa})^2} \leq 2.72 \text{ kPa } (\pm 5.74\%) \tag{3.30}$$

This represents the highest absolute vapour pressure uncertainty expected under typical operating conditions. Note that higher relative uncertainties will occur

Table 3.4 – Summary of uncertainties of independent variables

Measurand	Sensor		Uncertainty
Anode Mass Flow Rate, $w_{\dot{n}^a_{gas}}$	2.0 slpm MKS Type M100B	$\pm$	0.0046 slpm
Cathode Mass Flow Rate, $w_{\dot{n}^c_{gas}}$	5.0 slpm MKS Type M100B	$\pm$	0.027 slpm
Vapour Pressure, $w_{P_{vap}}$	Sensirion SHT75	$\leq$	2.72 kPa
Pressure, w_P	OMEGA MM Series 200 kPa(a)	$\pm$	0.385 kPa
Current, w_I	Scribner 850e Test Station	$\pm$	0 A

at lower vapour pressures because the vapour pressure is not linearly dependent on temperature. For an estimate of different vapour pressure uncertainties refer to Figure 3.6. The analysis detailed in this section has been extended to three different cell temperatures (60, 70, 80°C), assuming in each instance the gas temperature is heated 5°C above the cell temperature, with values decreasing away from complete saturation. A polynomial fit was generated for each condition correlating the relative uncertainty to the actual vapour pressure:

$$w_{P_{vap,60°C}} = 0.0113\, P_{vap}^2 - 0.489\, P_{vap} + 10.11 \tag{3.31}$$

$$w_{P_{vap,70°C}} = 0.0082\, P_{vap}^2 - 0.480\, P_{vap} + 12.43 \tag{3.32}$$

$$w_{P_{vap,80°C}} = 0.0054\, P_{vap}^2 - 0.441\, P_{vap} + 14.85 \tag{3.33}$$

3.5 Water Content Uncertainty

Table 3.4 contains a summary of the individual independent uncertainties for each measurand of interest.

Continuing with the application of equation (3.2) to equation (2.4), the overall absolute uncertainty in the water content of a gas stream detected by the setup is given as,

$$w_{\dot{n}_{H_2O}} = \left[\left(w_{\dot{n}_{gas}} \frac{P_{vap}}{P_\infty - P_{vap}}\right)^2 + \left(w_{P_{vap}} \frac{\dot{n}_{gas}\, P_\infty}{(P_\infty - P_{vap})^2}\right)^2 + \left(-w_P \frac{\dot{n}_{gas}\, P_{vap}}{(P_\infty - P_{vap})^2}\right)^2\right]^{1/2} \tag{3.34}$$

with the relative uncertainty found using,

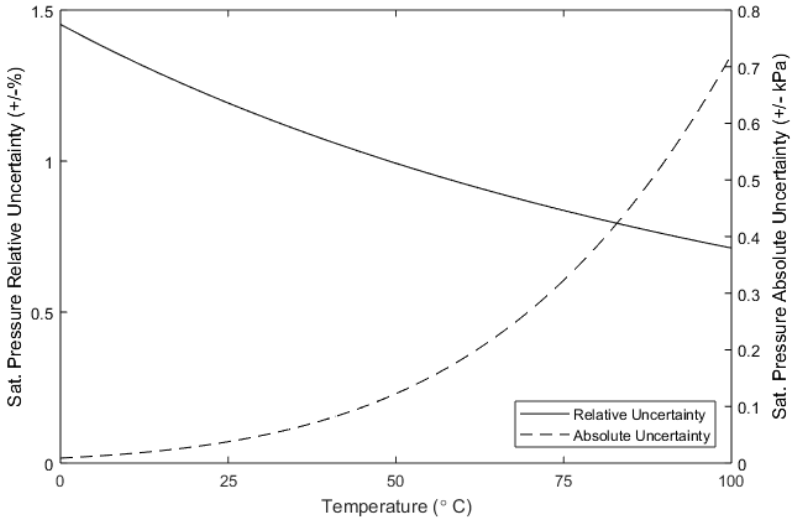

Figure 3.5 – Relative and absolute uncertainty of the saturation pressure at different temperatures

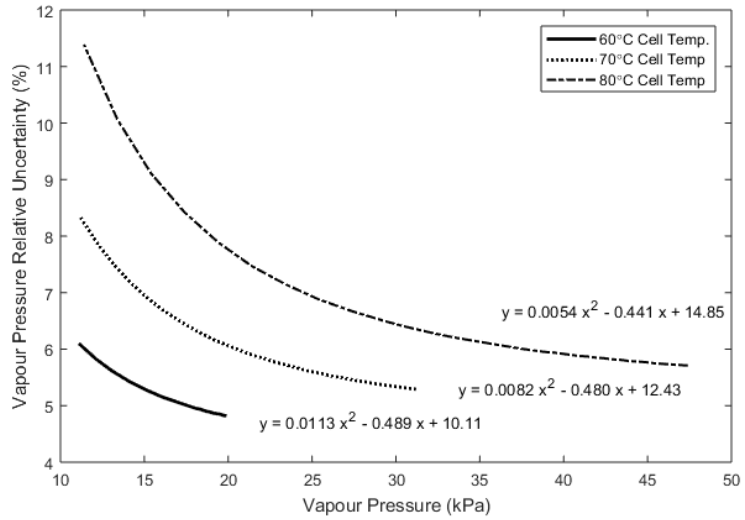

Figure 3.6 – Vapour pressure relative uncertainty as a function of the vapour pressure extrapolated from measurements taken at three different temperatures

$$\frac{w_{\dot{n}_{H_2O}}}{\dot{n}_{H2O}} = \left[\left(\frac{w_{\dot{n}_{gas}}}{\dot{n}_{gas}}\right)^2 + \left(\frac{w_{P_{vap}}}{P_{vap}}\,\frac{P_\infty}{P_\infty - P_{vap}}\right)^2 + \left(\frac{w_{P_\infty}}{P_\infty}\,\frac{P_\infty}{P_\infty - P_{vap}}\right)^2\right]^{1/2} \tag{3.35}$$

From observation, the largest relative uncertainty occurs at low flow rates, ambient pressures, and at high vapour pressures. This is confirmed by the trend illustrated in Figure 3.7, which plots the relationship between the barometric pressure and vapour pressure. More specifically, these conditions occur when the anode flow rate is 0.1 slpm (the lowest operational limit), a measurement temperature of 85°C, complete saturation, and a barometric pressure of 91 kPa. Note these are the extreme limits expected during operation. For the given conditions, the highest relative uncertainty for the water content in a gas stream is,

$$\frac{w_{\dot{n}_{H_2O}}}{\dot{n}_{H2O}} \leq \left[\left(\frac{0.0046 \text{ slpm}}{0.1 \text{ slpm}}\right)^2 + \left(0.0574\,\frac{91 \text{ kPa}}{91 \text{ kPa} - 47.41 \text{ kPa}}\right)^2 + \left(\frac{0.385 \text{ kPa}}{91 \text{ kPa} - 47.41 \text{ kPa}}\right)^2\right]^{1/2} \tag{3.36}$$

$$\frac{w_{\dot{n}_{H_2O}}}{\dot{n}_{H2O}} \leq \sqrt{(4.6\%)^2 + (12.0\%)^2 + (0.9\%)^2} \leq \pm 12.9\% \tag{3.37}$$

This is the upper limit of the overall uncertainty. The conditions it was determined from would rarely appear during routine experimentation. However because the relative humidity and temperature fluctuate and the saturation pressure uncertainty is a function of the temperature, a single uncertainty would not be representative of the accuracy of the system. As will be discovered in Chapters 4 and 5, reported values are accompanied with a relative uncertainty calculated at their respective conditions.

However using relative uncertainties provides insight into which variables contribute the largest inaccuracies and therefore identify the areas which should be improved upon first for the most efficient means of improving the setup. Equation (3.37) shows the limiting parameter is the measurement of vapour pressure, measured with the SHT75 sensor. Using a more accurate sensor such as the SHT35 discussed in Appendix A, would lower the uncertainty in the water content to $\leq$6.5%. These initiatives were noted and investigated but time constraints and technical difficulties prevented them from being implemented. Ultimately for this work, the Sensirion SHT75 meets all requirements and the accuracy of the vapour pressure measurements is acceptable.

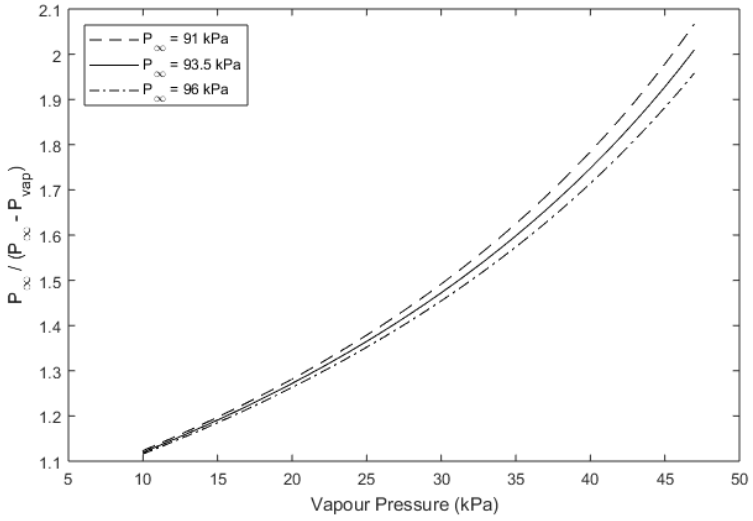

Figure 3.7 – Ratio of barometric pressure to the partial pressure of air at different barometric and vapour pressures

3.6 Net Water Crossover Uncertainty

The net crossover flux can be imagined as a difference in the vapour pressure and dry molar flow rate across the anode.

$$\dot{n}_{crossover} = \dot{n}_{H_2O,A,i} - \dot{n}_{H_2O,A,o} \tag{3.38}$$

$$\dot{n}_{crossover} = \dot{n}_{gas,i} \frac{P_{vap,i}}{P_{\infty,i} - P_{vap,i}} - \dot{n}_{gas,o} \frac{P_{vap,o}}{P_{\infty,o} - P_{vap,o}} \tag{3.39}$$

In practice, the two terms of the mathematical difference are of similar magnitude. This imposes a significant penalty on the uncertainty of the crossover. By taking the difference, the result tends to be smaller than its constituent parts but the uncertainty compounds as per equation (3.2)

$$w_{crossover} = \sqrt{w^2_{\dot{n}_{H2O,A,i}} + w^2_{\dot{n}_{H2O,A,o}}} \tag{3.40}$$

As the net crossover flux approaches zero, the accuracy of the setup tends towards infinity, creating a practical lower limit to the amount of crossover that can be confidently reported. Although not applicable to equation (3.39), this is best visualized in Figure 3.8 as a plot of the relative uncertainty of the crossover reported by cathode overlaid with the magnitude of the crossover. An asymptote develops where the net crossover flux changes direction. At very low net crossovers, a definitive direction

cannot be determined but the acknowledgement that water transport is approaching equilibrium is often more important. To further complicate this matter, the lower limit changes depending on the operating conditions. Figure 3.9 contains similar uncertainty plots for anode measurements based on different operating parameters.

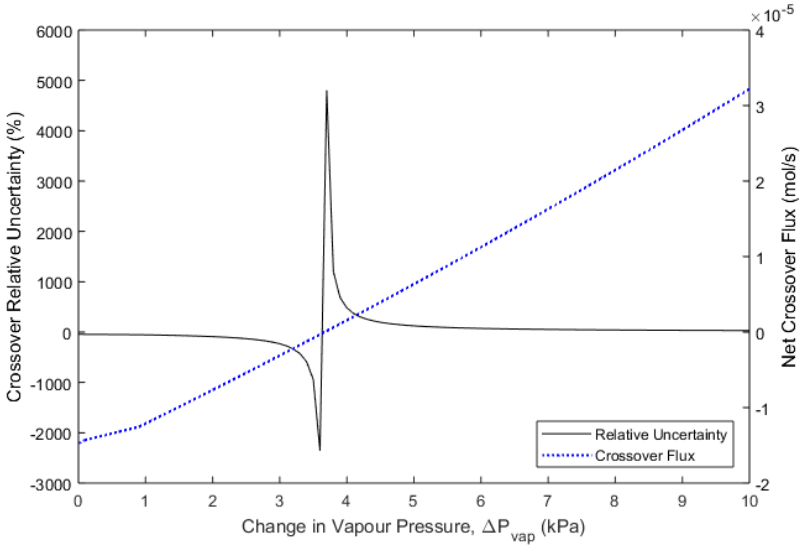

Figure 3.8 – Relative uncertainty of crossover taken from cathode measurements demonstrating asymptotic behaviour as crossover approaches zero.

From Figure 3.9, one can evaluate the influence of different operating parameters on the final reported crossover value. For example, as water transitions from one side of the cell to the other, the vapour pressure across the inlet and outlet of the anode changes accordingly. The extent of the change depends on the stoichiometry ratio of the gas entering the cell, to the effect of how diluted the crossover magnitude is relative to the molar flux of water entering the cell. At very high stoichiometries, the amount of water crossing the membrane may be indiscernible from the noise generated as large volumes of water enter the cell, therefore low stoichiometries are preferable.

The change in dry molar flow rate, stated in equation (2.7), is a function of the current applied to the cell. Faraday's law predicts hydrogen and oxygen are consumed at a ratio of 2:4 per amp respectively. The larger the current applied, the greater the difference in dry flow rate between the inlet and outlet, the greater the difference in equation (3.39), and the lower the overall uncertainty.

These are suggestions and at times it may be necessary to perform measurements that may contribute to less than desirable uncertainties. The crossover values reported later in this work have their respective uncertainties tailored to their specific operating conditions, calculated following the process outlined in this chapter.

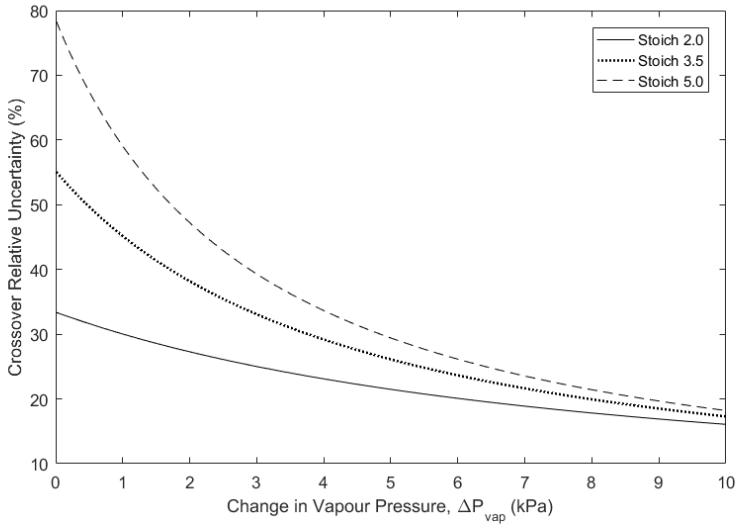

(a) Changing flow rates: 70°C cell temp, 1.0 A/cm^2, 5 cm^2

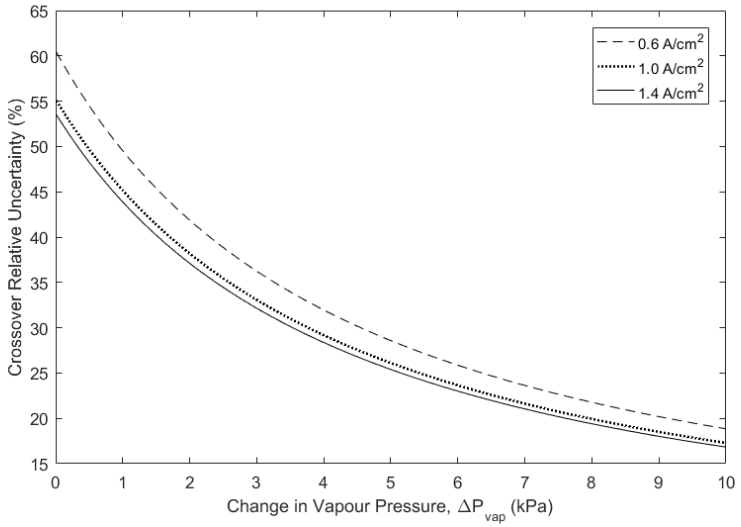

(b) Changing current: 70°C cell temp, 3.5 wet stoich, 5 cm^2

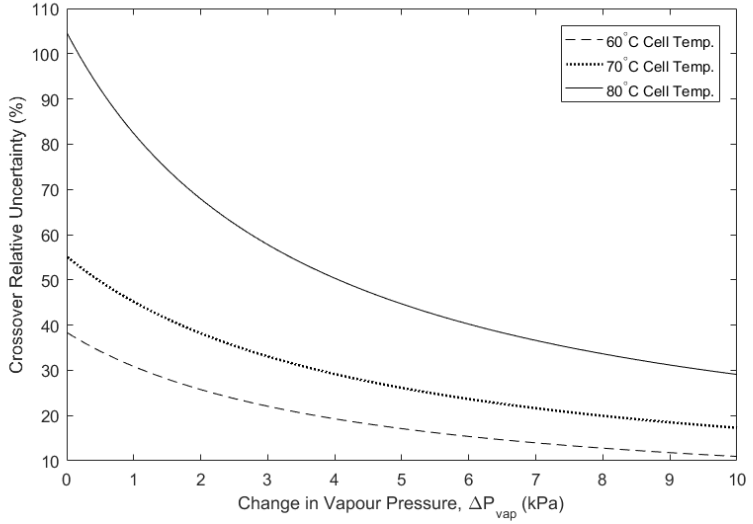

(c) Changing cell temperatures: 1.0 A/cm^2, 3.5 wet stoich, 5 cm^2

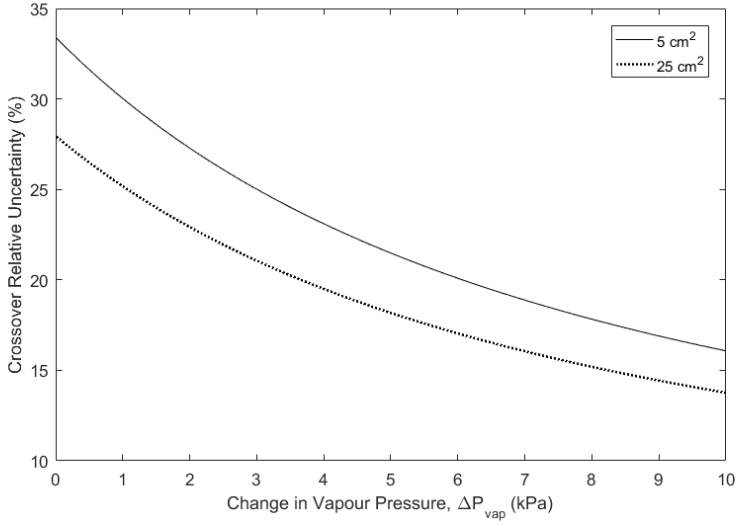

(d) Changing cell size: 70°C, 1.0 A/cm^2, 2 wet stoich

Figure 3.9 – Dependency of crossover uncertainty relative to different operating parameters

3.7 Summary

Performing measurements of the net crossover flux, as will be seen in following chapters, is a time intensive process. The first such experiment typically takes on the order of 3 - 4 hours with subsequent experiments taking slightly less time as the humidifiers and water bath no longer require time to warm up. The dynamic nature of the fuel cell and unpredictable behaviour of the test station humidifiers further complicates gathering large sample sets of measurements for the same experiment. As such, single-measurement experiments were preferred throughout this thesis with the exception of one small sample sized repeatability experiment performed in Section 4.3.

The recommended method for propagating uncertainties is to propagate only systematic uncertainties through the equations and perform multiple-measurement experiments to directly quantify the precision uncertainty of the final measurement. This precision uncertainty would account for the individual precision uncertainty contributions of each measurand and capture, more accurately, how those individual uncertainties interact with each other. For the experiments performed throughout Chapters 4 and 5, the length of time required to perform a single-measurement made this method unrealistic.

Rather, the individual precision uncertainties corresponding to each measurand were quantified with auxiliary experiments and propagated together with their respective systematic uncertainties through the equation process to provide a conservative estimate of the setup's accuracy. A small sample sized repeatability study performed in Section 4.3 found the precision uncertainty of a net crossover measurement to be $\pm$ 2.2%. This result shows the potential precision uncertainty of the setup however as it was only based upon three measurements, a more comprehensive precision uncertainty investigation should be performed. Completing this study would reduce the uncertainty of net crossover flux measurements, however the conservative estimate provided by the aforementioned analysis was considered sufficient enough for this work.

Chapter 4

Experimental Validation

The previous chapter discussed the theoretical behaviour of the water balance setup considering it as a composite of different instruments. This chapter explores the physical behaviour of the setup as a whole compared to experimental metrics based on physical laws and from previously published work. Section 4.1 demonstrates the water balance setup's ability to accurately measure the water vapour content entrained in a gas stream. Cumulative totals are also shown to be in good agreement with condensed values. Section 4.2 compares crossover values reported by the anode and cathode sensors, confirming all water entering and leaving an operating fuel cell is accounted for. Section 4.3 then draws direct parallels to a previously published study [54] investigating water flux across Nafion NR211 membranes. This section also details the ability of the setup to capture transient behaviour and demonstrates the full capacity of the water balance setup.

4.1 Water Collection

Prior to conducting any investigations, the setup's capacity to accurately measure the water content of a gas stream was verified. Foremost was to ensure the sensors are, at large, correctly identifying the amount of water leaving the test station and that the test station is operating properly.

To do so, gas, with an established temperature and flow rate, was routed from the test station immediately into the water balance setup and then passed through a forced air condensing unit. No fuel cell was included. Three results were then compared with each other; the theoretical water content based on the supposed test station set points, the results extrapolated from the sensor measurements, and the combined mass of the condensed water and the water vapour retained in the room temperature exhaust stream.

The theoretical calculations were modelled after the equations outlined in Section 2.1 under the assumption the dew point leaving the test station matches the set point temperature. With that assumption in place, the gas should be saturated when it exits the test station with the saturation pressure at the set point being equivalent to the vapour pressure. Calculations based on the test station inputs determined the theoretical molar flow rate of water leaving the station, $\dot{n}_{H_2O}$, and the cumulative water that should be collected downstream of the condenser, N_{H_2O}, given a certain experimental duration and assuming the gas vented from the condensing unit is fully saturated at room temperature (25°C). Scribner Associates Inc. independently verified this assumption.

Gas from the test station was passed immediately through the water balance setup. The measurements were saved in a comma-delimited file and processed with a spreadsheet. They were calculated in a similar manner to the theoretical values except the vapour pressure was calculated as per equation (2.6) and the discrete measurements were integrated over their sampling rate and summed over the experimental duration.

The gas then passed from the water balance setup and into the forced-air condensing unit before being evacuated through the drain, which was held open. A hose leaving the drain of the condensing unit was directed through a rubber stopper and terminated inside a vented erlenmeyer flask. Any liquid water condensed from the gas stream was collected inside the flask and the remaining gas was passed unencumbered through the flask port and dispersed into the surrounding room. For that reason, nitrogen was chosen in favour of hydrogen. An additional SHT75 sensor was placed at the flask's side arm to capture the water profile of the gas leaving the condenser. As expected, the dew point of the vented gas matched the ambient temperature of the room, reaffirming the previous assumption.

Prior to recording any measurements, the fully heated and humidified gas stream was passed directly through the condensing unit, allowing it to reach a quasi-steady state, where for every water droplet entering the condensing unit, another droplet exited the drain. This was performed for one hour before starting the experiment to prevent any accumulation of water from previous experiments from influencing the following experiment's results.

At the start of the experiment, dry flasks were placed at the drains and removed immediately upon its conclusion. The collected water was then transferred to a glass beaker and the contents were weighed on a Denver Instruments SI-603 scale.

The entire process was performed once for the three different temperatures noted in Table 4.1. Measurements were only recorded for the anode mass flow controller and humidifier. The water balance setup has the same sensors on both sides removing

Table 4.1 – Operating parameters for water collection validation

Condition	Value
Gas Temperature[1]	64, 71, 77 °C
Duration[1]	3, 2, 2 hours
Flow Rate	1.75 slpm
Pressure	Ambient
Gas	Nitrogen

1: Written as experiment # 1, 2, 3

the need to perform the same measurements on the cathode side. To minimize the influence of systematic errors, such as evaporation or adhesion to the flask wall, and large fluctuations in the water content during startup and shutdown, it was decided a minimum of 50 g of water should be collected. The results from the experiment are summarized in Table 4.2.

Of utmost importance is the discrepancy between the measured and collected masses of water. Liquid water collection has been pursued extensively in literature because, provided an appreciable amount can be collected, its accuracy is unparalleled for steady state measurements. For this situation, the mass of collected water was considered the true value. The main drive behind this water balance setup is to be capable of replicating liquid water collection whilst also capturing transient events. Therefore, the close agreement between the two results confirms it is capable of meeting the first requirement.

The water content uncertainty at such high flow rates ranges from +/- 6.1% to 9.5% as the gas temperature is increased. This corresponds to a resolution on the order of grams, not the tenth of a gram reported in Table 4.2, indicating the setup is likely more accurate than the uncertainty analysis concluded. Publications that utilize water collection often report water balances that agreed to within 95% [31, 58].

This uncertainty explains the subtle difference between the measurements and the collected masses of water. In addition, some of the difference can also be attributed to the discrete liquid water ejection events from the condensing unit. This is visually

Table 4.2 – Results from water collection validation experiment

	#1	#2	#3
Predictions	77.5 g	76.4 g	129.9 g
Measurements	75.3 g	60.3 g	131.5 g
Collected	75.6 g	61.1 g	131.7 g

apparent. On some of the transparent tubing, one can see the walls of the tubing slowly begin to collect liquid water until a certain threshold is reached, where upon a droplet sheds from the wall, clearing any further water adhered to the walls downstream. These events are largely unpredictable, both in mass and time. Placing the flask at the drain at the immediate start of the experiment may capture an ejection event that was produced prior to the experiment with the opposite possible when the flask is withdrawn.

In all three cases, the predictions based on the test station set points poorly match the other two outcomes. These values are indicative of how poorly the test station captures the correct temperature and humidity. Often the average dew point leaving the test station can be upwards of one degree below or above the set point. This is illustrated quite clearly in Table 4.3 which compares the average dew point measured in the three different experiments to their respective set point. This was what originally prompted the addition of the bypass loops. Utilizing them when testing on a fuel cell removes the dependency on the test station. Although they are not a perfect solution as they can under evaluate the water content because of trace amounts of water which ultimately condense inside the bypass lines or recirculate and condense inside the dead ends of the tees and fuel cell, they do provide a superior evaluation of the water entering the cell.

Figure 4.1 is a plot of the behaviour of the gas at each set point over the duration of the experiment. Note gas temperature is the temperature measured inside the sensor housing, not the set point temperature prescribed by the test station. Although the test station may not accurately heat the gas, Figure 4.1d demonstrates the vapour pressure is stable once the test station has achieved steady state. Monitoring the temperature and relative humidity over time are then not as imperative given fluctuations in either tend to offset each other. Table 4.4 summarizes the variation in the vapour pressure after the half hour mark of the experiment. In comparison to the bias uncertainty calculated in Section 3.4, the variation in the vapour pressure is negligible. Furthermore, it is independent of the set point temperature. This small variation allows the measurement of the vapour pressure of gas entering the cell prior to performing a crossover experiment and to assume it is constant thereafter.

Table 4.3 – Comparison between test station set point and measured dew point

Set Point	Measured Dew Point
64°C	63.46°C
71°C	69.94°C
77°C	77.36°C

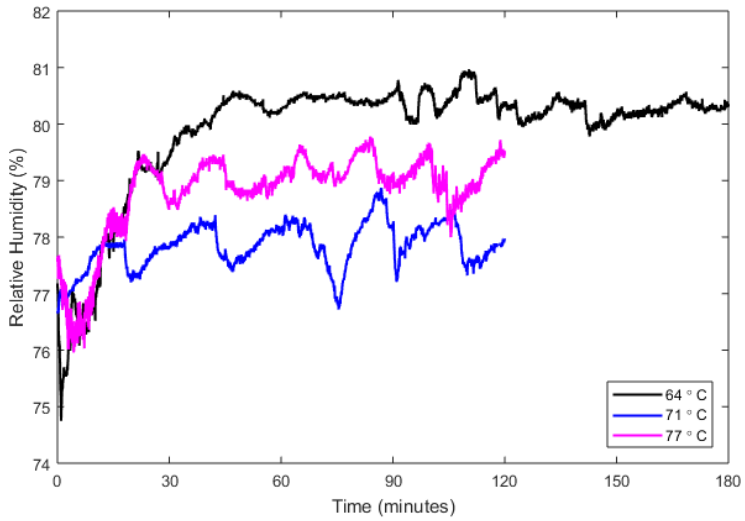

(a) Relative Humidity

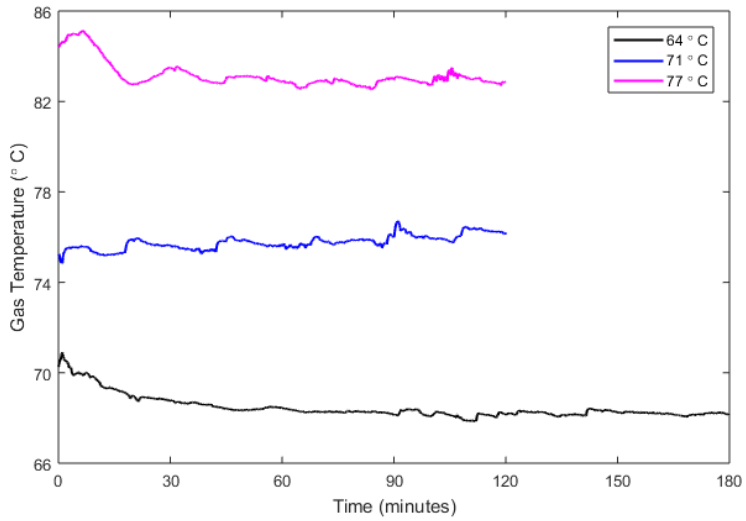

(b) Gas Temperature

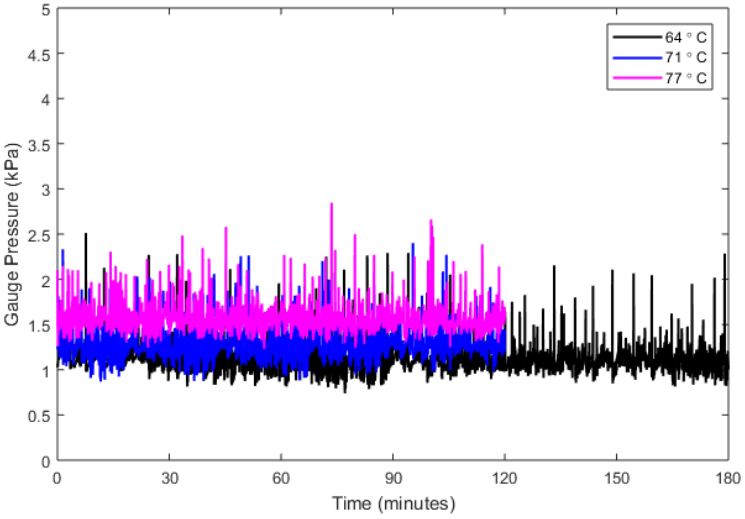

(c) Gauge Pressure

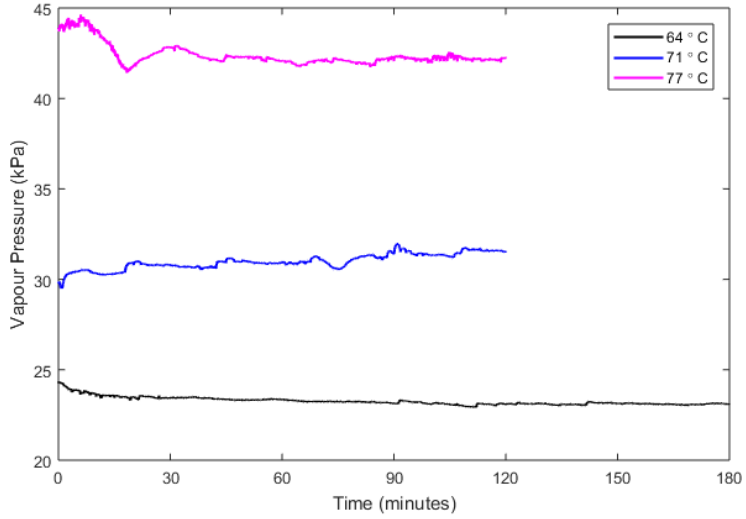

(d) Vapour Pressure

Figure 4.1 – Measured behaviour of the gas leaving the test station when operated at steady state (Nitrogen at 1.75 slpm)

Table 4.4 – Variation in the vapour pressure of the gas leaving the test station measured with the water balance setup when operating at steady state

Set Point	Vapour Pressure Mean	Variation (2x σ)
64°C	23.20 kPa	0.24 kPa (± 1.03%)
71°C	31.13 kPa	0.68 kPa (± 2.18%)
77°C	42.20 kPa	0.40 kPa (± 0.95%)

4.2 Conservation of Mass

The net crossover reported as throughout this work is usually based exclusively on measurements recorded from the anode. This simplifies the calculations, removing the need to consider the water generated from the reaction, and improves the accuracy of the final reported crossover value because the anode flow controller has a smaller uncertainty. However in theory, the crossover measured by the anode and cathode should be equivalent, with small variations permitted to account for transport limitations inside the cell. Although some quantitative measurements of the net crossover flux in literature are extrapolated exclusively from anode measurements [31, 49, 59], this is not universal [13, 42, 44, 45, 47, 48, 51, 58]. The simplified calculations and less data intensive measurements favour calculations based on the anode but including the cathode can provide further confirmation of results.

An experiment was performed to ensure all the water entering and leaving the fuel cell was accounted for by the sensors and that the anode and cathode reported the same results. Leak testing the setup with a surfactant solution confirmed the entire setup was gas tight. Therefore the only mass transport to consider was internal hydrogen and water crossover, reactant consumption, water generation, and bulk movement through the setup.

The cell assembly was chosen as an approximation of the in situ measurements of water transport performed by Adachi et al. [54]. The mass conservation experiment, performed three times, was performed with the conditions summarized in Table 4.5. These conditions defined by a concentration gradient and high EOD, were chosen to encourage water transport towards the cathode; a conclusion supported by Adachi et al's findings [54].

Prior to beginning the experiment, a commercially available 5 cm^2 IonPower MEA with a symmetric loading of 0.3 mg_{Pt}/cm^2 and an NR211 PEM was assembled with SGL 28BC GDLs and single serpentine flow channels. The cell underwent a slightly modified cell characterization from that outlined in Appendix C. The results are shown in Figure 4.2. The conditioning was performed as usual however the higher

current density steps were modified to accommodate the poor initial performance of the IonPower MEA. The cell was operated at a single current density of 0.8 A/cm^2 rather than the typical 0.9 and 1.0 A/cm^2 steps. The polarization curves were performed at a cell temperature of 80°C with 50 kPa(g) of back pressure applied and wet stoichiometric ratios of 2 and 6 for the anode and cathode. A wet stoichiometry differs from the traditional dry stoichiometry in that it accounts for the displacement of the reactant with water vapour based on the ratio of partial pressures between the dry gas and water vapour. Compared to previous results attained by inkjet printed CCMs prepared at the ESDLab, the performance is quite poor despite having a cathode platinum loading 2-3 times higher. The minimum acceptable potential at a current density of 1.0 A/cm^2 for ESDLab CCMs is 0.45, 0.50, and 0.55 V for 50%, 70%, and 90% inlet humidities respectively. The IonPower CCM's performance at the same humidities was 0.39, 0.46, and 0.50 V respectively.

The hydrogen crossover extrapolated from the CV was 1.09×10^{-8} mol/(cm^2 s). Adachi et al. [54] reports the minimum magnitude of water crossover reported for a cell exposed to similar operating conditions to be approximately 2.0×10^{-6} mol/(cm^2 s). Although hydrogen that crosses the membrane is destined to form water at the cathode electrode, the amount that is generated and the diatomic hydrogen lost from the anode is negligible relative to the amount of hydrogen entering the cell and the water generated from proton transfer.

The water content of the gases entering the fuel cell were categorized beforehand by redirecting flow around the fuel cell through the bypass lines. At this stage, the test station had been operating for about 1 hour to provide sufficient time for the humidifiers to warm to their respective set points. Figure 4.3 illustrates the dew point of the inlet gases leading up to the first experiment. Only the measurements after the dew point had stabilized were averaged and from there, were assumed unchanged throughout the duration of the experiment (as per Figure 4.1d).

The anode and cathode pressure were measured with an Omega MM Series 100 kPa absolute and 200 kPa absolute pressure transducer respectively. The barometric pressure, needed for monitoring the water vapour vented from the condensing unit, was monitored with a digital barometer found in a Samsung Galaxy A5 smartphone that was consistent with the reading from a traditional mercury barometer.

The water collection basins inside the condensing unit were emptied before the experiment and again, into separate beakers, at the immediate conclusion of the two and a half hours. The mass of water was then weighed with Denver Instruments SI-603 scale. Whereas before, when the drains were left open during the experiment, for this experiment, the anode drain had to be closed because hydrogen could not

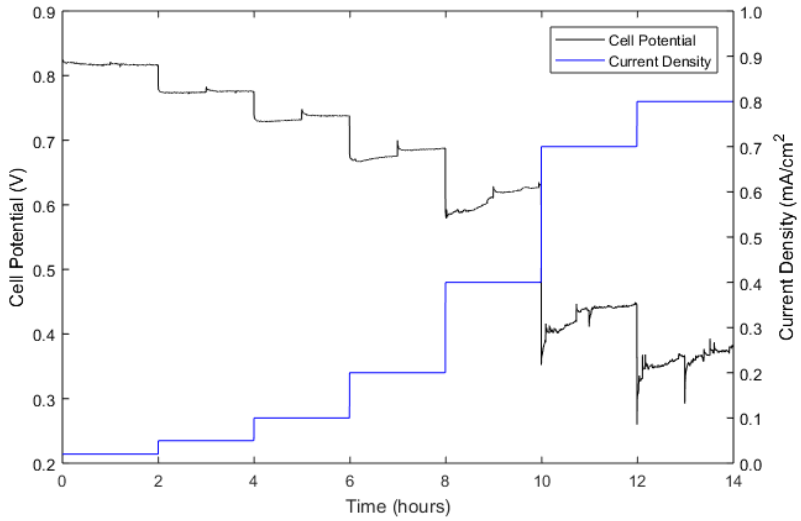

(a) Cell conditioning (80°C, 80% RH, 0 kPa(g))

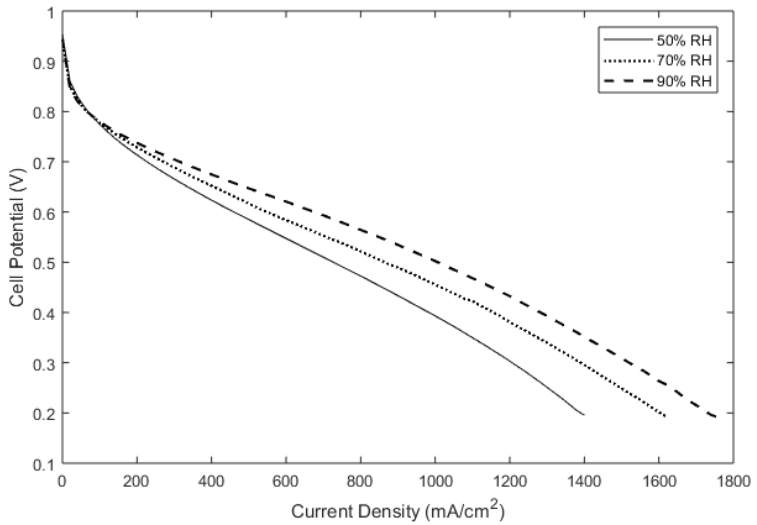

(b) Polarization curves (80°C, varying RH, 50 kPa(g))

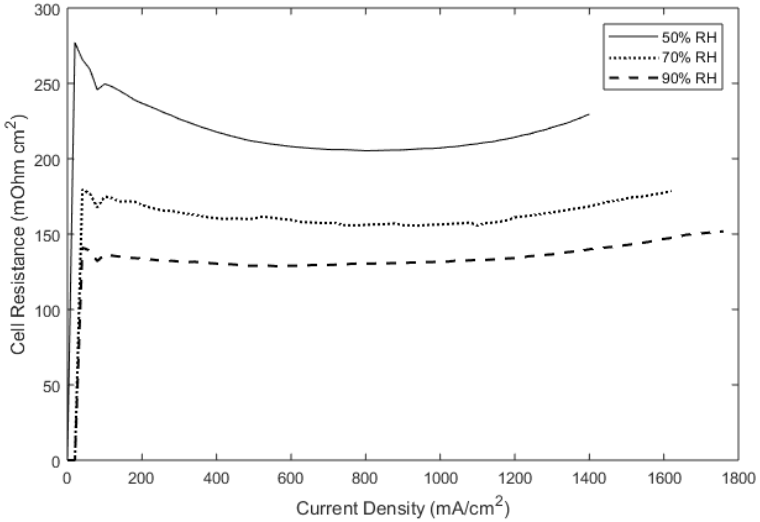

(c) Cell resistance (80°C, varying RH, 50 kPa(g))

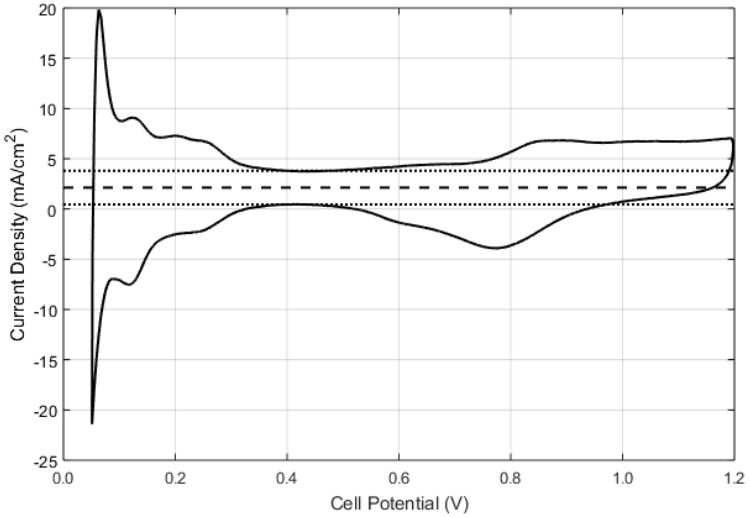

(d) Cyclic Voltammetry (30°C, 100% RH, H_2/N_2, 40 mV/s)

Figure 4.2 – Complete characterization of commercial IonPower 5 cm^2 CCM used for setup validation

Table 4.5 – Parameters for validating conservation of mass and crossover

Condition	Value
Cell Temperature	70 °C
Anode Humidity	100%
Cathode Humidity	40%
Anode Flow Rate	0.25 slpm
Cathode Flow Rate	0.50 slpm
Pressure	Ambient
Current Density	1 A/cm^2
Duration	2.5 hours

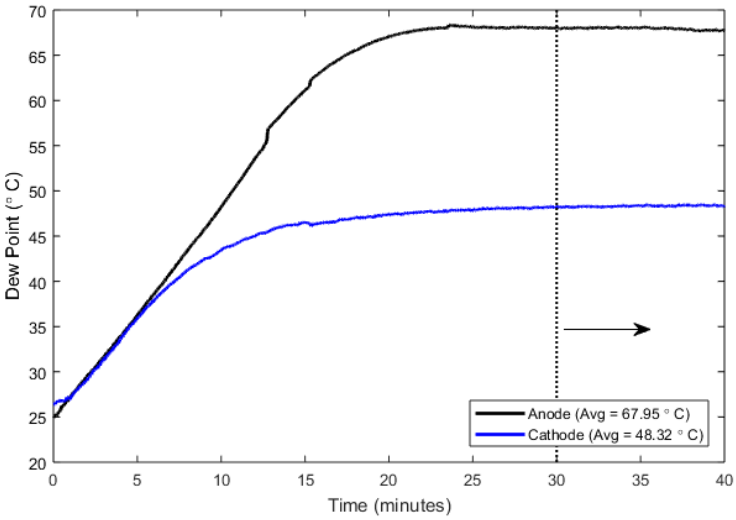

Figure 4.3 – Dew point of the gases entering the fuel cell. Anode was set to 70°C and cathode was set to 50.2°C. Vertical dashed line indicates time after which results were reported

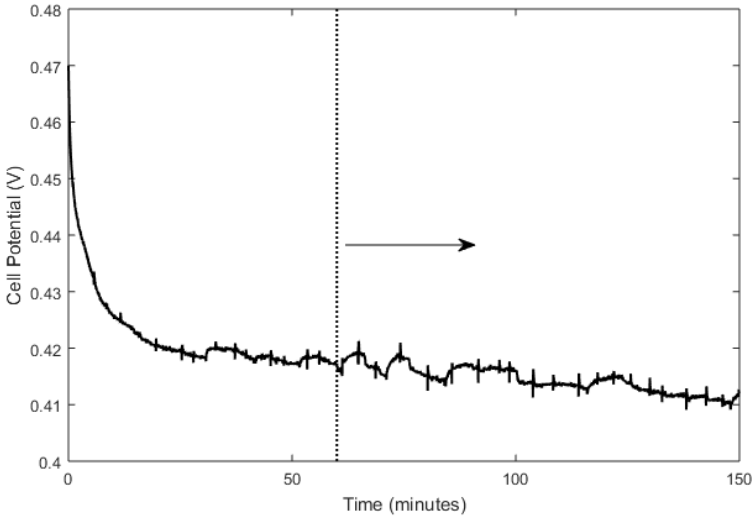

Figure 4.4 – Measured cell potential during experiment # 3. Vertical dashed line indicates time after which results were calculated

Table 4.6 – Comparison of anode and cathode derived crossover measurements

	Anode Crossover		**Cathode Crossover**	
	(mol/(m^2 s))	[α]	(mol/(m^2 s))	[α]
1	0.0355	[0.69]	0.0351	[0.68]
2	0.0330	[0.64]	0.0304	[0.59]
3	0.0259	[0.50]	0.0227	[0.44]

be vented into the lab. This is not ideal. With the drain closed, there is no way to confirm all the water retained in the auxiliary piping inside the unit has managed to reach the collection basin and that it has passed through the drain.

Although the test parameters were unchanged during the experiment, the fuel cell required some time to acclimatize to whichever conditions were imposed upon it. Only values after this acclimatization period were averaged; defined as any measurement recorded after the 60th minute. This specific time frame was chosen to maintain consistency with Adachi et al. [54]. It is best illustrated from a plot of cell potential as seen in Figure 4.4.

The average net water crossover values recorded during each experiment are summarized in Table 4.6. Adachi et al. [54] reported crossover values of approximately 0.025 mol/(cm^2 s) for a similar experimental setup. As expected, within the same experiment, the anode and cathode crossover values fall within each other's uncertainties. The uncertainty for anode measurements ranged from 50.0% to 65.1% while

the cathode uncertainty ranged from 34.3% to 48.6%. These values are very large due to the high initial humidity of the anode and the poorer performance of the cathode sensing. The uncertainty is more reasonable in Chapter 5.3 where the inlet anode humidity is lowered to 40% RH.

Note the uncertainties reported are predominately influenced by equipment bias so for a given set of operating conditions, the uncertainty applies equally to each set of measurements, offsetting the mean value. The variation and oscillations of the data are unaffected and represent the true behaviour of the system.

Although the membrane acts a permeable boundary for water between the anode and cathode, the instantaneous measurements captured by the water balance setup do not show mirrored behaviour. Prominent changes in the water ejected from one side of the cell were not always reflected on the other side. Figure 4.5 plots the instantaneous crossover corrected to the amount of water generated for both the anode and cathode captured during the first experiment. A large ejection measured at the half hour mark on from the cathode did not correspond to any changes in the anode measurements at the same time. Although the control volumes are coupled, the porous structure of the electrodes, adsorption capacity of the membrane, and distance between the membrane-catalyst layer interface and the humidity sensors prevent instantaneous comparisons between the anode and cathode.

At approximately the 180th minute, the anode shows a general increase in the crossover towards the cathode whereas measurements reported from the cathode show the opposite. At the same time, there is no discernible change in cell potential or resistance. The cause for this behaviour cannot be determined as the magnitude of the difference away from the average is approximately 3% and outside the resolution of the setup. Similar can be said for the noise and oscillations exhibited in both sets of measurements.

In all three cases, the crossover reported by the anode sensors exceeds that reported by the cathode sensors. From observation of equation (3.39), this may be indicative of some measure of condensation prior to the gas being measured by the sensor, causing the crossover reported by the anode to appear larger than it truly is. Furthermore, the same behaviour on the cathode side would artificially lower the cathode reported crossover. The true crossover is likely between the two values reported in the table. The reason this behaviour is not detected by the setup is unknown. The largest difference between anode and cathode crossover values is 0.0032 mol/(m^2 s) which amounts to 0.26 cumulative grams of water over the duration of the experiment. It may be possible that such a small amount of water may find residence in a region that does not experience sufficient recirculation or shearing force from the

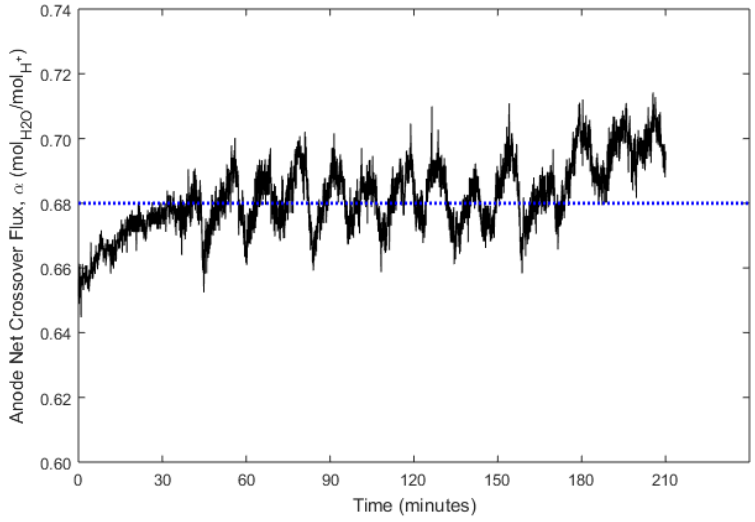

(a)

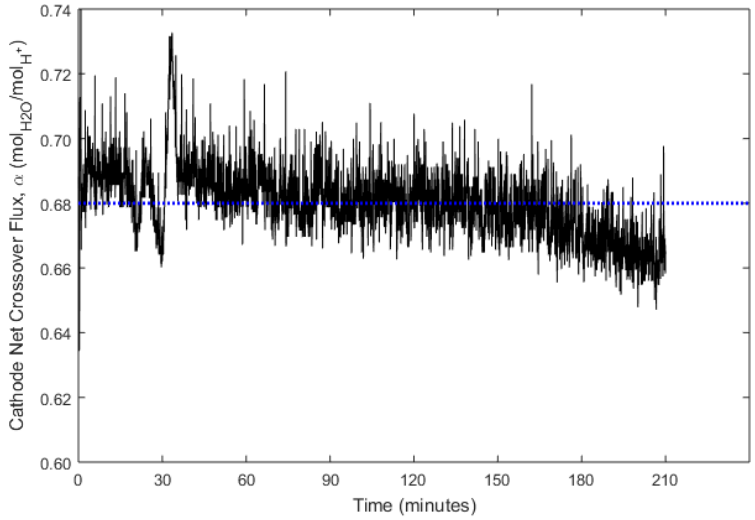

(b)

Figure 4.5 – Molar flux of water crossing the membrane for the first experiment from the perspective of the anode (a) and cathode(b) normalized to the amount of water produced. Blue line indicates an average of $\alpha = 0.68$

Table 4.7 – Comparison between the mass of water measured passing the sensors to the amount condensed and collected downstream of the condensing unit

	# 1	# 2	# 3
Cathode Measured (g)	13.39	12.67	12.66
Cathode Collected (g)	11.21	13.92	13.64
Discrepancy (g)	**2.18**	**-1.25**	**-0.98**
Anode Measured (g)	9.51	8.93	8.71
Anode Collected (g)	11.20	10.57	10.63
Discrepancy (g)	**-1.69**	**-1.64**	**-1.92**

remaining gas stream to eject past the sensors.

This conclusion is supported by the results in Table 4.7 where comparisons between the setup's measurements and the mass of liquid water condensed from the gas stream indicate the setup has, in most cases, under-evaluated the amount of water contained in the gas stream. The magnitude of the discrepancy is far greater than the results from Section 4.1 and the 0.26 g unaccounted for by the sensors. Based on the variation of the vapour pressure reported in Section 4.1, a change in the assumed vapour pressure entering the cell could explain an additional 0.55 g while it should also be noted the water collected from the anode was performed with the drain closed during experimentation, calling into question whether 100% of the water was collected. Additionally, there is auxiliary piping between the fuel cell and water bath that was not present in Section 4.1 that may contribute to additional condensation. With the high flow rates, the residence time may be too short for the gas to evaporate before passing the sensors.

Interestingly, the net crossover does not appear to be solely a function of the cell operating conditions. Crossover values reported in Table 4.6 for the three experiments were performed at the same current density and humidification. One might have expected the reported crossover values to be of closer value. These differences in net crossover are accompanied with other changes in the cell's behaviour such as a difference in cell potential and resistance. Because the cell had not been disassembled between experiments, the change in cell resistance, shown in Table 4.8, provides insight into the hydration state of the membrane. Lower cell resistances are correlated with a higher absorbed water content as the membrane conductivity increases, as does its thickness as it swells, possibly further reducing contact resistances. The smaller changes in vapour pressure measured in each successive experiment are demonstrative of the increase in the amount of water retained by the cell. A clear reason for the change in hydration state between experiments has not been noted although the membrane may not have fully hydrated during conditioning.

Table 4.8 – Change in steady state cell parameters during mass conservation validation experiment

	Anode ΔP_{vap} (kPa)	Cathode ΔP_{vap} (kPa)	Cell Potential (V)	Cell Resistance (mOhm)
1	1.78	8.30	0.385	29.869
2	1.73	8.13	0.365	27.279
3	0.86	7.20	0.415	26.627

4.3 Literature Comparison

The final step in experimentally validating the water balance setup was to reproduce results previously reported in literature. Despite increasing interest in water management of PEMFCs, the work presented in Adachi et al. [54] is one of a very few publications that can be fully replicated with the equipment and resources available in the ESDLab.

In the work of Adachi et al., the flux of water across a Nafion NR211 membrane generated from a hydraulic or concentration gradient with an ex situ setup is compared to the crossover measured from in situ water balance experiments in an attempt to classify the type of permeation experienced during regular cell operation. They concluded, based on the magnitude of the in situ measured crossover, that liquid-vapour permeation, defined as liquid water in contact with one side of the membrane and fully saturated vapour on the other side, is the dominant transport behaviour across an MEA during cell operation. They speculate liquid water builds up at the cathode electrode interface, generating a significant chemical potential gradient that offsets the EOD and encourages some water to return to the anode.

Adachi et al. [54] presented a plot of the net water flux at increasing current densities under two different conditions; (i) wet anode/dry cathode and (ii) dry anode/wet cathode. The results confirm the previously established conclusion that back diffusion dominates at lower current densities and EOD dominates at higher current densities, giving the plot a quadratic appearance as the current density is increased. For the first case (i), Adachi et al. states the transition between the two transport mechanisms occurs between 0.4 and 0.6 A/cm^2 where the magnitude of the net water flux ranges from approximately 0.018 mol/(m^2 s) at its lowest to 0.051 mol/(m^2 s) at its greatest. The same transition is not as apparent for case (ii) as current driven EOD and concentration driven back diffusion offset each other. Consequently, the magnitude of the net water flux is also smaller, ranging only from approximately -0.015 mol/(m^2 s) to -0.027 mol/(m^2 s).

Both cases were replicated for experimental validation of the water balance setup.

Table 4.9 – Cell architecture comparisons for Adachi et al. [54] literature validation

Parameter	Validation Experiment	Adachi et al. [54]
Catalyst	TKK 46.7% wt_{Pt}	N/A
Ionomer Solution	5% wt Nafion	
Membrane	Nafion NR211	
Fabrication Method	Doctor-bladed	Spray-coated
Catalyst Loading	0.45-0.48 mg_{Pt}/cm^2	0.35-0.40 mg_{Pt}/cm^2
Ionomer Loading	30% wt	
Surface Area	25 cm^2	
Flow Field	Triple serpentine	
GDL	SGL 24BC	
Gaskets	152 μm fibreglass reinforced PTFE	125 μm compressible silicone

Two independently fabricated cells were studied. The first was used throughout the validation and the second cell was used periodically to ensure repeatability. All conditions and parameters, where possible, were kept the same as Adachi et al.'s work. The most noteworthy difference between the two works was the fabrication method of the CCM. Adachi et al. used an automated spray coater to deposit an undefined carbon-supported platinum, methanol, and water suspension onto a Nafion NR211 membrane for a final loading of 0.35-0.40 mg_{Pt}/cm^2 per side. For the validation experiment, two 25 cm^2 CCMs were fabricated by doctor-blading an ink slurry comprised of 46.7% wt platinum supported on carbon black (Tanaka Kikinzoku Kogyo K.K.), Nafion suspension, propylene glycol, and isopropyl alcohol across a PTFE substrate before being decal transferred onto a Nafion NR211 membrane with a hot press. The final loading of the first CCM was 0.45 mg_{Pt}/cm^2 for both the anode and the cathode and the second CCM was 0.48 mg_{Pt}/cm^2. Potentially adverse differences arising from the different fabrication techniques include the type of carbon support, differences in loading, and the microstructure of the electrode.

Another difference arose with the cell assembly. The same GDL (SGL 24BC) and 25 cm^2 triple serpentine flow fields (Fuel Cell Technologies) were used however 152 μm fibreglass reinforced PTFE gaskets were used in place of the 125 μm compressible silicone gaskets employed in ref. [54]. By using a thicker gasket, the GDL does not experience the same compression and therefore maintains more of its original volume and porosity at the possible expense of a slightly higher contact resistance. Excessive compression of the GDL contributes to higher mass transport losses as the porosity of the GDL proportionally decreases. A side by side comparison of the different cell constructions is summarized in Table 4.9.

Figure 4.6 plots the results from the initial cell characterization of the second doctor-bladed cell. Both doctor-bladed cells underwent the standard cell characterization outlined in Appendix C with the exception of replacing the 0.7 and 0.9 A/cm^2 current steps with 0.6 and 0.8 A/cm^2. The polarization curves were recorded with current increments of 0.5 A, held for 45 seconds at each point. No back pressure was applied. The results presented are the average of three curves generated as the cell was swept from low to high current densities. The cell resistance was measured with the current interrupt method during the polarization curves. Lastly, the CV was generated with the protocol noted in Appendix C.

The cell understandingly outperforms the CCM tested in Section 4.2 and the metric established for the ESDLab's low loaded inkjet printed electrodes; largely attributed to the $\geq 60\%$ larger platinum loading. The hydrogen crossover was measured to be 7.00 $\times 10^{-9}$ mol/(cm^2 s), comparable to other Nafion NR211 based CCMs. This remains negligible in comparison to protonic water generation and the inlet flow rates.

Additional polarization curves, shown in Figure 4.7, were performed to replicate the polarization curves published in Adachi et al. [54]. The cell temperature was 70°C and the anode and cathode were similarly defined as (i) wet/dry and (ii) dry/wet respectively for two different experimental conditions. Wet was defined as an RH $\geq$ 100% (dew point of approximately 75°C) and dry was defined as an RH = 40%. Excessive flooding during initial attempts to supersaturate the anode stream similar to ref. [54] were unsuccessful, prompting the polarization curves and crossover experiments for the doctor-bladed cells to be operated at a wet humidity of 100% instead.

Hydrogen and air were supplied with wet stoichiometries of 2.0 and 3.0 for the anode and cathode, with a minimum flow rate of 0.25 slpm for both to prevent reactant starvation at low current densities. The polarization curve was conducted in galvanostatic mode with 2 A increments held for 3 minutes each. This was chosen in place of potentiostatic 50 mV increment polarization curve used in ref. [54] because galvanostatic mode is inherently more stable. The test station is more adept at maintaining a constant electronic load than imposing a certain potential on the cell whose behaviour tends to fluctuate. As a result of using large current steps, the curves exhibit kinks that are not seen in other polarization curves with a finer current resolution.

The polarization curves published by Adachi et al. [54] and reproduced in Figure 4.7 was the average from eight individual curves. The polarization curves presented as part of this work were averaged from three curves taken as the cell was swept from low to high currents.

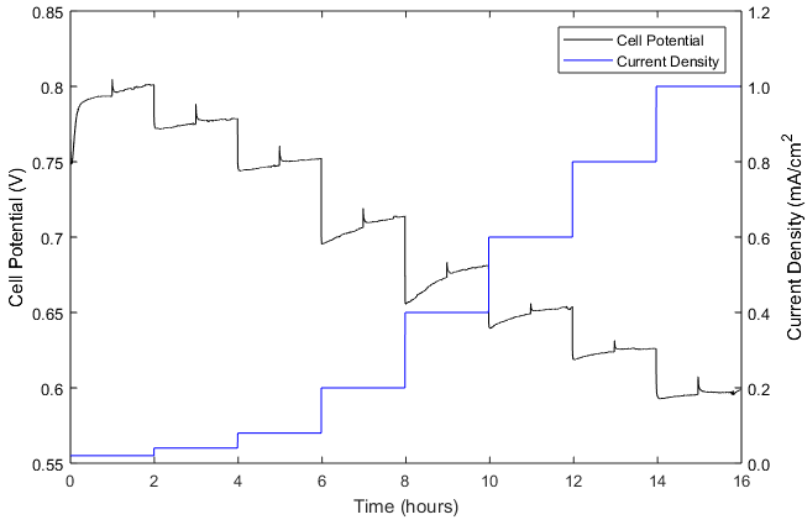

(a) Cell conditioning (80°C, 80% RH, 0 kPa(g))

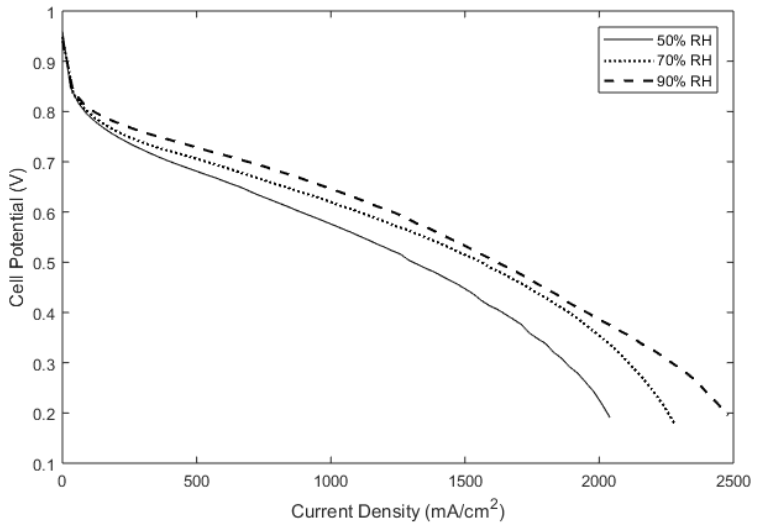

(b) Polarization curves (80°C, varying RH, 0 kPa(g))

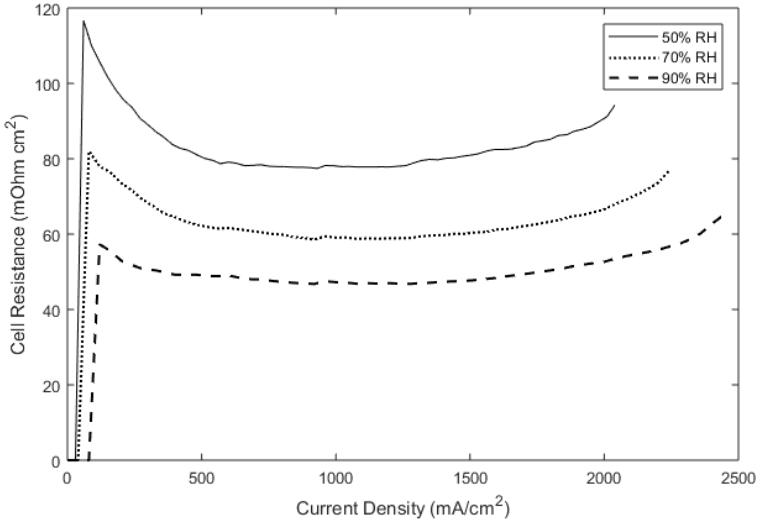

(c) Cell resistance (80°C, varying RH, 0 kPa(g))

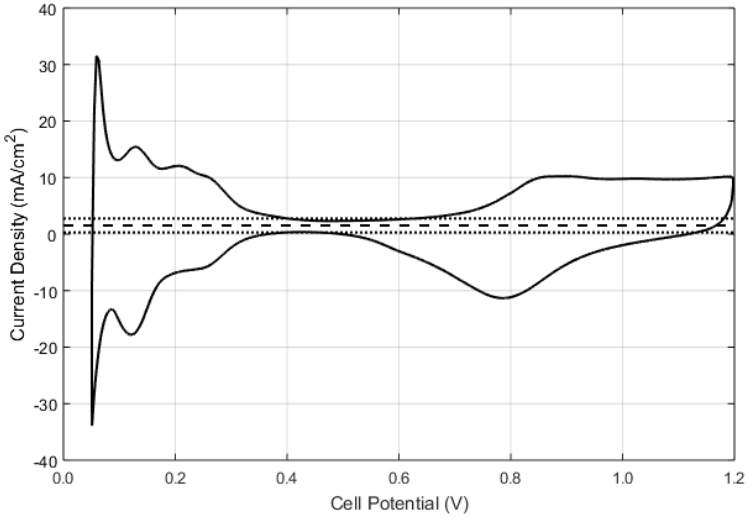

(d) Cyclic Voltammetry (30°C, 100% RH, H_2/N_2, 40 mV/s)

Figure 4.6 – Complete characterization of in-house doctor-bladed 25 cm^2 CCM used for literature validation with Adachi et al. [54]

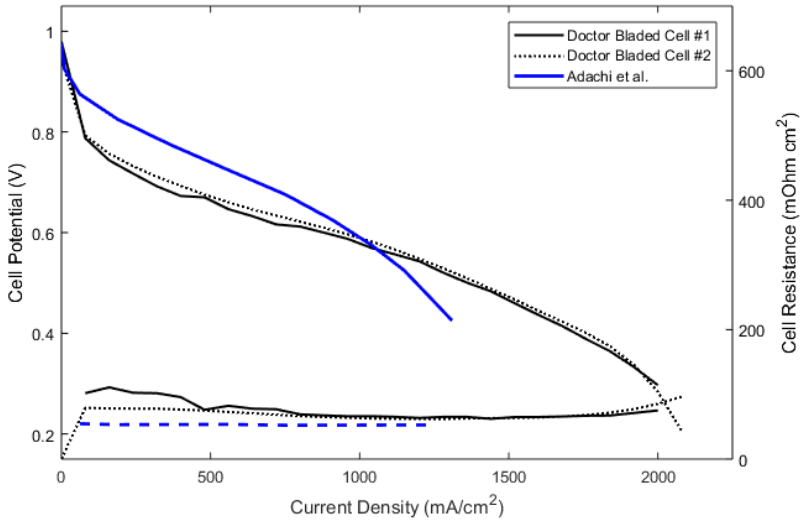

(a) Wet/Dry: 70°C, A: 100% RH, C: 40% RH, 0 kPa(g)

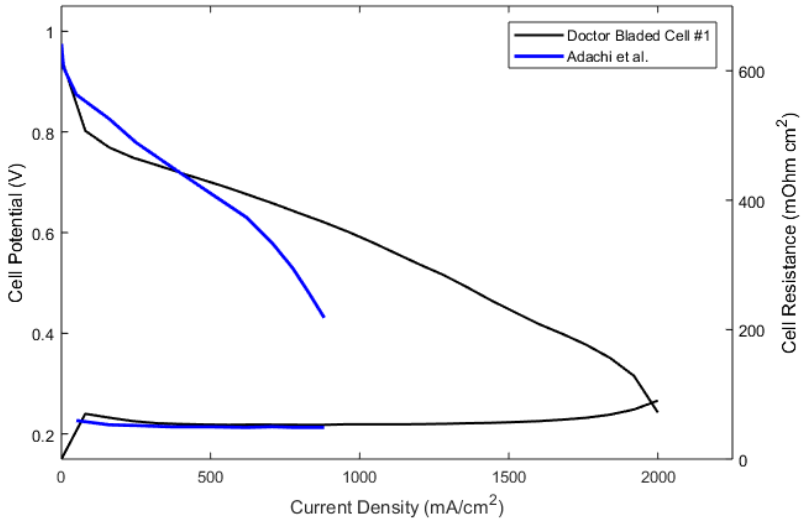

(b) Dry/Wet: 70°C, A: 40% RH, C: 100% RH, 0 kPa(g)

Figure 4.7 – Performance comparison between the doctor-bladed cells and the results reported in Adachi et al. [54] for a similar cell build

The doctor-bladed cells were outperformed by the spray-coated cell used by Adachi et al. in the kinetic and part of the ohmic regions but performed best at higher current densities after the cell used by Adachi et al. cell suffered from early onset mass transport issues. Performance in the kinetic region is correlated with the electrode loading and electrochemical surface area (ECSA), with higher amounts of both contributing to lower activation requirements. Compared to spray-coating, and to a lesser extent inkjet printing, doctor-blading has been speculated to produce a lower catalyst layer porosity and therefore a lower ECSA. For example, the ECSA of the second doctor-bladed cell, extrapolated from Figure 4.6d, was 69.8 m^2/g of catalyst compared to a typical ECSA of $\geq$ 90.0 m^2/g for inkjet printed electrodes. Although Adachi et al. did not report the ECSA of their MEAs, assuming spray-coating is comparable to inkjet printing, this difference would explain the poor performance of the doctor-bladed cells at low current densities.

As the current density increased, the performance of the spray-coated cell non-linearly dropped, mimicking behaviour very much representative of mass transport limitations. Given the supersaturation of one of the gas streams, flooding is likely the cause. A flooded electrode is usually accompanied with a change in the cell resistance as some of the liquid water is either absorbed by the membrane, lowering its protonic resistance [8], or liquid water limits the permeation of gas into the catalyst layer and shifts the reaction further from the membrane-catalyst layer interface, raising the cell resistance [24]. Although not always the case, the lack of change in the cell resistance reported by Adachi et al. may be evidence that the electrodes did not flood and the mass transport losses are instead a result of the GDL being over compressed.

It was also not clarified in the ref. [54] whether wet or dry stoichiometric ratios were used. Wet stoichiometric ratios introduce additional dry gas to offset the dilution caused by humidifying the gas. For the operating conditions imposed in Figure 4.7, wet stoichiometric ratios of 2.0/3.0 (A/C) correspond to dry stoichiometries of 3.0/3.5. The difference from having 50% and 17% more fuel at the anode and cathode would be most apparent at those high current densities, shifting the limiting current density higher.

The polarization curves presented by Adachi et al. [54] showed a distinct difference in performance between (i) wet/dry and (ii) dry/wet operating conditions. The highest attainable current density for case (ii) with the cathode supersaturated was approximately 30% less than for case (i). This is to be expected because the reaction rate of the ORR is more susceptible to reactant starvation.

The doctor-bladed cell #1 behaved differently, exhibiting nearly identical performance irrespective of the inlet humidities. This goes against convention, however,

Table 4.10 – Operating conditions for Adachi et al. [54] literature validation

Condition	Value
Cell Temperature	70°C
Relative Humidity[1]	(i) 40/100% & (ii) 100/40%
Minimum Flow Rates	0.25 slpm
Wet Stoichiometric Ratios[1]	2.0/3.0
Pressure	Ambient
Current Density	0.6/1.0/1.4 A/cm^2
Experimental Duration	3 hours

1: Written as anode/cathode

as will later be discussed, NR211 membranes have excellent water transport properties. In addition, having lowered the relative humidity of the wet gas stream to 100% allowed the cell exposed to both operating conditions to achieve higher current densities before flooding.

The water balance setup was introduced after the cells had been characterized. The first doctor-bladed cell fully replicated the experiment conducted by Adachi et al. [54] and the second cell only replicated case (i). The operating conditions are summarized in Table 4.10. The net water flux was measured as the difference in the amount of water entering and leaving the anode. The water entering the cell was characterized beforehand by directing the gas flow through the bypass loop. Measurements were taken of the gas temperature, relative humidity, and pressure to calculate the water content with equations (2.3), (2.4), and (2.6). The outlet water content was similarly calculated with the fuel cell exhaust stream. The cell was operated at a constant current for 3 hours. Only measurements after the first hour were reported to allow the opportunity for the cell to acclimatize. The net water flux reported as part of this study was the average of the instantaneous water fluxes measured over the remainder of the experiment.

The net water flux reported from measurements performed at the anode are plotted in Figure 4.8 and summarized in Table 4.11. For case (i), the net water flux reported by Adachi et al. exhibited a quadratic relationship with increasing current density. As the current density increased above 0.4 - 0.6 A/cm^2, the EOD contribution to the net water transport grew, becoming the dominate transport mechanism. The baseline contribution to the net water transport as a consequence of the concentration gradient, amounting to 0.018 mol/(cm^2 s), was extrapolated from where the quadratic fit intersected with a current density of zero. From there, EOD and to a lesser extent the shift in the concentration gradient from water production, increased

the net water flux to 0.051 mol/(cm^2 s) at a current density of 1.4 A/cm^2.

The same trend was detected with the doctor-bladed cells and water balance setup however to a much lesser extent. The net water flux still exhibits quadratic behaviour but the value reported at each current density is lower than those reported by Adachi and by greater amounts as the current density increases. The discrepancy between the two data sets ranges from a factor of 1.5 to 2.1.

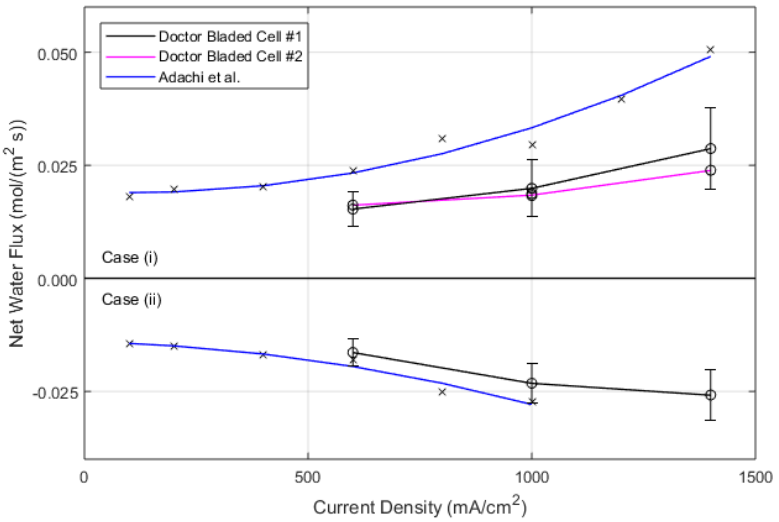

Figure 4.8 – Net water flux across the doctor-bladed CCM compared to results published by Adachi et al. [54]

For case (ii), Adachi again reports a quadratic trend however the fit is less convincing and the behaviour contradicts their previous argument. The concentration gradient imposed by the dry/wet conditions encourages back diffusion towards the anode, noted by the negative net water flux. As current density increases and, as per their previous argument, one expects EOD to become more apparent, however the quadratic fit instead bends in the direction of the anode, suggesting back diffusion is increasing and EOD is non-existent. A reason for this behaviour is not discussed in the article.

The reported values doctor-bladed cell #1 were of a similar magnitude to those reported for case (ii), however the quadratic behaviour is inverted. Extrapolating the fit towards higher current densities forecasts the net flux will approach equilibrium then begin flowing towards the cathode. This is in agreement with Adachi et al.'s argument for case (i). As current density increases, EOD becomes more prevalent gradually offsetting back diffusion from cathode to anode by an increasing amount.

Table 4.11 – Comparison of the net water flux measured by water balance setup to the values reported by Adachi et al. [54] at the same current densities

Current Density	**Adachi et al.** (mol/(m^2 s))	**Doctor Bladed Cell #1** (mol/(m^2 s))	**Doctor Bladed Cell #2** (mol/(m^2 s))
Case (i)			
0.6 A/cm^2	0.024	0.015 ± 24.8%	0.016 ± 23.5%
1.0 A/cm^2	0.030	0.020 ± 31.7%	0.018 ± 33.5%
1.4 A/cm^2	0.051	0.029 ± 35.3%	0.024 ± 37.4%
Case (ii)			
0.6 A/cm^2	-0.018	-0.016 ± 24.8%	-
1.0 A/cm^2	-0.027	-0.023 ± 27.6%	-
1.4 A/cm^2	-	-0.026 ± 31.6%	-

Despite attempts to replicate the same CCM and cell assembly, the performances noted in Figure 4.7 distinctively shows the two fuel cells are different from the cell tested by Adachi et al. [54]. Possible differences in the microstructure of the porous layers would likely influence water transport inside the cell. Furthermore, the higher resistances reported for the doctor-bladed cells may be indicative of a higher PEM resistance which is proportional to the amount of water the membrane has absorbed. Lower absorption levels are typically accompanied with lower water permeability [8]. Provided the differences in cell characterization, exact replication of the Adachi et al.'s results would have been unlikely.

Furthermore, the original publication of the crossover reported by Adachi et al. [54] had error bars representing the standard deviation from an undisclosed number of trials. The largest error bar corresponded to an approximate relative error of $\leq$ 13%. The error bars illustrated in Figure 4.8 for doctor bladed cell #1 are the single measurement overall uncertainty of the setup based on the work of Section 3.1. The error bars for doctor bladed cell #2 were omitted for clarity but were of the same magnitude as those shown for doctor bladed cell #1. These uncertainties are large due to the cumulative systematic uncertainty of the setup sensors. To place this into perspective, crossover measurements taken with a current density of 1.0 A/cm^2 were repeated three times using doctor bladed cell #2, resulting in a standard deviation of 0.002 mol/(cm^2 s) for a precision uncertainty of ±2.2%. Here, the precision uncertainty is taken as two times the standard deviation which is proper convention for capturing a confidence interval of 95%. The bulk of the uncertainty therefore comes from the water balance equipment itself and not the standard deviation. The extent of the systematic uncertainty of setup used by Adachi et al. [54] is not mentioned in the paper, raising questions about the accuracy of their individually measured

net water fluxes. Adachi et al. performed all tests with the a Scribner 850c test station, similar to that used at the ESDLab, however as opposed to measuring the vapour pressure of the gas entering the cell as part of each experiment, previously predicted fluxes of water from calibration measurements conducted independent of the experiment were used. There is no mention of the uncertainty associated with the calibration measurements but from experience with the 850e test station, the inlet vapour pressure can fluctuate on the order of approximately $\pm$ 5.0% between experiments. When using the water balance setup, that uncertainty is minimized by measuring the vapour pressure entering the cell before and after experimentation.

The water balance setup's correct identification of the relationship between back diffusion and EOD with current density while also reproducing net water fluxes within the same order of magnitude as the literature is sufficient to confirm the water balance setup's capacity to accurately measure steady state water crossover.

4.3.1 Transient Behaviour

Water collection provides a time averaged quantitative means for extrapolating the internal crossover of water inside a fuel cell. Measurements are performed on the amount of liquid water ejected from the cell and a mass balance is used to resolve an average crossover relative to the duration of the collection period. Even by performing real time mass measurements of the water condensed from the exhaust streams, minor transient events become obscured by the resolution of the scale, the time taken to condense the gas, or the distance and time needed to transport the water to a scale.

The water balance setup has the same limitations when monitoring the crossover. Measurements are performed downstream of the cell and not at the catalyst-layer interface so the crossover values reported are influenced by capacitative features such as the porous structure of the MEA, the hydration state of the membrane, and the capacity of the flow fields and supporting piping to harbour liquid water. Although instantaneous measurements of the water leaving the cell are reported, by assuming the water entering the cell and the water generated is uniform, the crossover acquires whatever shape the water leaving the cell does. This can be misleading as an ejection of water as a result of some accumulation inside the cell over time will appear as a sudden change in the crossover. Crossover values should only be reported as a time average to smooth out any transient behaviour. However, provided the MEA has acclimatized and the operating conditions are steady, the transient cell response to a sudden change of operating conditions and the time required to return to equilibrium can be studied. This assists the development of transient numerical models being

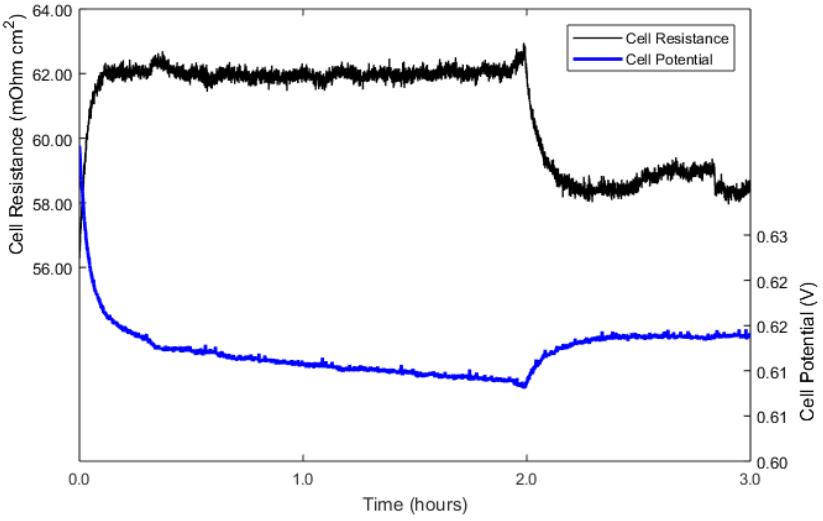

Figure 4.9 – Transient cell behaviour discovered during steady state operation (1.0 A/cm^2, wet/dry)

developed at the ESDLab.

By exclusively monitoring the gas phase, the resolution for measuring minor transient events is much higher than water collection systems. In most cases, close examination of the cell behaviour during net water flux measurements reveal small fluctuations in the cell potential and resistance such as those illustrated in Figure 4.9. The initial drop in cell potential corresponds to the cell acclimatization period as fuel is introduced into the cell and a load is applied. This behaviour was exhibited in every experiment and justifies the one hour period prior to interpreting the water crossover measurements. The sudden 10 mV increase in cell potential at the two hour mark however was unique. The corresponding change in cell resistance suggested the transient event was in some part connected to a change in the water profile inside the cell. Until now, this could only be speculated.

The same event is reflected in the molar flux of water leaving the cell and the pressure downstream of the cell, shown in Figure 4.10. With the water balance setup, it can be confirmed there was a large liquid water ejection event at the two hour mark. The molar flux of water measured by the sensor increased by approximately 8.5% over the course of ten minutes. This is the same behaviour Niroumand et al. [66] encountered which was attributed to two-phase flow. In this instance, the slow decrease in cell potential can be correlated with the accumulation of liquid water in the porous layers of the MEA and the channels of the flow field, throttling the reactant flow to the catalyst layer. The restriction was sufficient enough to noticeably change

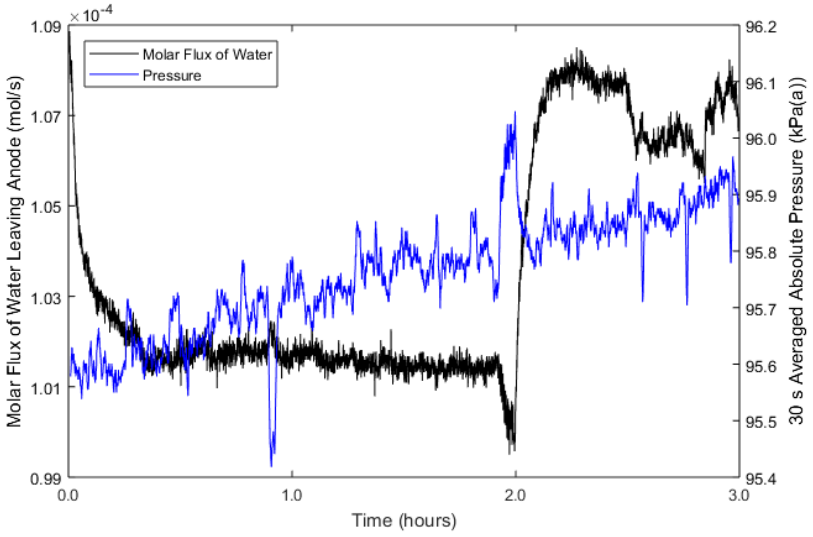

Figure 4.10 – Molar water flux and pressure measured by water balance setup capturing water ejection event (1.0 A/cm^2, wet/dry)

the pressure downstream of the cell. Once a certain threshold was achieved, the liquid water shedded from the MEA, opening the previously blocked pathways for gas transport, resulting in a sudden increase in cell potential.

Justification for the correlation between water transport and cell resistance is not as clear. Typically cell resistance and water content are inversely proportional. This can be seen in Figure 4.6c where the cell resistance decreases as the humidity of the inlet gases increases. The more water introduced into the cell, the more water absorbed by the membrane, and the lower the membrane resistance. In addition, the absorption of water by both the membrane and the porous layers causes the various layers to expand, decreasing the contact resistance at each interface. This understanding is at odds with the behaviour exhibited by the resistance in Figure 4.9. Despite the apparent ejection of liquid water from the cell, the cell resistance decreases. A possible explanation for this behaviour was recently predicted in a numerical modelling publication investigating the role of an MPL on cell performance [24]. It was predicted that water first accumulates inside the catalyst layer at the membrane-catalyst layer interface and from there propagates towards the MPL. This accumulation limits the penetration of the gas into the catalyst layer, shifting the reaction further from the membrane-catalyst layer interface. This increase in the distance for protons to travel would raise the cell resistance, although there was no discussion on quantifying the extent of the change.

This relationship between the cell potential, resistance, and outlet molar flow rate of water was seen throughout the experiments. Figure 4.11 shows a different collection of transient events. The approximate uncertainty of the molar flux of water reported in both Figures 4.10 and 4.11b is 8-9%. This is on the same order of magnitude as the transient events. Similarly, the accuracy of the cell potential measured by the test station is $\pm$ 0.3 mV $\pm$ 0.3% which corresponds to approximately $\pm$ 5 mV when applied to the potentials reported in Figures 4.9 and 4.11a. In both cases, there is not a statistically significant enough change in the molar flux to extrapolate the cumulative amount of water that is ejected with each event. However, it should be noted that the cell potential and molar flux of water are measured independently. That two independent measurements can identify the same transient event confirms the water balance setup capacity to monitor transient behaviour. This is useful for investigating the effect different cell and operating parameters have on the occurrence of two-phase flow within the cell.

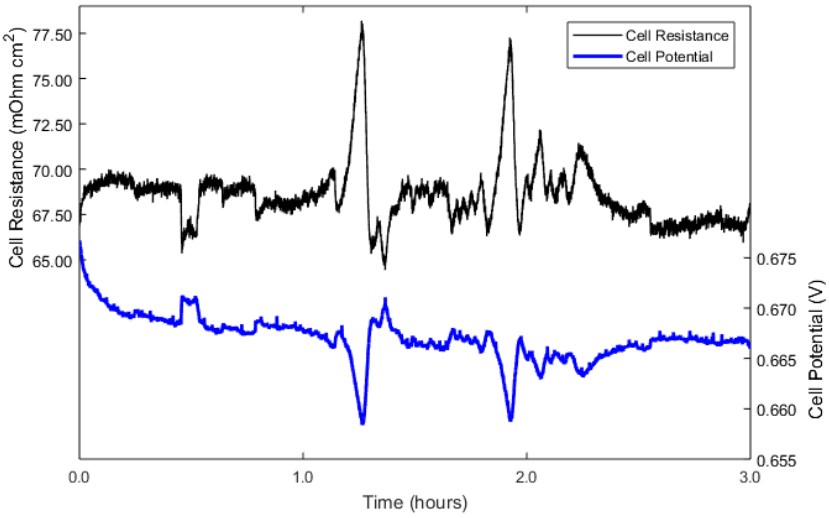

(a)

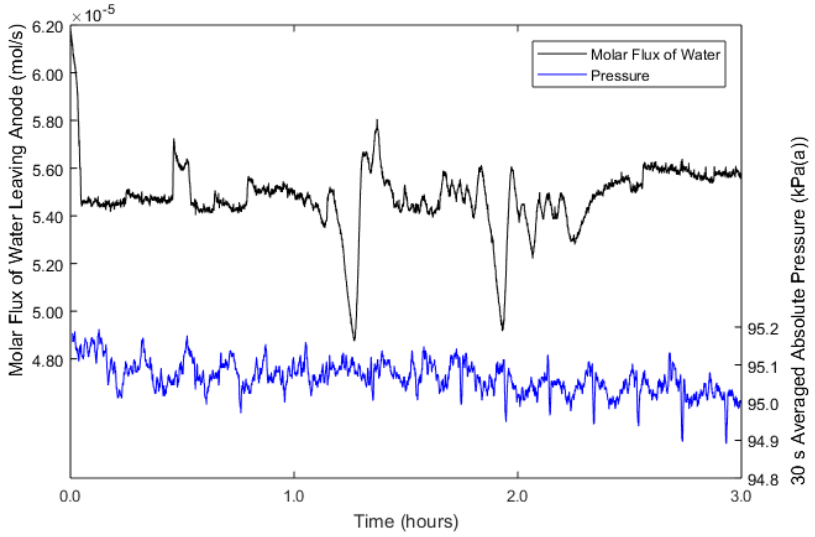

(b)

Figure 4.11 – Transient behaviour reflected in cell potential and resistance measurements (a) and molar flux of water leaving the cell (b) (0.6 A/cm^2, wet/dry)

Chapter 5

MPL Investigations

This chapter will address some of the gap between the works of Kim et al. [31] and Atiyeh et al. [58] on the role of MPLs on water transport inside the cell. Both groups investigated whether the introduction of an MPL in the cathode influenced the net water flux across the membrane. Kim et al., using two MEAs with the same cell construction, found the addition of an MPL to the cathode increased the rate of water transport towards the anode. The lower saturation in the cathode GDL was then attributed to reduced oxygen mass transport resistance and increased membrane water content, both contributing to improved cell performance. Conversely, Atiyeh et al., with a similarly designed experiment, noted the same improved performance but was unable to discern a statistically significant enough change in the net water flux to warrant a conclusive connection between the MPL and water transport. The most notable difference between the two studies was the membrane thickness. Kim et al. used an 18 μm thick Gore membrane whereas Atiyeh et al. used a 50.8 μm thick Nafion N112 membrane. This work was originally conducted under the speculation that the benefits of an MPL are limited by the membrane thickness. Extrinsic transport and electrical phenomena such as diffusion and resistance are known to be dependent on some characteristic length and therefore whatever cell properties an MPL modifies may only be apparent below a certain membrane thickness.

The molar flux of water through the membrane is defined by the ratio of the water activity gradient across the membrane and the combination of the interfacial resistances and the bulk resistance of the membrane [8],

$$\dot{n}_{H2O} \propto \frac{\text{Activity Gradient}}{\text{Resistance}} \tag{5.1}$$

where the bulk resistance of the membrane is found to be inversely proportional to the steady state diffusivity and linearly proportional to the thickness of the membrane,

$$R_B = L/D_{ss} \tag{5.2}$$

Hence the molar flux of water across the membrane is dependent on its thickness with thicker membranes inhibiting crossover. This is in agreement with the experimental work of Adachi et al. [43] where it was shown water permeation across the membrane increased as the membrane thickness decreased. The objective of this work will be to bridge the gap between the two studies and experimentally investigate the effect of the MPL on the net water flux across the membrane for different membrane thicknesses.

The results from ref. [31] are supported by numerical studies [24] however the mechanism behind the increased mass transport is still disputed. The experimental group speculated the smaller capillary radius and hydrophobicity of the MPL lowers its permeability, generating a pressure gradient that encourages water transport towards the anode. Numerical models however propose the lower thermal conductivity of the MPL retains some of the heat generated from the reaction, increasing the vapour pressure at the cathode which improves diffusion across the membrane. It may be possible that these effects are offset by membrane thickness and become less apparent as that thickness increases. By using the same experimental setup to measure the net water flux across membranes of different thickness, with and without an MPL, the relationship between the MPL and membrane thickness may be resolved and further information regarding the transport mechanism may become apparent.

5.1 Method

The experimental setup and methodology used by both Kim et al. [31] and Atiyeh et al. [58] to measure the net water flux across the membrane were quite similar. Both employed their own variant of downstream water collection, passing the exhaust gas stream through a cold trap and weighing the condensed water. Kim et al. only reported results from the anode, justifying their approach by noting the anode experiences lower flow rates than the cathode under the assumption the flow rate influences the net water flux. Atiyeh et al. only reported results from cathode measurements but did not provide a reason for their choice.

A comparison between the experimental parameters used in this work and the two other studies is summarized in Table 5.1. The two publications served as a framework for the parameters used in this work however this was not an attempt to replicate their results. As such, there are some noticeable differences, much of which arise from the difference in equipment used for crossover measurements.

Table 5.1 – Comparison of cell architecture and experimental operating conditions between this work and the work of Kim et al. [31] and Atiyeh et al. [58]

Parameter	**Experiment Value**	**Kim et al.** [31]	**Atiyeh et al.** [58]
MEA	Inkjet Printed	Gore-PRIMEA-18	Ion Power
Surface Area (cm^2)	5	25	100
Membrane Thickness (μm)	25.4/50.8/127	18	50.8
Platinum Loading[1] (mg_{Pt}/cm^2)	0.09/0.16	0.4	0.3
GDL	SGL 29BA/BC	SGL 10BA/BC	SGL 10BA/BB
Flow Field	Single Serpentine	Single Serpentine	Seven Serpentine
Flow Mode	Co - flow	Counter	Counter
Current Density (A/cm^2)	0.75/1.00/1.25	0.4/0.8/1.2	0.3/0.5/0.7
Duration (hours)	2	3	$\approx$ 23
Cathode RH	100%	100%	100/60%
Anode RH	40%	30/70/100%	60/100%
Cell Temperature (°C)	70	70	60
Stoich Ratios[1]	Fixed 0.1 slpm/3	1.5/2	1.4/2,3
Pressure	50 kPa	Ambient	35 kPa

1: Written as anode/cathode

Accurate results with water collection require large volumes of water. Larger cell areas and experimental durations reflect this requirement which is best exaggerated in the study performed by Atiyeh et al. [58] where a 100 cm^2 cell was operated for approximately 23 hours. Measuring the instantaneous crossover using relative humidity, temperature, and pressure sensors allows the surface area of the MEA to scale without sacrificing much accuracy as demonstrated in Figure 3.9d. Therefore 5 cm^2 inkjet printed cells were chosen and operated for 2 hours, with only results from the latter hour reported and the first hour used to acclimatize the cell.

The platinum loading and fabrication method of the CCM is a continuation of the work by Shukla et al. [81] and the ESDLab. Commercially available MEAs, such as those used in ref. [31] and [58], have generous symmetric loadings. Shukla had shown inkjet printed electrodes with loadings as low as 0.025 mg_{Pt}/cm^2 can achieve current densities greater than 1.25 A/cm^2. Reaction kinetics of the ORR at the cathode are also orders of magnitude slower than anode [9], prompting the use of asymmetric loadings where the anode loading is appreciably less than the cathode. The combined loading of the inkjet printed CCMs used in this study is 0.25 mg_{Pt}/cm^2, nearly 70% less platinum than the Gore-PRIMEA-18.

Three different membrane thicknesses were investigated: Nafion NR211, NR212, and N115. All three membranes have the same chemical specifications, most notably an equivalent weight of 1100 g/mol, defined as the number of the grams of polymer per moles of ionic group. The hydrophilic ionic groups are responsible for the absorption and transport of water through the membrane. As the equivalent weight increases, the amount of water absorbed by the membrane decreases [8]. NR211, with a thickness of 25.4 μm, is the thinnest commercially available Nafion membrane with an equivalent weight of 1100 and without requiring reinforcement. NR212 and N115 are the next thicknesses meeting the same requirements.

Table 5.2 – Cell configurations for membrane crossover study

	A) NR211	**B) NR212**	**C) N115**
1	BA/BA	BA/BA	BA/BA
2	BA/BC	BA/BC	BA/BC
3	BC/BC		

Written as anode/cathode

The different cell configurations used in the study are given in Table 5.2. The type of GDL used was Sigracet SGL 29 series [91] with and without an MPL, denoted as BA and BC respectively. The BA GDL is made from carbon fibres cast into a paper with

Table 5.3 – Sigracet SGL29 series specifications [91]

Parameter	Value	
	29BA	**29BC**
GDL Thickness[1]	140 μm	140 μm
MPL Thickness[1]	N/A	60 μm
Open Porosity[1]	84%	66%
Electrical Conductivity	3.5-4 (S/cm)	2.0-2.3 (S/cm)
Thermal Conductivity	0.4-0.5 W/(K m)	0.5 W/(K m)

1: Measured by Fei Wei of the ESDLab using mercury porosimetry

an organic binder, sintered, and then hydrophobized with a 5%wt PTFE solution. The BC GDL is an extension of the BA GDL with a microporous layer comprised of 77%wt carbon black and 23%wt PTFE applied to one side. Notable properties of the different GDLs are summarized in Table 5.3.

The cell configuration is denoted by a letter and a number shown in Table 5.2, indicating the type of membrane and GDL arrangement inside the cell, i.e. A1 refers to NR211 and BA/BA. All cells were assembled with Fuel Cell Technologies 5 cm^2 single channel serpentine flow fields and cell hardware. A rigid 51 μm thick PFA gasket was used for BA GDLs and a rigid 152 μm thick fibreglass reinforced PTFE gasket was used for BC GDLs. ESDLab gasket availability limited thickness selection. Compression was uniformly applied with a torque based system. Despite the difference in gasket thickness, the amount of compression was qualitatively verified with Fujifilm pressure measurement film, as outlined in Section 2.4.3.

All assembled cells underwent the standard characterization outlined in Section 2.4.4, with the standard polarization curves shown in Figure 5.1 and resistance plots in Figure 5.2.

For crossover measurements, the water bath was warmed to a temperature of approximately 80°C, ten degrees above the cell temperature of 70°C. Prior to measuring the crossover, the gas was passed through the bypass loop and monitored until it achieved steady state. The water content was recorded and the gas was redirected into the fuel cell for crossover measurements to begin. Measurements were recorded every 2 seconds for two hours and only for the anode. Results are reported from measurements recorded after the first hour.

The net water flux was measured at three current densities, 0.75, 1.00, 1.25 A/cm^2. These current densities were chosen as a preliminary starting point to bridge the gap between the low current densities studied by Atiyeh et al. [58] and the higher current densities studied by Kim et al. [31]. Back pressure of 50 kPa(g) was applied to both

the anode and the cathode. Maintaining symmetrical pressures across the membrane minimized the transport of water and gas species due to a pressure gradient. The cathode was supplied with fully saturated air and the anode was supplied with hydrogen at a humidity of 40%. This maintains a concentration gradient in the same direction as Kim et al. [31] and Atiyeh et al. [58].

The minimum amount of dry hydrogen required for a 5 cm^2 cell at current densities of 0.75, 1.0, and 1.25 A/cm^2 is 0.026, 0.035, and 0.044 slpm respectively. The difference between the flow rates was not considered significant enough to warrant implementing stoichiometric flow rates. Instead a fixed flow rate of 0.1 slpm, which corresponds to dry stoichiometric ratios of 3.8, 2.9, and 2.3 for the different current densities, was chosen for the anode. This also happens to be the minimum anode flow rate typically prescribed when operating 5 cm^2 cells to prevent reactant starvation. The cathode was supplied air at a wet stoichiometric ratio of 3 with a minimum flow rate of 0.25 slpm. This corresponds to a flow rate of 0.25, 0.31, and 0.38 slpm for current densities of 0.75, 1.0, 1.25 A/cm^2 respectively.

5.2 Results and Discussion

5.2.1 Standard Performance Comparisons

The standard polarization curves for every cell configuration at each inlet humidity are presented in Figure 5.1. The general categorical order for cell performance has thick membranes without MPLs performing the poorest and thin membranes with a single MPL on the cathode performing the strongest. Considering the curves by its three characteristic regions provides insight into how the MPL may influence the cell performance.

At low current densities, the presence of the MPL had little to no effect on the activation losses of the cell. All curves exhibit the same initial asymptotic behaviour and transition into the linear ohmic region at a current density of approximately 125 mA/cm^2. Yau et al. [42] reached the same conclusion with their own MPL investigation noting feed humidification and the addition of an MPL had no effect on reaction kinetics below 100 mA/cm^2. The average open circuit voltage was 0.94 $\pm$ 0.04 V. One of the advantages of the inkjet printing process is its ability to produce repeatable electrodes [81]. This is then expected as activation losses predominately derive from differences in the loading, catalyst, and microstructure of the catalyst layer, which are the same for each CCM. All the CCMs were inkjet printed with the same 40% platinum supported on KetjenBlack supplied by HyPlat for a final loading

of 0.09/0.16 mg_{Pt}/cm^2 for the anode and cathode respectively.

To further understand the cell behaviour in the the ohmic region, Figure 5.2 plots the cell resistance measured during each polarization curve using current interrupt. The cell resistance is a measure of protonic resistance of the PEM, contact resistance between each layer, and electronic resistance of the catalyst layers and GDLs [87]. Changes in the cell resistance as the current is scanned arise largely from changes in membrane hydration. The non-linearity seen throughout the curves plotted in Figure 5.2 is thought to be an example of this. The momentary low resistance reported for current densities below 120 mA/cm^2 is not reflective of the cell but rather an artifact of the current interrupt measurement process where sufficient current must be drawn from the cell before any values can be reported.

The resistance curves for BA/BA and BA/BC cell builds are arranged into three distinct groups depending on the thickness of the membrane. Not surprisingly, increasing the membrane thickness increased the overall cell resistance. The difference in the average cell resistance correlates with the increase in the slope of polarization curves reported in Figure 5.1 with N115 having the steepest slope and therefore the lowest limiting current density. The cell resistance of the BC/BC cell does not follow any of the trends established by the other cell configurations. Whether this is due to the addition of a second MPL or some other reason is explored later.

According to the manufacturer's specifications [91], the addition of an MPL to BA GDLs lowers the electrical conductivity of the entire layer by upwards of 50%. However, the finer porous structure of the MPL has also been speculated to lower the contact resistance between the porous diffusion media and the catalyst layer [5–7]. To determine the net effect of adding an MPL, Figure 5.3 was used to extrapolate non-PEM related resistances.

The cell resistance reported for the BA/BA and BA/BC cell builds at a current density of 120 mA/cm^2 are plotted relative to their membrane thickness. Each data set represents the same cell build at a prescribed humidity. The BC/BC cell was not included in this analysis as only a single cell of that type was assembled. A low current density was chosen to remove any effects the presence of an MPL has on membrane hydration, providing the clearest picture on how the electronic cell resistance might change with and without an MPL. It is at low current densities that the hydration of the membrane is predominately influenced by the relative humidity of the gas entering the cell and the difference in the membrane water content between BA/BA and BA/BC cells should be the smallest.

The slope of the linear fit correlates to the membrane conductivity and the intercept corresponds to the non-PEM related resistances. The linear relationship demon-

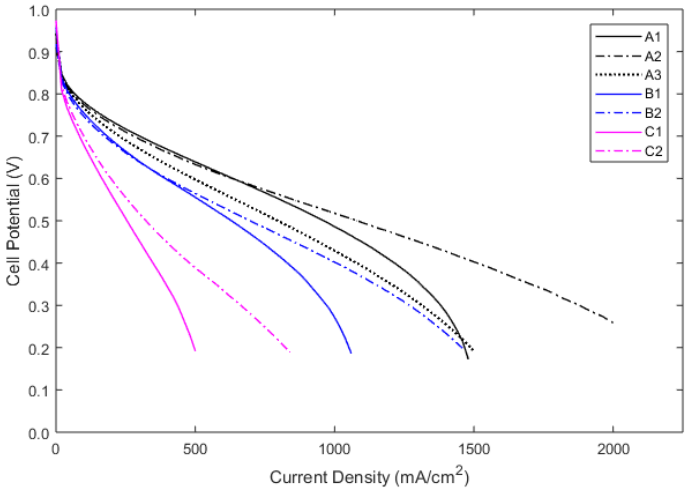

(a) 50% Inlet Humidity

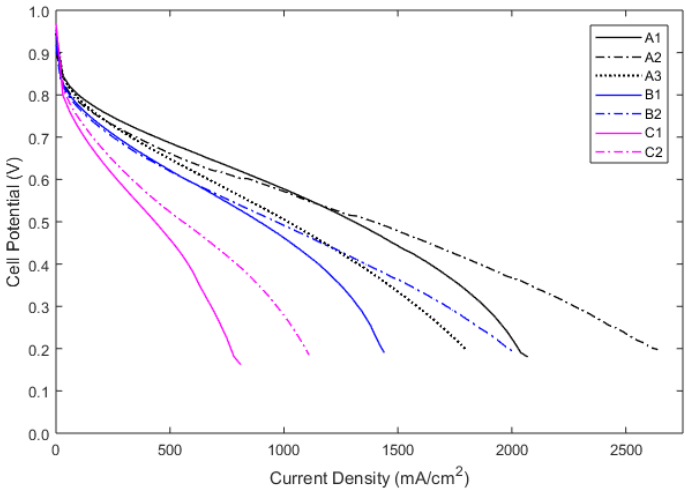

(b) 70% Inlet Humidity

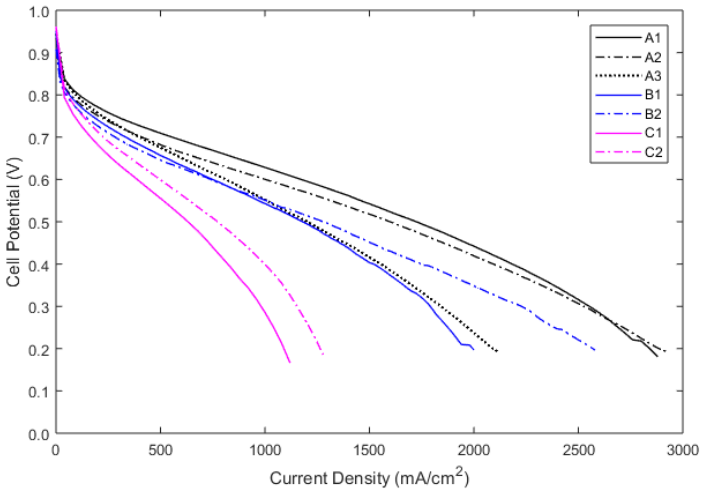

(c) 90% Inlet Humidity

Figure 5.1 – Polarization curves for different GDL arrangements (80°C, 50 kPa(g))

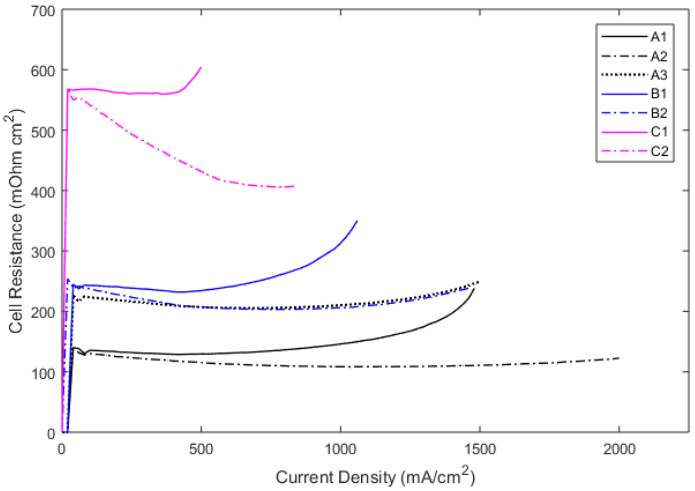

(a) 50% Inlet Humidity

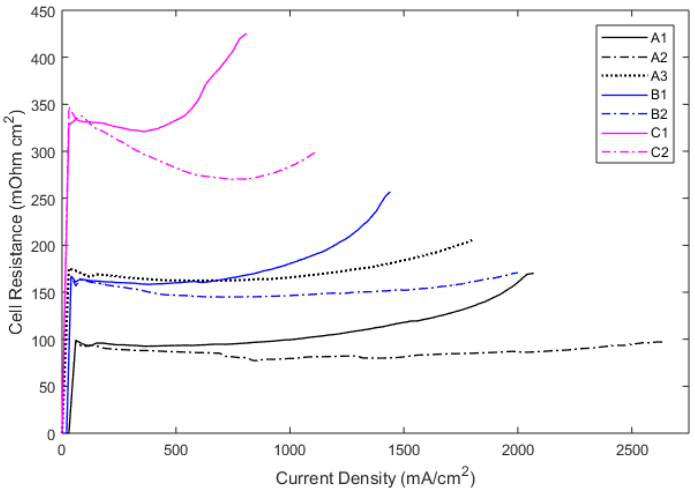

(b) 70% Inlet Humidity

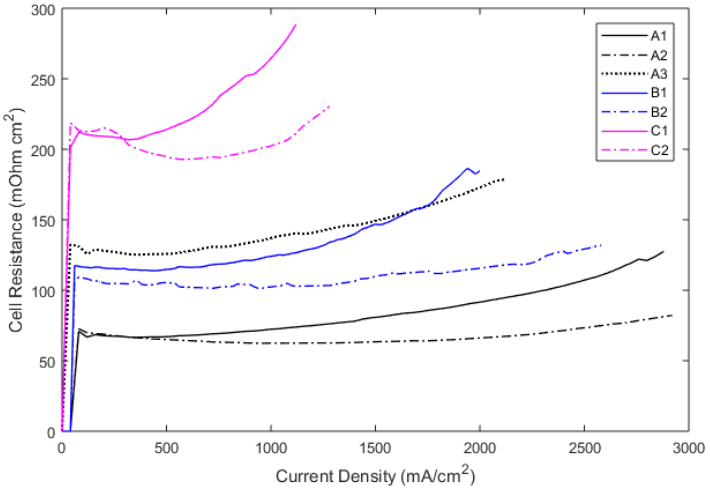

(c) 90% Inlet Humidity

Figure 5.2 – Cell resistance curves for different GDL arrangements (80°C, 50 kPa(g))

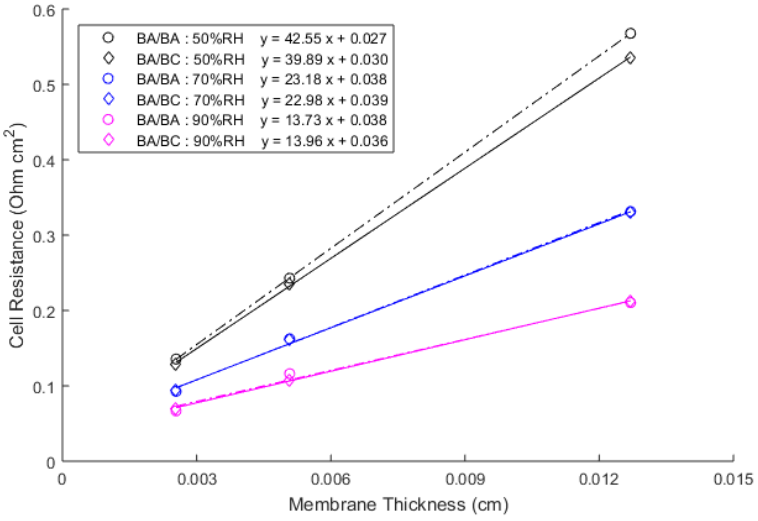

Figure 5.3 – Cell resistance dependency on membrane thickness at 120 mA/cm^2

strates the resistance of the membrane at a given moisture level is directly proportional to the membrane thickness. For each given humidity, increasing the membrane thickness by 5 times corresponded to an increase in the PEM-exclusive resistance by an average factor of 5.09.

Average slopes of 41.22, 23.08, and 13.85 Ohm·cm for inlet humidities of 50%, 70%, and 90% respectively correspond to membrane conductivities of approximately 0.02, 0.04, and 0.07 S/cm. An NR211 Nafion membrane fully saturated with liquid water at a temperature of 80°C has a water content, λ, of approximately 20 and a membrane conductivity of 0.15 S/cm [92]. Despite sharing the same activity, Nafion membranes exposed to saturated vapour exhibit a lower water content than those saturated with liquid water [8]. This phenomenon is known as Schröder's paradox. For a Nafion membrane saturated with water vapour, the water content drops to about $\lambda = 14$. Several studies reviewed by Kusoglu et al. [8] reported membrane conductivities ranging from 0.048 to 0.115 S/cm for the same water content but at temperatures of 25-30°C. Although membrane conductivity further increases with temperature for a given hydration state, the wide range of values reviewed by Kusoglu et al. [8] suggests, given adequate time, exposing a Nafion membrane to inlet gases at 90% humidity will nearly saturate it. Reducing the inlet humidity to 70% and 50% then lowers the water content to approximately 10 and 5 respectively [8]. The close agreement between the conductivities and water contents extrapolated from Figure 5.3 and those from previously published results are evidence supporting the accuracy of the linear fits.

The intercept of each linear fit with the vertical axis is the non-PEM related resistance, summarized for the different cell builds in Table 5.4. These encompass the cumulative electronic resistance of each component and the cumulative contact resistance between each layer. They derive from material selection and cell assembly. At all three humidities, the difference in the non-PEM related resistances between BA/BA and BA/BC MEAs is negligible considering the overall cell resistance. Extrapolating non-PEM related resistances from the total cell resistance determined that in this case, the addition of an MPL had no net effect on a cell's overall electrical resistance. Therefore, the $\geq$50 mOhm·cm^2 resistance measured for the BC/BC cell build is not the consequence of adding a second MPL. The substantially higher resistance is likely from insufficient MEA compression.

The pressure applied to an MEA was qualitatively checked. Differences in applied pressure were noted by the visual strength of the colour imprinted on the pressure film. The narrow range of available gasket thicknesses offered poor control over the repeatable distribution and amount of pressure applied to the MEA. As such, it is probable that when assembling the BC/BC fuel cell, the amount of applied pressure was insufficient resulting in high contact resistances and poorer performance.

The non-PEM related resistances reported for the different cell builds at each humidity were measured without disassembling the cells. Therefore, by assuming the contact resistances did not change, the excellent agreement between the values reported at 70% and 90% humidity (and to a lesser extent 50%) indicate the non-PEM related resistance is independent of the humidity. The portion of cell resistance reported in Figure 5.2 that is over and above the values noted in Table 5.4 result from changes to the membrane water content and/or, in light of a recent publication [24], a shift in the reaction front in the through plane direction of the catalyst layer.

It has been known for some time that the addition of an MPL improves a cell's performance at high current densities; conditions which are notorious for the sudden loss of performance attributed to mass transport limitations. The increase in the limiting current density with the introduction of an MPL seen in this study was anticipated and the results add to an extensive body of work demonstrating this. For most cases, adding the MPL shifted the limiting current density higher, with the

Table 5.4 – Non-PEM related resistances for different cell builds

	50% RH	**70% RH**	**90% RH**
BA/BA (Ohm·cm^2)	0.027	0.038	0.038
BA/BC (Ohm·cm^2)	0.030	0.039	0.036

change, relative to the cells' overall performance, greatest at lower humidities. The one exception was the NR211 membranes at 90% humidity. The performance of the BA/BA and BA/BC cells were almost identical. Extrapolating their performance suggests the BA/BA cell may have begun to experience mass transport limitations before the BA/BC cell however this cannot be confirmed due to the 0.2 V turnaround potential.

Although the pressure film concluded the compression applied to both types of GDLs was equivalent, considering the GDL and gasket thicknesses, intuition suggests the compression for the thinner gasket should be higher. Assuming the bulk GDL yields to compression before the MPL and that the gaskets are incompressible, the decrease in porosity after cell assembly can be found using,

$$\varepsilon_a = 1 - \frac{t_b}{t_g}\left(1 - \varepsilon_b\right) \tag{5.3}$$

where ε_a is the open porosity of the GDL after compression, t_b is the thickness of the GDL before compression given as 140 μm, t_g is the thickness of the gasket less the thickness of the MPL (if one is present), and ε_b is the porosity of the GDL before compression given as 84%. For the 29BC GDL compressed with the 152 μm PTFE gasket, the open porosity collapses to 75% and for the 29BA GDL with the 51 μm PFA gasket, the open porosity drops to 55%. While the BA/BA cell may experience lower gas permeation through the cathode GDL, the addition of an MPL, with a manufacturer reported open porosity of approximately 40% [91], makes comparing the transport properties of the two complete porous layers difficult. The pressure differential across the cathode for the BA/BA cell build measured with nitrogen at 1.0 slpm and room temperature is 23.84$\pm$0.81 kPa whereas the pressure differential measured with the same conditions for the BA/BC cell build is 24.01$\pm$0.81 kPa suggesting neither GDL impregnated the flow channels. For now it is assumed the effect of the difference in porosity between the two cell assemblies on gas permeation through the porous layers is negligible. The near-identical performance of the NR211 BA/BA and BA/BC cells at 90% RH suggests the difference in porosity does not affect reactant transport.

Referring back Figure 5.2, with the application of an electrical load, the cell resistance for cells without an MPL adopted an increasing quasi-quadratic profile relative to the current density. Similar behaviour was noted in the cells with an MPL however it occurred at a higher current density and to a far lesser extent. Membrane conductivity has been shown to be directly proportional to the amount of absorbed water [8]. An increase in cell resistance may then be indicative of membrane drying.

Interestingly, at the same current densities, Figure 5.1 shows cells without an MPL exhibit the distinct asymptotic performance that approaches a limiting current density which has been considered characteristic of mass transport losses and flooding. Flow rates were the same throughout Figure 5.1 for all cell configurations. Therefore the earlier onset of an asymptotic drop in cell potential seen with cells assembled without an MPL is not the result of insufficient dry reactant entering the cell but may rather be an inability for that dry reactant to reach a reaction site.

Both behaviours suggest the cell is simultaneously flooding and drying out. When operating at high current densities, the EOD from anode to cathode and localized increase in temperature at the electrodes due to the reaction lowers the vapour pressure of the anode electrode and may be subsequently drying the membrane at the anode CL-membrane interface. Conversely, operating at high current densities increases the likelihood of flooding at the cathode. A large amount of water is produced and EOD introduces even more water from the anode. If flooding were then to occur, it would first manifest at the cathode CL-membrane interface and propagate towards the porous media, drawing the reaction front with it. The farther the reaction is from the membrane, the further the protons have to travel through the ionomer phase of the catalyst layer, possibly raising the cell resistance measured with current interrupt.

For the MPL to minimize this behaviour, as seen throughout Figures 5.1 and 5.2, the MPL would have to reduce drying at the anode and flooding at the cathode. The MPL may be acting as a transport barrier, inhibiting water generated as product of the reaction and transported via EOD from accumulating in the cathode GDL and leaving the cell through the cathode. In doing so, the pathways needed for oxygen transport to the catalyst later remain free. A larger breakthrough pressure needed for water to pass through the MPL would encourage water retained in the cathode catalyst layer to pass through the membrane and leave via the anode instead, thereby reducing the likelihood of the membrane at the anode from drying out. Insight into this shift in the crossover and the hydration state of the gases leaving each side of the cell should be identifiable with the water balance setup.

In all, the cell with only an MPL on the cathode fared the best. This is in agreement with Kim et al. [31] who found the order from poorest to strongest performance to be cells without MPLs, cells with an MPL on both sides, and finally cells with only an MPL on the cathode. This work differs in that cells without an MPL outperformed those with two MPLs, however this may be a result of the compression issues noted earlier. Numerical results from Zhou et al. [24] predicted the MPL improves performance by in large because of its lower thermal conductivity that retains extra heat from the reaction, raising the temperature of the electrode. The group concluded

this reduces cathode flooding. Only cells with two MPLs were investigated and the conclusions do not provide any insight into the ideal MPL arrangement for optimal cell performance.

5.2.2 Low Flow Rate Crossover

The net crossover flux for each cell configuration measured at the conditions outlined in Table 5.1 is provided in Figure 5.4. The crossover has been normalized to the amount of water produced by the reaction. The negative sign indicates water is travelling opposite the direction of the protons and towards the anode. Each data point is comprised of the average of a two second sampling rate recorded over an hour for a single given cell build. Prior to recording any measurements, the cell was operated for a single hour to acclimatize the MEA to the operating conditions.

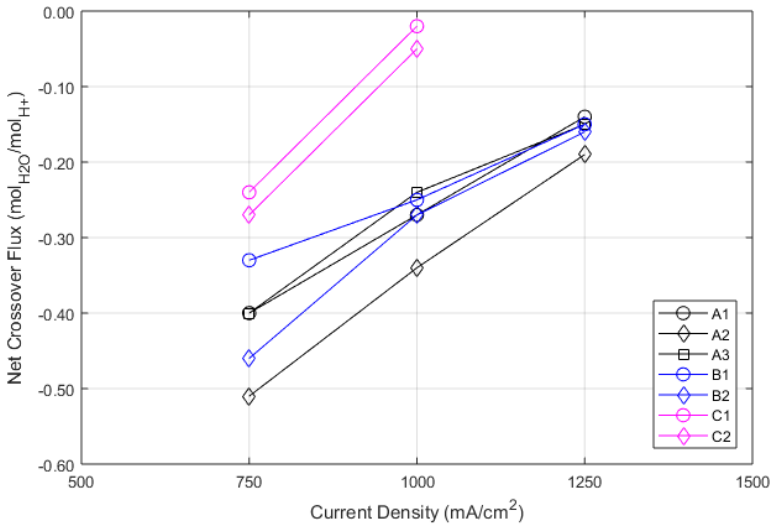

Figure 5.4 – Net crossover flux for different cell configurations at an anode flow rate of 0.1 slpm. Negative indicated transport from cathode to anode. (70°C, A: 40% RH, C: 100% RH, 50 kPa(g))

The overall relative uncertainty for each data point ranged from approximately ±17% to ±32% with the largest errors attributed to the low absolute magnitude crossovers measured at 1.25 A/cm^2. Error bars of those scale were omitted from Figure 5.4 to avoid complicating the plot. As has been previously explored, the majority of a measurement's overall uncertainty comes from the systematic uncertainty of the equipment. Therefore direct measurement is difficult however, because these biases on average apply equally to each reported value, comparisons between identifiable

trends is possible. As an aside, note repeatability conducted in Section 4.3 amounted to a precision uncertainty of ± 2.2%.

As anticipated, the strong concentration gradient introduced by saturating the cathode and drying the anode encouraged the net flux of water to travel towards the anode. Furthermore, the magnitude of the crossover decreased with increasing current density, once again illustrating the effect of current dependent EOD driven water transport.

The magnitude of the normalized net crossover flux ranges from -0.51 mol_{H2O}/mol_{H^+} for an NR211 membrane cell with a single MPL to -0.02 mol_{H2O}/mol_{H^+} for an N115 membrane cell without any MPLs. Crossover values measured by Kim et al. [31] for 18 μm thick GORE membranes tested under similar conditions ranged from approximately -0.39 to 0.05 mol_{H2O}/mol_{H^+}. In ref. [31], cells with a single MPL on the cathode exhibited the largest average crossover towards the anode, followed by cells with two MPLs, and lastly those without any. Crossover values reported by Atiyeh et al. [58] for 50.8 μm thick Nafion membranes exposed to a concentration gradient in the direction of the anode ranged from -0.11 to 0.04 mol_{H2O}/mol_{H^+}. In contrast to the results of this work and those of Kim et al. [31] and Adachi et al. [54], Atiyeh et al. reports the largest crossover towards the anode was from a cell with a single MPL on the anode, whereas adding an MPL to the cathode, reversed the direction of the crossover. This is despite the concentration gradient favouring crossover towards the anode. A positive crossover would be anticipated at high current densities but Atiyeh et al. reported a positive crossover at 0.3 A/cm^2.

Figure 5.4 shows the net crossover for all cell configurations is characterized by a linear trend. However, the net crossover for NR211 and NR212 membranes converges to an average flux of -0.16 mol_{H2O}/mol_{H^+}. This in situ convergence of water crossover across membranes of different thickness has not been seen in other works. Although there is an inclination that NR211 membranes experienced slightly higher crossover and that an MPL further contributes, closer inspection of the vapour pressure downstream of both the anode and cathode for NR211 and NR212 MEAs indicated the gas leaving both sides of the cell were either fully or supersaturated. The vapour pressure remained constant despite changes to the applied current density. This gave rise to the linear behaviour as the downstream dry flow rate is linearly dependent on the current.

Despite the concentration gradient induced by the offset inlet humidities, the product water from the reaction is more than sufficient to saturate both the anode and cathode streams provided enough water can transit the membrane. Recalling that water transport inside a fuel cell is predominately a combination of EOD and

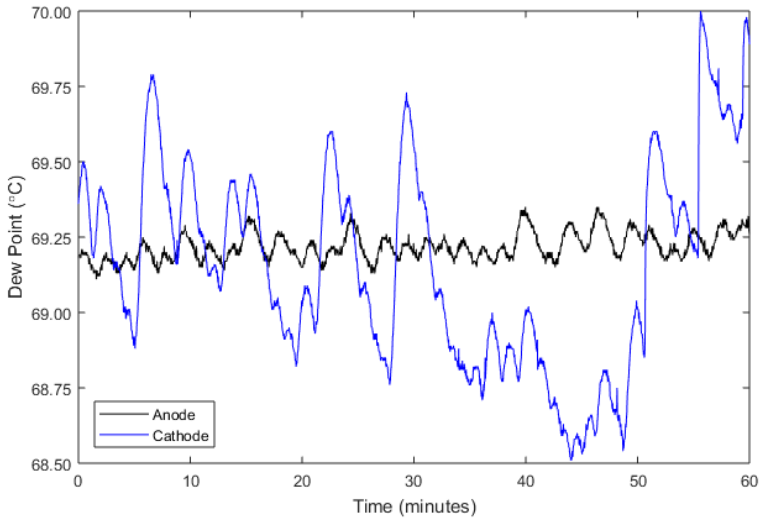

Figure 5.5 – Downstream anode and cathode dew points exhibiting saturation variability for an NR211 BA/BC cell with an anode flow rate of 0.1 slpm (70°C, A: 40% RH, C: 100% RH, 50 kPa(g), 1.0 A/cm^2)

back diffusion, once there is saturated vapour or liquid water present on both sides of the membrane, only back diffusion needed to maintain equilibrium under the steady flux of EOD would occur. Additional water generated on the cathode would then supersaturate the gas stream and leave as two-phase flow. This behaviour, seen in Figure 5.5, was interpreted as the large fluctuations in the cathode dew point measured downstream of the cell, especially in contrast to the more steady saturation of the anode.

Water permeation across a membrane should be dependent on the membrane thickness (relation (5.1) & equation (5.2)). The results from Figure 5.4 imply the water crossover across NR211 and NR212 membranes is the same despite a change in thickness by a factor of 2. By only recording measurements downstream of the cell, the water profile of the gas along the flow field channel cannot be determined. Water transport across NR211 membranes may indeed be faster than NR212 however in the event the flow rate is too low or the channel length is too long, both gas streams for NR211 and NR212 MEAs would have sufficient time to saturate prior to leaving the cell. This gave the illusion both membranes had the same transport properties and artificially indicated the MPLs effect of water transport was insignificant. This development prompted an addendum to the experiment which is discussed in the following section.

This discovery would not have been apparent with the water collection techniques

used in [31] and [58]. The saturation state of the downstream exhaust streams are not measured directly and while it can be inferred at the conclusion of their experiment based on the duration and cumulative amount of water collected, neither group reported any values. Ref. [58] provides a review of Murahashi et al. [50], who had demonstrated net crossover flux varies along the channel based on changes to the concentration gradient, however it was not reflected in their work. Adachi et al. [54] identifies that the downstream anode relative humidity will differ from the inlet humidity however again, no values were reported. The close agreement between the magnitudes reported by Kim et al. [31] and this work suggest they may have also been experiencing similar saturation concerns. Nonetheless, without investigating different membrane thicknesses, the results would not have had much significance.

Downstream vapour pressure measurements for N115 MEAs indicated the gas streams did not saturate. Therefore, N115 MEAs did not follow the same convergence demonstrated by the other membranes, but rather indicated a significantly smaller crossover. This matches expectations. Increasing the membrane thickness increases the membrane's inherit resistance to water transport. Neither N115 cell configuration was able to maintain a load at 1.25 A/cm^2. Only results for 0.75 and 1.0 A/cm^2 were reported. At both current densities, adding an MPL increased the crossover by 0.03 $\text{mol}_{H2O}/\text{mol}_{H^+}$ towards the anode. This is in agreement with the observations discussed in Section 5.2.1. An N115 membrane is 2.5 times thicker than the membrane studied by Atiyeh et al. [58] however with only two data points to compare and a marginal increase, the effect of the MPL on this thickness of membrane requires further investigation to confirm.

Having attributed the poor performance to compression issues, the addition of a second MPL appears to counteract the positive attributes of the first. Kim et al. [31] concluded the increase in water transport seen in their results after the addition of a single MPL to the cathode was due to a the MPL creating a hydraulic gradient which pushes water across the membrane towards the anode. They extended their argument to suggest a second MPL also generates a hydraulic gradient but in the opposite direction, lowering the pressure difference between the two electrodes and subsequently lowering water transport. Although the low limiting current density and crossover measured for BC/BC cells in this work are symptoms of this phenomena, the high resistance concerns should be addressed before drawing further conclusions.

5.2.3 High Flow Rate Crossover

Due to the saturation of the gas streams leaving NR211 and NR212 MEAs, only the crossovers reported for N115 identifies a difference between cells assembled with and without an MPL. Insight from Section 5.2.1 suggested an MPL should also influence water transport across the thinner membranes however according to the low flow rate measurements, there was an inconclusive change similar to what was reported by Atiyeh et al. [58]. Avoiding the saturation of the exit stream requires either decreasing the length of the flow field channel or increasing the flow rate of the gas. Implementing the latter raises the velocity of the gas and decreases the residence time inside the fuel cell. Additional crossover experiments were performed on all NR211 cell configurations with a higher fixed anode flow rate of 0.4 slpm in an attempt to dilute the downstream vapour pressure. This corresponds to dry stoichiometric ratios of 23.0, 15.3, 11.5, and 9.2 for a 5 cm^2 cell and current densities of 0.50, 0.75, 1.00, and 1.25 mA/cm^2 respectively. The addendum to the crossover experiments performed in Section 5.2.2 is summarized in Table 5.5

Table 5.5 – Revised experimental operating conditions for investigating different GDL arrangements

Parameter	**Experiment Value**
MEA	Inkjet Printed
Surface Area (cm^2)	5
Membrane Thickness (μm)	25.4 (NR211)
Platinum Loading[1] (mg_{Pt}/cm^2)	0.09/0.16
GDL	SGL 29BA & BC
Flow Field	Single Serpentine
Flow Mode	Co - flow
Current Density (A/cm^2)	0.50/0.75/1.00/1.25
Duration (hours)	2
Cathode RH	100%
Anode RH	40%
Cell Temperature (°C)	70
Stoich Ratios[1]	Fixed 0.4 slpm/3
Pressure	50 kPa

1: Written as anode/cathode

The experimental approach remained the same; the cell was operated at steady state for one hour prior to recording measurements for an additional hour at a sampling rate of a data point every two seconds. Upstream measurements utilizing the bypass lines determined the water content of the gas entering the cell which was assumed unchanged for the duration of the experiment. Downstream measurements

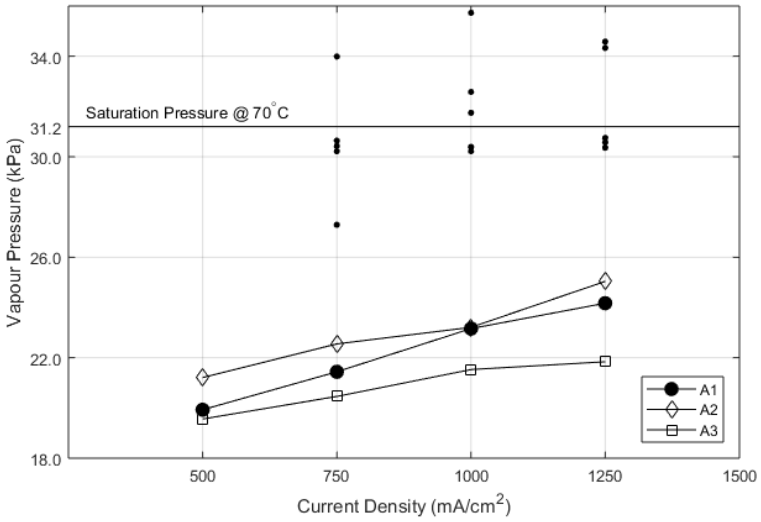

Figure 5.6 – Downstream vapour pressure for the different NR211 cell configurations at an anode flow rate of 0.4 slpm (70°C, A: 40% RH, C: 100% RH, 50 kPa(g))

of the temperature, relative humidity, and pressure provided a real time view of the water leaving the cell.

The change in the downstream vapour pressure was immediately realized. As plotted in Figure 5.6, the physical effect of increasing the anode flow rate by a factor of four can be seen by the decrease in the average vapour pressure measured downstream of the cell. The black data points scattered around the saturation pressure at 70°C are a sample of the downstream vapour pressures measured for NR211 and NR212 MEAs at the lower anode flow rate of 0.1 slpm from Section 5.2.2. Any vapour pressure exceeding 30 kPa was considered to be either saturated or supersaturated to accommodate any differences between the reported cell temperature and the true maximum temperature achieved by the gas. Raising the flow rate lowered the vapour pressure well below 30 kPa and provided enough resolution to distinguish between the different cell configurations.

The differences in the downstream vapour pressure were mirrored in the reported net crossover fluxes. Figure 5.7 illustrates the net crossover flux at the prescribed current densities. Contrary to Figure 5.4, there is a clear distinction between the different MPL configurations. Independent of the current density, the order for the largest to smallest net crossover flux is MEAs with an MPL on the cathode, MEAs with no MPLs, and lastly those with two MPLs. This order is consistent with the performance ranking discussed in Section 5.2.1.

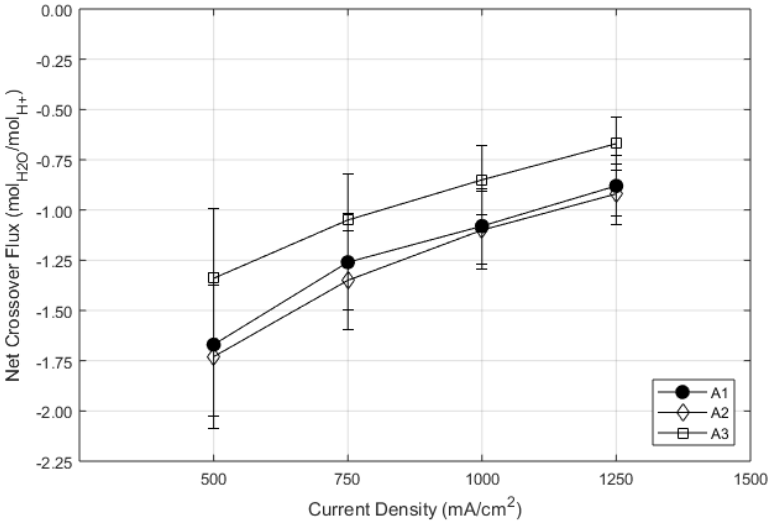

Figure 5.7 – Net crossover flux for NR211 cell configurations at an anode flow rate of 0.4 slpm (70°C, A: 40% RH, C: 100% RH, 50 kPa(g))

By increasing the anode flow rate, convective drying of the anode reinstated the concentration driven back diffusion, thereby more than doubling the average net crossover fluxes compared to the lower flow rate measurements from Section 5.2.2. Janssen et al. [49] reached the same conclusion. Lowering the average vapour pressure along the anode channel to avoid saturation allows substantially more water to crossover. This increase in crossover from raising the anode flow rate demonstrates ultra-thin membranes are not a significant barrier to water transport and the full extent of their ability to manage water levels on the cathode can be realized by diluting the anode stream. Utilizing the anode as a pathway for ejecting water from the cathode allows the cell to operate at even higher current densities where previously, flooding of the cathode electrode was likely.

Figure 5.8 shows the polarization curves for the different NR211 cell configurations at the same conditions (40% anode RH & 100% cathode RH) used for measuring the cell crossover. Minimum flow rates of 0.2 and 0.4 slpm combined with wet stoichiometric ratios of 2 and 6 were used for the anode and cathode respectively. Again, the single MPL arrangement has the strongest performance raising the limiting current density by approximately 30% and the double MPL arrangement had the poorest performance.

Direct comparison to the performances noted in Figure 5.1 are difficult because of the asymmetrical inlet humidities, different cell temperature, and flow rates. Despite having a lower cumulative amount of water entering the cell and a lower electrode

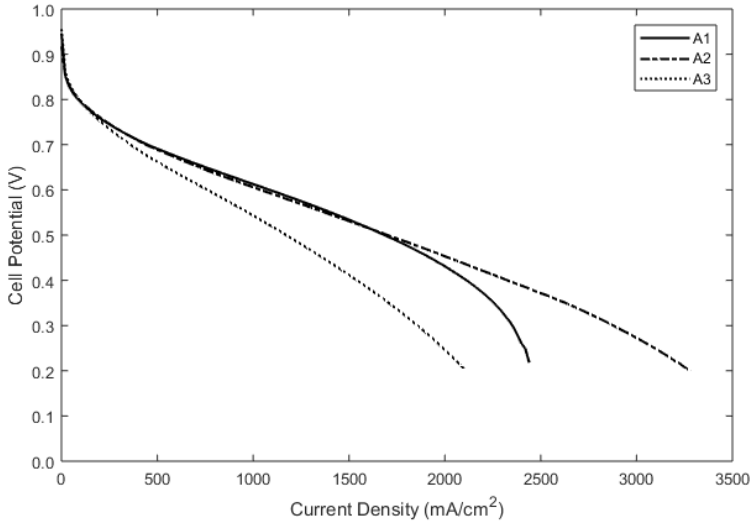

Figure 5.8 – Polarization curves for NR211 cell configurations at crossover experiment operating conditions (70°C, A: 40% RH, C: 100% RH, 50 kPa(g))

temperature, the profile of the polarization curves and the cell resistances reported in Figure 5.9 are best described by the results captured for inlet humidities of 70% RH and a cell temperature of 80°C shared in Section 5.2.1. Although the profile appeared the same, the polarization curves generated with asymmetrical inlet humidities experienced a 17-24% increase in the limiting current density. For the configuration with a single MPL added to the cathode, a limiting current of 3280 mA/cm^2 at 0.2 V is the highest measured in the ESDLab.

For current densities less than 1750 mA/cm^2 there is no defined difference between the performance of the BA/BA and BA/BC cell builds. The addition of an MPL appears to only influence the performance of the cell at current densities that approach and define the mass transport limited region specific to a particular cell. The same conclusion cannot be said for the BC/BC cell which again exhibited notably higher cell resistances that remained from its inconsistent cell assembly.

The net crossover fluxes noted in Figure 5.7 show BA/BA and BA/BC MEAs experience almost the same magnitude of flux towards the anode. Meanwhile the limiting current for the cell without any MPLs was 840 mA/cm^2 lower than the BA/BC cell. To understand this substantial difference in performance, additional crossover measurements were performed at a current density of 1750 mA/cm^2, where the performance of the two cell builds begin to diverge, and 2400 mA/cm^2, just below the BA/BA cell's limiting current density. The results are plotted in Figure 5.10.

Note, as opposed to the previously reported crossover values, Figure 5.10 was

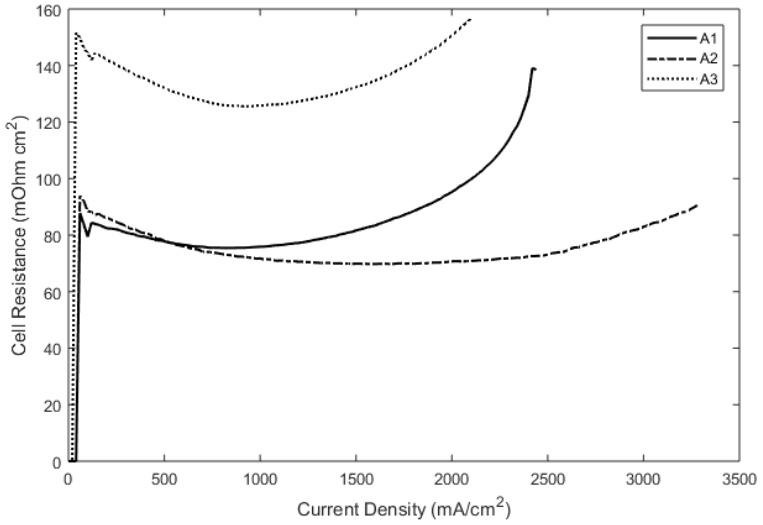

Figure 5.9 – Cell resistance for NR211 cell configurations at crossover experiment operating conditions (70°C, A: 40% RH, C: 100% RH, 50 kPa(g))

measured with anode and cathode stoichiometric ratios of 2 and 6 and therefore cannot be compared to the previous sections. These were the same flow rates that identified the noteworthy disparity between the BA/BA and BA/BC performances while generating the polarization curves in Figure 5.8.

Foremost, once again the cell with a single MPL exhibited higher crossover in the direction normal to the MPL than the cell without any MPLs. At a current density of 1750 mA/cm^2, both cell configurations have net water transport towards the anode. At a current density of 2400 mA/cm^2 however, the net flux across the BA/BA membrane reverses direction. The sudden drop in BA/BA cell potential noted in Figure 5.8 correlates with the change in the direction of the net flow of water. The net difference in crossover between the two cell configurations is equivalent to the BA/BA cell generating approximately 63% more water. Without an effective means to remove this additional water from the cathode, flooding was inevitable. The presence of an MPL appears to be critical in creating a driving force that moves water away from itself, which in this instance continued to facilitate net water transport towards the anode. Increased back diffusion allowed the BA/BC cell to achieve a higher current density before EOD became large enough to overcome the back diffusion.

Evidence of flooding is shown in Figure 5.11. The cell potential of the BA/BA cell at 2400 mA/cm^2 has far greater variability than the BA/BC cell at the same current density. This variability was attributed to liquid water momentarily disrupting reactant flow to the cathode catalyst layer. At this current density, the BA/BA cell was

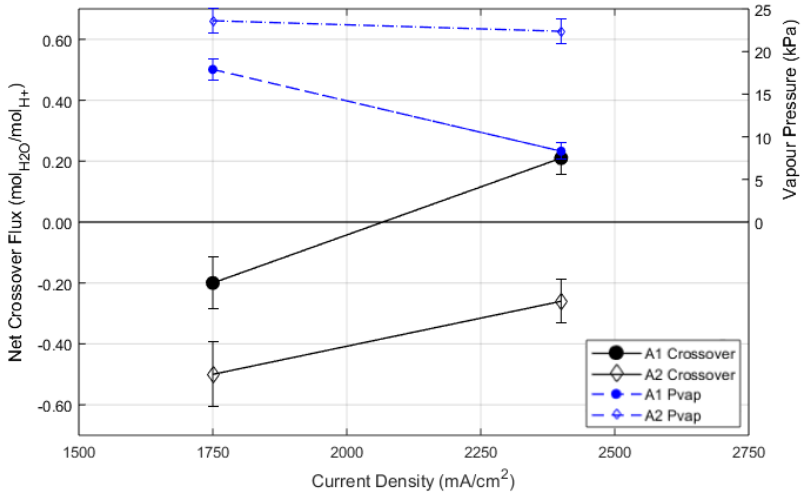

Figure 5.10 – Net crossover flux for BA/BA and BA/BC cell configurations at current densities where BA/BA and BA/BC cell performance deviates (70°C, A: 40% RH, C: 100% RH, 50 kPa(g))

struggling albeit managing to eject accumulated liquid water from the cathode porous media. The water balance setup captured a non-steady vapour pressure leaving the BA/BA cell's cathode and a transient spike in water content matches a similar spike in cell potential. All behaviour indicative of two phase flow resulting from electrode flooding.

Accompanying the reverse in flux is also a pronounced increase in cell resistance. Figure 5.9 shows both the BA/BA and BA/BC cells share the same low current resistance however, as the current density is increased, the BA/BA cell resistance spikes. This non-linear quasi-quadratic behaviour has been witnessed in all resistance plots, such as those shown in Figure 5.2. In every instance, this behaviour in cells without MPLs was more pronounced than those with at least one.

An increase in the cell resistance when the cell is flooding is contrary to the accepted understanding that membrane resistance decreases with absorbed water content [8]. Especially if there is liquid water in contact with the membrane as per Schröder's paradox. There is numerical evidence that suggests flooding which occurs in the catalyst layer shifts the reaction away from the membrane and towards the GDL/CL interface [24]. This adds protonic resistance proportional to the resistivity and thickness of the catalyst layer. Working in conjunction with this may be drying of the membrane at the anode membrane/CL interface. The average downstream vapour pressure of the anode measured for both cell configurations at 2400 mA/cm^2 was 8.31 kPa for the BA/BA cell build and 22.37 kPa for the BA/BC cell build. A

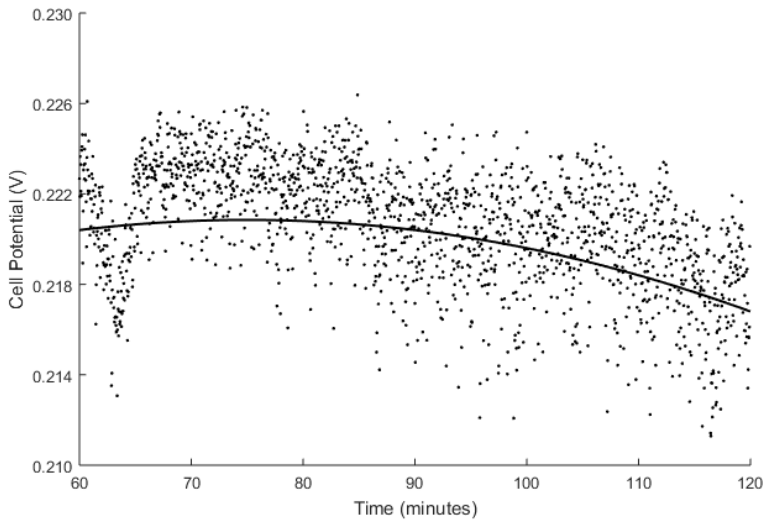

(a) BA/BA cell potential

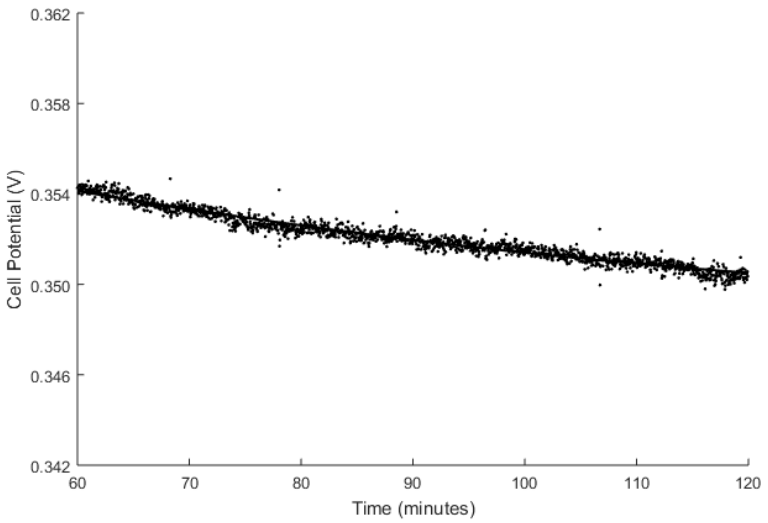

(b) BA/BC cell potential

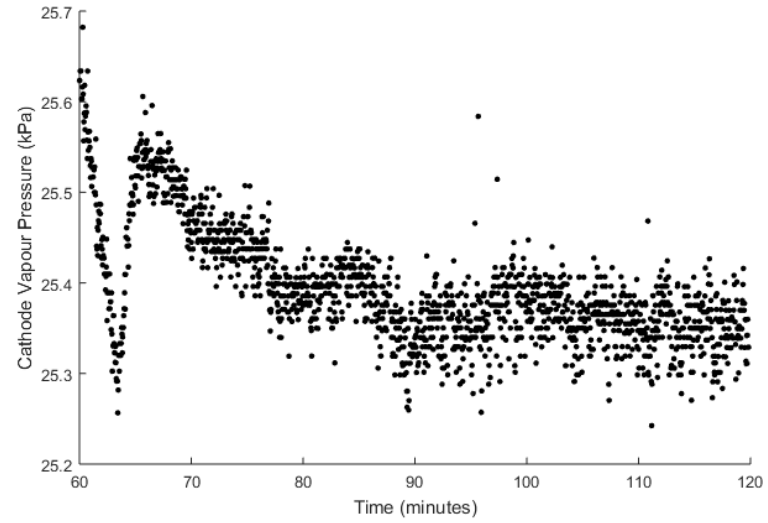

(c) BA/BA downstream cathode vapour pressure

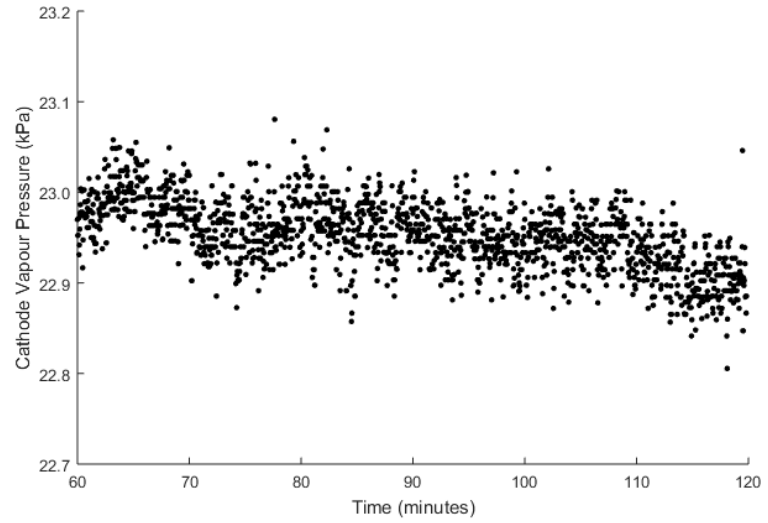

(d) BA/BC downstream cathode vapour pressure

Figure 5.11 – Cell behaviour of NR211 MEAs measured at 2400 mA/cm^2 demonstrating evidence of two-phase flow (70°C, A: 40% RH, C: 100% RH, 50 kPa(g))

humidity of 40% corresponds to an inlet vapour pressure of 12.48 kPa. A decrease in the vapour pressure along the flow field channel because of net water transport towards the cathode would result in a lower membrane water content and higher resistance near the anode membrane/CL interface. Maintaining a net flux towards the anode minimizes drying induced by EOD.

5.3 Conclusion

The initial intention of this study was to investigate the effects of an MPL on MEAs with varying membrane thickness. Results were mixed. Membranes upwards of 2.5 times thicker than those previously discussed in literature showed signs the MPL increases water transport away from the electrode its assembled with. However the narrative had to change in light of the higher than anticipated crossovers which fully saturated the gas leaving the anode, lending to the illusion 25.4 and 50.8 μm membranes had the same transport properties and the MPL did not modify water transport. When comparing to other crossover experiments especially those investigating thin membranes, flow rate is critical as the exhaust streams leaving a fuel cell can become saturated, adversely affecting results. Crossovers measured with a higher anode flow rate demonstrated 25.4 μm thick membranes are not a significant barrier to water transport and in agreeing with the previous conclusion, a single MPL does in fact increase water transport away from itself. This property impedes flooding of the cathode and prevents the membrane from drying out at the anode, allowing the cell to achieve higher current densities.

This is in agreement with most experimental publications investigating the effects of MPLs which conclude the MPL does increase water transport normal to itself and improves cell performance at high current densities by reducing water saturation in the GDL [6, 7, 24, 31, 42, 54, 74]. Other groups have extended their arguments to recognize water crossover is inversely proportional to membrane thickness [43, 49]. Atiyeh et al. [58] and Karan et al. [51], of the same research group, are widely acknowledged throughout recent articles of being the only publications unable to discern a statistically significant conclusion between the presence of an MPL and a change to the net crossover flux. A definitive reason for the difference in conclusions has not been determined.

Chapter 6

Conclusions & Future Work

Development of PEMFCs have transcended feasibility and now focuses on optimization and efficiency. One area garnering attention is understanding the transport of water throughout the cell. Water is critical in varying amounts for proton conductivity and reactant transport. Intelligent design of different cell components with the intention of managing water levels inside the cell can succeed in improving performance.

An over abundance of water inside a PEMFC contributes to premature performance losses as liquid water retained in the porous structures make the reactant pathways impassable, starving the reaction. Conversely, inadequate amounts of water reduces the proton conductivity of the catalyst layers and ionomer membrane, similarly dropping performance. An array of transport mechanisms shift water throughout the cell depending on hydraulic, thermal, concentration, or electrical potential gradients. Controlling the distribution of water throughout the cell requires an understanding of the different transport mechanisms and their net behaviour. The premise of this thesis was to provide the experimental means for the ESDLab to conduct research into water management to assist with the development of PEMFC numerical models.

6.1 Conclusions

The principal aim of this thesis was to design, develop, and validate a cost-effective experimental setup for downstream in situ measurements of the water distribution throughout an operational PEMFC. Rather than adopting the liquid water collection techniques commonly cited in literature, relative humidity, temperature, and pressure sensors were utilized to monitor the water content of a gas stream in the vapour phase. This sensor arrangement allows for real time capture of transient events and the identification of two-phase flow in addition to the same time-averaged behaviour

noted with conventional water collection.

The mixture of unused reactant and water vapour leaving both sides of a PEMFC are independently characterized by a Sensirion SHT75 relative humidity/temperature sensor and an OMEGA MM series pressure transducer housed in gas-tight stainless steel fittings that are externally heated above the cell temperature with a water bath. The sensors can only identify water in the vapour phase prompting the need for the gas to be heated prior to being measured. Bypass lines capable of re-directing gas flow around the cell allow case by case characterization of the water content of the gas provided by the test station. The net movement of water across the PEM can then be determined by a mass balance considering the water entering and leaving the anode of a PEMFC. Integrating the instantaneous measurements over the duration of the experiment provides the same results as conventional water collection. Momentary deviations away from a mean measurement correspond to liquid water ejection from the cell.

Real time measurements were a necessity for investigating the prevalence of two-phase flow and the transient cell response after exposure to a variety of step-changes. Realizing these advantages required sacrificing accuracy. Individual uncertainties associated with each measurand were characterized with auxiliary experiments and then propagated through the calculations process to quantify the overall uncertainty of the water balance setup. Because the vapour pressure was indirectly measured using multiple measurands, the individual uncertainties compounded, resulting in high overall uncertainties. The water content of a gas stream can be quantified to within $\pm 12.9\%$. A maximum achievable uncertainty of the net crossover flux cannot be surmised because it is dependent on the magnitude of the crossover and the operating conditions imposed on the cell. The subtraction arising from the mass balance applied to the anode creates a practical limit wherein the uncertainty approaches infinity as the net crossover approaches zero. For experimental conditions designed to create noticeable concentration gradients across the membrane, the uncertainty ranges from ± 15 - 35%. The largest contribution to the uncertainty is systematic, arising from manufacturer accuracies. Assuming bias uncertainties apply uniformly to all measurements, comparisons between identified trends would be subject to significantly smaller precision uncertainties.

Validation experiments were performed to realize the full potential of the setup. Foremost was to compare with conventional water collection. Humidified gas was fed directly from the test station, through the water balance setup, and then condensed with a forced air condensing unit. Taking the amount of condensed liquid water to be the control, the water balance setup routinely matched those amounts to within

± 1.3%. A second experiment was performed with the intended goal of reconciling the crossover measured by the anode with the same values based on the cathode. Measurements based on both sides of the cell were in agreement given their respective uncertainties. The last experiment was an attempt to reproduce experimental results previously published by Adachi et al. [54]. True replication of the tested MEAs and cell constructions was not possible, highlighted by differences in performance. Nevertheless, the crossovers measured with the water balance setup were of the same order of magnitude and in the same direction as those reported in literature. Further inspection of the real time measurements captured by the water balance setup revealed capricious spikes in the water content leaving the anode that correlated with changes in the cell potential, cell resistance, and internal pressure. Prior to developing the water balance setup, the cause of these transient events could only be speculated.

Through a comprehensive literature review, it was noted published experimental assessments of the effect of an MPL on water management have not considered membrane thickness. Using the water balance setup, an experiment, framed upon the work of Kim et al. [31] and Atiyeh et al. [58], investigated the change in the net crossover flux before and after the addition of an MPL. Three different Nafion membrane thicknesses were considered; NR211, NR212, and N115. Results indicate the addition of a single MPL to the cathode vastly improves high current performance by assisting the ejection of water from the cathode by increasing back diffusion to the anode. These advantages were seen for each membrane thickness with thinner membranes exhibiting higher crossovers and stronger performance. Furthermore, extrapolating non-PEM related resistances determined the addition of an MPL does not noticeably improve contact resistance between the catalyst layer and the GDL nor does it add additional electrical resistance. Contact resistance is primarily a function of cell compression.

6.1.1 Contributions

In conclusion, this thesis contributes to the following areas:

1. The development of a cost effective and accurate water balance setup for transient measurements of water fluxes from a PEMFC complete with a comprehensive uncertainty analysis to understand its accuracy

2. Experimental validation demonstrating the setup's functionality and confirming it can replicate established literature results

3. An investigation into the addition of an MPLs effect on water transport inside a PEMFC

6.2 Future Work

The water balance setup is currently fully operational however numerous improvements were noted throughout the development process that would improve the accuracy and functionality of the setup. This version of the water balance setup was a proof-of-concept prototype. The uncertainty analysis earmarked the Sensirion sensors as the largest contributor to measurement inaccuracies. Improved versions are available and were considered however a custom manufactured PCB and interfacing software were required, justifying the use of the older more supported sensors. Additional hardware improvements are explored in Appendix A.

Currently, the water content upstream of the fuel cell is characterized prior to any downstream measurements and assumed unchanged through the experimental duration. Steady state measurements of the water content directly from the test station support this conclusion however this limits the setup to steady state humidification operation. Introducing a second water balance setup upstream of the cell would allow additional experiments exploring the effects of upstream humidity to be performed.

The research potential for this setup is immense. Investigations into transient cell behaviour, quantifying water distributions under a variety of gradients, classifying operating conditions with a tendency for two-phase flow, and optimizing cell architecture to avoid flooding are but a sample of the experimental applications of the setup yet to be explored.

References

[1] James Larminie and Andrew Dicks. *"Fuel Cell Systems Explained 2nd Edition"*. Wiley, 2003.

[2] M. Warshay and P. Pokopius. "The fuel cell in space: yesterday, today, tomorrow". *Journal of Power Sources*, 29:193–200, 1990.

[3] Y. Wang, K.S. Chen, J. Mishler, S.C. Cho, and X.C. Ardoher. "A review of polymer electrolyte membrane fuel cells: Technology, applications, and needs on fundamental research". *Applied Energy*, 88:981–1007, 2011.

[4] M.S. Wilson, J.A. Valerio, and S. Gottesfeld. "Low Platinum Loading Electrodes for Polymer Electrolyte Fuel Cells Fabricated Using Thermoplastic Ionomers". *Electrochimica Acta*, 40(3):355–363, 1995.

[5] M. Blanco and D.P. Wilkinson. "Investigation of the effect of microporous layers on water management in a proton exchange membrane fuel cell using novel diagnostic methods". *International Journal of Hydrogen Energy*, 39:16390–16404, 2014.

[6] A.Z. Weber and J. Newman. "Effects of Microporous Layers in Polymer Electrolyte Fuel Cells". *Journal of the Electrochemical Society*, 152(4):A677–A688, 2005.

[7] J.T. Gostick, M.A. Ioannidis, M.W. Fowler, and M.D. Pritzker. "On the role of the microporous layer in PEMFC operation". *Electrochemistry Communications*, 11(3):576–579, 2009.

[8] A. Kusoglu and A.Z. Weber. "New Insights into Perfluorinated Sulfonic-Acid Ionomers". *Chemical Reviews*, 117(3):987–1104, 2017.

[9] M. Moore, A. Putz, and M. Secanell. "Investigation of the ORR Using the Double-Trap Intrinsic Kinetic Model". *Journal of The Electrochemical Society*, 160(6):F670–F681, 2013.

[10] A. Wilson, J. Marcinkoski, and D. Papageorgopoulos. Fuel cell system cost - 2016. Technical Report 16020, USA Department of Energy, 2016.

[11] N. Yousfi-Steiner, Ph. Moçotéguy, D. Candusso, D. Hissel, A. Hernandez, and A. Aslanides. "A Review on PEM voltage degradation associated with water management: Impacts, influent factors and characterization". *Journal of Power Sources*, 183:260–274, 2008.

[12] P.C. Rieke and N.E. Vanderborgh. "Temperature Dependence of Water Content and Proton Conductivity in Polyperfluorosulfonic Acid Membranes". *Journal of Membrane Science*, 32:313–328, 1987.

[13] T.A. Zawodzinski, C. Derouin, S. Radzinski, R.J. Sherman, V.T. Smith, T.E. Springer, and S. Gottesfeld. "Water Uptake by and Transport Through Nafion 117 Membranes". *Journal of the Electrochemical Society*, 140(4):1041–1047, 1993.

[14] G. Pourcelly, A. Oikonomou, and C. Gavach. "Influence of the water content on the kinetics of counter-ion transport in perfluorosulphonic membranes". *Journal of Electroanalytical Chemistry and Interfacial Electrochemistry*, 287(1):43–59, 1990.

[15] J. Zhang, Y. Tang, C. Song, Z. Xia, H. Li, H. Wang, and J. Zhang. "PEM fuel cell relative humidity (RH) and its effect on performance at high temperatures". *Electrochimica Acta*, 53:5315–5321, 2008.

[16] F.A. Uribe, T.E. Springer, and S.Gottesfeld. "A Microelectrode Study of Oxygen Reduction at the Platinum/Recast-Nafion Film Interface". *Journal of the Electrochemical Society*, 139(3):765–773, 1992.

[17] E. Endoh, S. Terazono, H. Widjaja, and Y. Takimoto. "Degradation Study of MEA for PEMFCs under Low Humidity Conditions". *Electrochemical and Solid-State Letters*, 7(7):A209–A211, 2004.

[18] C. Chen and T.F. Fuller. "The effect of humidity on the degradation of Nafion Membrane". *Polymer Degradation and Stability*, 94:1436–1447, 2009.

[19] M. Kim, N. Jung, K. Eom, S.J. Yoo, J.Y. Kim, J.H. Jang, H. Kim, B.K. Hong, and E. Cho. "Effects of anode flooding on the performance degradation of polymer electrolyte membrane fuel cells". *Journal of Power Sources*, 266:332–340, 2014.

[20] T.J. Mason, J. Millichamp, T.P. Neville, P.R. Shearing, S. Simons, and D.J.L. Brett. "A study of the effect of water management and electrode flooding on the dimensional change of polymer electrolyte fuel cells". *Journal of Power Sources*, 242:70–77, 2013.

[21] T.E. Springer, T.A. Zawodzinski, and S. Gottesfeld. "Polymer Electrolyte Fuel Cell Model". *Journal of the Electrochemical Society*, 138(8):2334–2342, 1991.

[22] J. Zhou, A. Putz, and M. Secanell. "A Mixed Wettability Pore Size Distribution Based Mathematical Model for Analyzing Two-Phase Flow in Porous Electrodes I. Mathematical Model". *Journal of the Electrochemical Society*, 164(6):F530–F539, 2017.

[23] J. Zhou, D. Stanier, A. Putz, and M. Secanell. "A Mixed Wettability Pore Size Distribution Based Mathematical Model for Analyzing Two-Phase Flow in Porous Electrodes II. Model Validation and Analysis of Micro-Structural Parameters". *Journal of the Electrochemical Society*, 164(6):F540–F556, 2017.

[24] J. Zhou, S. Shukla, A. Putz, and M. Secanell. "Analysis of the role of the microporous layer in improving polymer electrolyte fuel cell performance". *Electrochimica Acta*, 268:366–382, 2018.

[25] S. Shimpalee, U. Beuscher, and J. Van Zee. "Analysis of GDL flooding effects on PEMFC performance". *Electrochimica Acta*, 52(24):6748–6754, 2007.

[26] P. Staiti, Z. Poltarzewski, V. Alderucci, G. Maggio, N. Giordano, and A. Fasulo. "Influence of electrodic properties on water management in a solid poylmer electrolyte fuel cell". *Journal of Applied Electrochemistry*, 22:663–667, 1992.

[27] X. Liu, H. Guo, and C. Ma. "Water flooding and two-phase flow in cathode channels of proton exchange membrane fuel cells". *Journal of Power Sources*, 156(2):267–280, 2006.

[28] A. Mughal and X. Li. "Experimental diagnostics of PEM fuel cells". *Internation Journal of Environmental Studies*, 63(4):377–389, 2006.

[29] W. He, G. Lin, and T.V. Nguyen. "Diagnostic Tool to Detect Electrode Flooding in Proton-Exchange-Membrane Fuel Cells". *AIChE Journal*, 49(12):3221–3228, 2003.

[30] K. Tüber, D. Pócza, and C. Hebling. "Visualization of water buildup in the cathode of a transparent PEM fuel cell". *Journal of Power Sources*, 124:403–414, 2003.

[31] T. Kim, S. Lee, and H. Park. "A study of water transport as a function of the micro-porous layer arrangement in PEMFCs". *International Journal of Hydrogen Energy*, 35:8631–8643, 2010.

[32] J.P. Owejan, J.E. Owejan, W. Gu, T.A. Trabold, T.W. Tighe, and M.F. Mathias. "Water Transport Mechanisms in PEMFC Gas Diffusion Layers". *Journal of the Electrochemical Society*, 157(10):B1456–B1464, 2010.

[33] T.V. Nguyen. "A Gas Distributor Design for Proton-Exchange-Membrane Fuel Cells". *Journal of the Electrochemical Society*, 143(5):L103–L105, 1996.

[34] J. St-Pierre, D.P. Wilkinson, S. Knights, and M. Bos. "Relationships between water management, contamination and lifetime degradation in PEFC". *Journal of New Materials For Electrochemical Systems*, 3(2):99–106, 2000.

[35] F. Ettingshausen, J. Kleeman, A. Marcu, G. Toth, H. Fuess, and C. Roth. "Dissolution and Migration of Platinum in PEMFCs Investigated for Start/Stop Cycling and High Potential Degradation". *Fuel Cells*, 11(2):238–245, 2011.

[36] C.A. Rice, P. Urchaga, A.O. Pistono, B.W. McFerrin, B.T. McComb, and J. Hu. "Platinum Dissolution in Fuel Cell Electrodes: Enhanced Degradation from Surface Area Assessment in Automotive Accelerated Stress Tests". *Journal of the Electrochemical Society*, 162(10):F1175–F1180, 2015.

[37] T.A. Zawodzinski, J. Davey, J. Valerio, and S. Gottesfeld. "The Water Content Dependence of Electro-Osmotic Drag in Proton-Conducting Polymer Electrolytes". *Electrochimica Acta*, 40(3):297–302, 1995.

[38] T.F. Fuller and J. Newman. "Experimental Determination of the Transport Number of Water in Nafion-117 Membrane". *Journal of the Electrochemical Society*, 139(5):1332–1337, 1992.

[39] A. Husar, A. Higier, and H. Liu. "In situ measurements of water transfer due to different mechanisms in a proton exchange membrane fuel cell". *Journal of Power Sources*, 183:240–246, 2008.

[40] Q. Yan, H. Toghiani, and J. Wu. "Investigation of water transport through the membrane in a PEM fuel cell by water balance experiments". *Journal of Power Sources*, 158:316–325, 2006.

[41] S. Motupally, A.J. Becker, and J.W. Weidner. "Diffusion of Water in Nafion 115 Membranes". *Journal of the Electrochemical Society*, 147(9):3171–3177, 2000.

[42] T.C. Yau, M. Cimenti, X. Bi, and J. Stumper. "Effects of cathode gas diffusion layer design on polymer electrolyte membrane fuel cell water management and performance". *Journal of Power Sources*, 196:9437–9444, 2011.

[43] M. Adachi, T. Navessin, Z. Xie, F.H. Li, S. Tanaka, and S. Holdcroft. "Thickness dependence of water permeation through proton exchange membranes". *Journal of Membrane Science*, 364:183–193, 2010.

[44] T.C. Yau, P. Sauriol, X. Bi, and J. Stumper. "Experimental Determination of Water Transport in Polymer Electrolyte Membrane Fuel Cells". *Journal of the Electrochemical Society*, 157(9):B1310–B1320, 2010.

[45] T.C. Yau, M. Cimenti, X. Bi, and J. Stumper. "Water transport and Schröder's Paradox in fuel cell membrane electrode assemblies". *Journal of Power Sources*, 224:285–289, 2013.

[46] R. Zaffou, J.S. Yi, H.R. Kunz, and J.M. Fenton. "Temperature-Driven Water Transport Through Membrane Electrode Assembly of Proton Exchange Membrane Fuel Cells". *Electrochemical and Solid-State Letters*, 9(9):A418–A422, 2006.

[47] A. Thomas, G. Maranzana, S. Didierjean, J. Dillet, and O. Lottin. "Measurements of Electrode Temperatures, Heat and Water Fluxes in PEMFCs: Conclusions about Transfer Mechanisms". *Journal of the Electrochemical Society*, 160(2):F191–F204, 2013.

[48] A. Thomas, G. Maranzana, S. Didierjean, J. Dillet, and O. Lottin. "Thermal and water transfer in PEMFCs: Investigating the role of the microporous layer". *International Journal of Hydrogen Energy*, 39:2649–2658, 2014.

[49] G. Janssen and M. Overvelde. "Water transport in the proton-exchange-membrane fuel cell: Measurements of the effective drag coefficient". *Journal of Power Sources*, 101(1):117–125, 2001.

[50] T. Murahashi, M. Naiki, and E. Nishiyama. "Water transport in the proton exchange-membrane fuel cell: Comparison of model computation and measurements of effective drag". *Journal of Power Sources*, 162:1130–1136, 2006.

[51] K. Karan, H. Atiyeh, A. Phoenix, E. Halliop, J. Pharoah, and B. Peppley. "An Experimental Investigation of Water Transport in PEMFCs: The Role of Microporous Layers". *Electrochemical and Solid-State Letters*, 10(2):B34–B39, 2007.

[52] P. Sauriol, D.S. Nobes, X.T. Bi, J. Stumper, D. Jones, and D. Kiel. "Design and Validation of a Water Transfer Factor Measurement Apparatus for Proton Exchange Membrane Fuel Cells". *Journal of Fuel Cell Science and Technology*, 6:(041014) 1–13, 2009.

[53] B.S. Pivovar. "An overview of electro-osmosis in fuel cell polymer electrolytes". *Polymer*, 47(11):4194–4204, 2006.

[54] M. Adachi, T. Navessin, Z. Xie, B. Frisken, and S. Holdcroft. "Correlation of In Situ and Ex Situ Measurements of Water Permeation Through Nafion NRE211 Proton Exchange Membranes". *Journal of the Electrochemical Society*, 156(6):B782–B790, 2009.

[55] M. Adachi, T. Romero, T. Navessin, Z. Xie, Z. Shi, W. Merida, and S. Holdcroft. "Water Permeation Through Catalyst-Coated Membranes". *Electrochemical and Solid-State Letters*, 13(6):B51–B54, 2010.

[56] N. Zhao, D. Edwards, C. Lei, K. Wang, J. Li, Y. Zhang, S. Holdcroft, and Z. Shi. "The importance of water transport on short-side chain perfluorosulfonic acid membrane fuel cells operating under low relative humidity". *Journal of Power Sources*, 242:877–883, 2013.

[57] S. Ge, X. Li, B. Yi, and I. Hsing. "Absorption, Desorption, and Transport of Water in Polymer Electrolyte Membranes for Fuel Cells". *Journal of the Electrochemical Society*, 152(6):A1149–A1157, 2005.

[58] H.K. Atiyeh, K. Karan, B. Peppley, A. Phoenix, E. Halliop, and J. Pharoah. "Experimental investigation of the role of a microporous layer on the water transport and performance of a PEM fuel cell". *Journal of Power Sources*, 170:111–121, 2007.

[59] T. Colinart, A. Chenu, S. Didierjean, O. Lottin, and S. Besse. "Experimental study on water transport coefficient in Proton Exchange Membrane Fuel Cell". *Journal of Power Sources*, 190(2):230–240, 2009.

[60] X. Ye and C. Wang. "Measurement of Water Transport Properties Through Membrane-Electrode Assemblies I. Membranes". *Journal of the Electrochemical Society*, 154(7):B676–B682, 2007.

[61] X. Ye and C. Wang. "Measurement of Water Transport Properties Through Membrane-Electrode Assemblies Part II. Cathode Diffusion Media". *Journal of the Electrochemical Society*, 154(7):B683–B686, 2007.

[62] H. Li, Y. Tang, Z. Wang, Z. Shi, S. Wu, D. Song, J. Zhang, K. Fatih, J. Zhang, H. Wang, Z. Liu, R. Adouatallah, and A. Mazza. "A review of water flooding issues in the proton exchange membrane fuel cell". *Journal of Power Sources*, 178:103–117, 2008.

[63] W. Dai, H. Wang, X. Yuan, J.J. Martin, D. Yang, J. Qiao, and J. Ma. "A review on water balance in the membrane electrode assembly of proton exchange membrane fuel cells". *International Journal of Hydrogen Energy*, 34:9461–9478, 2009.

[64] Q. Zhao, P. Majsztrik, and J. Benziger. "Diffusion and Interfacial Transport of Water in Nafion". *The Journal of Physical Chemistry B*, 115(12):2717–2727, 2011.

[65] J. St-Pierre. "PEMFC In Situ Liquid-Water-Content Monitoring Status". *Journal of the Electrochemical Society*, 154(7):B724–B731, 2007.

[66] A.M. Niroumand and M. Saif. "Two-phase flow measurement system for polymer electrolyte fuel cells". *Journal of Power Sources*, 195:3250–3255, 2010.

[67] M.M. Mench, Q.L. Dong, and C.Y. Wang. "In situ water distributions measurements in a polymer electrolyte fuel cell". *Journal of Power Sources*, 124(1):90–98, 2003.

[68] Q. Dong, J. Kull, and M.M. Mench. "Real-time water distribution in a polymer electrolyte fuel cell". *Journal of Power Sources*, 139:106–114, 2005.

[69] J.P. Owejan, T.A. Trabold, D.L. Jacobson, M. Arif, and S.G. Kandlikar. "Effects of flow field and diffusion layer properties on water accumulation in a PEM fuel cell". *International Journal of Hydrogen Energy*, 32:4489–4502, 2007.

[70] R.J. Bellows, M.Y. Lin, M. Arif, A.K. Thompson, and D. Jacobson. "Neutron Imaging Technique for In Situ Measurement of Water Transport Gradients within

Nafion in Polymer Electrolyte Fuel Cells". *Journal of the Electrochemical Society*, 146(3):1099–1103, 1999.

[71] R. Satija, D.L. Jacobson, M. Arif, and S.A. Werner. "In situ neutron imaging technique for evaluation of water management systems in operating PEM fuel cells". *Journal of Power Sources*, 129:238–245, 2004.

[72] M. Breitwieser, R. Moroni, J. Schock, M. Schulz, B. Schillinger, F. Pfeiffer, R. Zengerle, and S. Thiele. "Water management in novel direct membrane deposition fuel cells under low humidification". *International Journal of Hydrogen Energy*, 41:11412–11417, 2016.

[73] M.A. Hickner, N.P. Siegel, K.S. Chen, D.N. McBrayer, D.S. Hussey, D.L. Jacobson, and M. Arif. "Real-Time Imaging of Liquid Water in an Operating Proton Exchange Membrane Fuel Cell". *Journal of the Electrochemical Society*, 153(5):A902–A908, 2006.

[74] D. Spernjak, A.K. Prasad, and S.G. Advani. "Experimental investigation of liquid water formation and transport in a transparent single-serpentine PEM fuel cell". *Journal of Power Sources*, 170(2):334–344, 2007.

[75] D. Malevich, E. Halliop, B.A. Peppley, and K. Karan J.G. Pharoah. "Investigation of Charge-Transfer and Mass-Transport Resistances in PEMFCs with Microporous Layer Using Electrochemical Impedance Spectroscopy". *Journal of the Electrochemical Society*, 156(2):B216–B224, 2009.

[76] R.P. Ramasamy, E.C. Kumbur, M.M. Mench, W. Liu, D. Moore, and M. Murthy. "Investigation of macro- and micro-porous layer interaction in polymer electrolyte fuel cells". *International Journal of Hydrogen Energy*, 33(13):3351–3367, 2008.

[77] T. Kitahara, T. Konomi, M. Murata, N. Berg, and P.M. Wilde. "Influences of Gas Diffusion Layer Design Parameters on the Performance of Polymer Electrolyte Fuel Cells". *ECS Transactions*, 5(1):27–36, 2007.

[78] J. Chen, T. Matsuura, and M. Hori. "Novel gas diffusion layer with water management function for PEMFC". *Journal of Power Sources*, 131:155–161, 2004.

[79] U. Pasaogullari, C. Wang, and K.S. Chen. "Two-Phase Transport in Polymer Electrolyte Fuel Cells with Bilayer Cathode Gas Diffusion Media". *Journal of the Electrochemical Society*, 152(8):A1574–A1582, 2005.

[80] J.G. Pharoah, B.A. Peppley, H. Atiyeh, E. Halliop, K. Karan, and A. Phoenix. "Investigating the Role of a Microporous layer on the Water Transport and Performance of a PEMFC". *ECS Transactions*, 3(1):1227–1237, 2006.

[81] S. Shukla, K. Domican, K. Karan, S. Bhattacharjee, and M. Secanell. "Analysis of Low Platinum Loading Thin Polymer Electrolyte Fuel Cell Electrodes Prepared by Inkjet Printing". *Electrochimica Acta*, 156:289–300, 2015.

[82] S. Shukla, D. Stanier, M.S. Saha, J. Stumper, and M. Secanell. "Analysis of Inkjet Printed PEFC Electrodes with Varying Platinum Loading". *Journal of the Electrochemical Society*, 163(7):F677–F687, 2016.

[83] Shantanu Shukla. *Experimental analysis of inkjet printed polymer electrolyte fuel cell electrodes*. PhD thesis, University of Alberta, 2016.

[84] A.L. Buck. "New Equations for Computing Vapor Pressure and Enhancement Factor". *Journal of Applied Meteorology*, 20(12):1527–1532, 1981.

[85] Buck Research Intruments LLC. *"Model CR-1A Hydrometer with Autofill Operating Manual - Appendix 1: Humidity Conversion Equations"*, May 2012.

[86] X. Yuan, S. Zhang, J.C. Sun, and H. Wang. "A review of accelerated conditioning for a polymer electrolyte membrane fuel cell". *Journal of Power Sources*, 196(22):9097–9106, 2011.

[87] K.R. Cooper and M. Smith. "Electrical test methods for on-line fuel cell ohmic resistance measurement". *Journal of Power Sources*, 160(2):1088–1095, 2006.

[88] Anthony J. Wheeler and Ahmad R. Ganji. *"Introduction to Engineering Experimentation 2nd Edition"*. Prentice Hall, 2004.

[89] John R. Taylor. *"An Introduction to Error Analysis: The Study of Uncertainties in Physical Measurements 2nd Edition"*. University Science Books, 1997.

[90] L. Greenspan. "Humidity Fixed Points of Binary Saturated Aqueous Solutions". *Journal of Research of the National Bureau of Standards - A. Physics and Chemistry*, 81A(1):89–96, 1977.

[91] R. Schweiss, C. Meiser, T. Damjanovic, I. Galbati, and N. Haak. *"SIGRACET® Gas Diffusion Layers for PEM Fuel Cells, Electrolyzers and Batteries"*. SGL CARBON GmbH, www.sglgroup.com/cms/international/products/product-groups/su/fuel-cell-components/index.html?__locale=en, August 2016.

[92] J. Peron, A. Mani, X. Zhao, D. Edwards, M. Adachi, T. Soboleva, Z. Shi, Z. Xie, T. Navessin, and S. Holdcroft. "Properties of Nafion ®NR-211 membranes for PEMFCs". *Journal of Membrane Science*, 356(1-2):44–51, 2010.

[93] C. Beal. "The Viscosity of Air, Water, Natural Gas, Crude Oil and Its Associated Gases at Oil Field Temperatures and Pressures". *Transactions of the AIME*, 165(1):94–115, 1946.

[94] J.P. Holman. *Heat Transfer Tenth Edition*. McGraw Hill Higher Education, 2010.

[95] K.R. Cooper. "In Situ PEMFC Fuel Crossover & Electrical Short Circuit Measurement". *Fuel Cell Magazine*, 8(Aug/Sep), 2008.

[96] M. Schoemaker, U. Misz, P. Beckhaus, and A. Heinzel. "Evaluation of Hydrogen Crossover through Fuel Cell Membranes". *Fuel Cells*, 14(3):412–415, 2014.

[97] K.R. Cooper. "In Situ PEM Fuel Cell Electrochemical Surface Area and Catalyst Utilization Measurement". *Fuel Cell Magazine*, 9(Jan/Feb), 2009.

Appendix A

Setup Improvements

Considerable time and effort was allocated towards improving the accuracy, resolution, and reliability of the water balance setup. The development process was organic, constantly changing based on how the setup operated and the outcome of different experimental results. This appendix documents the work already invested into this area before it was ultimately put on hold due to time constraints.

Consideration of the individual contributions to the overall uncertainty of the setup (equation (3.37)) confirmed the vapour pressure, and therefore the SHT75 sensors, should be earmarked for improvement to achieve the most efficient gains in accuracy. The latest development from Sensirion is the SHT35, intended as a more accurate replacement for the SHT75. A side by side comparison of the two sensors is summarized in Table A.1.

Revising the uncertainty analysis in Section 3.1 with the SHT35 specifications reduces the relative uncertainty of the vapour pressure by approximately 62%. With only this improvement, the overall uncertainty of water content measured by the setup would improve by a factor of 2.

Despite the obvious benefits, the decision to proceed with the SHT75 was based in part because the SHT75 sensors arrive from the manufacturer already mounted onto a PCB and accompanied with a bug-free communication software complete with a live-feed of the sensor measurements. In contrast, the SHT35 is shipped as a chip,

Table A.1 – Sensirion relative humidity/temperature sensor comparison

Specification	**SHT75**	**SHT35**
Operational RH Accuracy	± 2.0 %	± 1.8 %
Operational Temp. Accuracy	± 1.3°C	± 0.2°C
Comments	PCB mounted /w software	Requires custom mounting & software

Table A.2 – TE Connectivity pressure sensor specifications

Specification	OMEGA MM Series	MS5803-01BA07
Pressure Range	± 200 kPa	± 120 kPa
Accuracy	± 0.1 kPa	± 0.5 kPa
Max Operating Temp.	105°C	125°C
Comments	Waterproof	Water Tight
Volume	≈ 20.0 cm^3	0.11 cm^3

requiring a custom PCB design and I^2C communication program.

The necessity for a custom PCB presented the opportunity for including a board mountable I^2C pressure sensor. The advantages of this design would be simultaneous pressure, temperature, and relative humidity measurements recorded at the same location, a single communication program for interfacing with all the sensors, and a reduction in the overall cost of the measurement equipment.

Notable factors influencing the selection of a pressure sensor included a maximum size limited by the space available inside the sensor housing and on the PCB shared with the SHT35 sensor, the range of measurable pressures, capacity to operate in warm humid environments, and the cost. This led to the selection of an MS5803-01BA miniature variometer module from TE Connectivity. Specifications for the pressure sensor are summarized in Table A.2.

Development of the PCB and communication software was in partnership with Rick Conrad of University of Alberta's Mechanical Engineering Electronics Department. Communication was established with several working prototypes. A picture of an operational sensor board is shown in Figure A.1. The surface area of the board is approximately 100 mm^2. The Electronics Department retains the manufacturing drawings for the PCB and software code for interacting with the sensors.

The feed throughs were unchanged with the exception of a different connector. Power and ground were shared between the sensors and each had their own I^2C circuits. The feed throughs were then connected to a Teensy 3.2 USB development board that facilitated communication between the computer and sensors. With this setup, uncertainty analysis and some experimental validation was able to be performed with promising results. Water collection performed with the prototype sensor board agreed to within 0.6% (Table A.3). However chronic communication reliability issues prevented the PCB design from being fully implemented.

Possible explanations for the communication issues included operating near the extreme ends of the sensors specifications (85°C) causing physical damage to the internal structure of the sensors, moisture accumulation causing electrical shorts, and

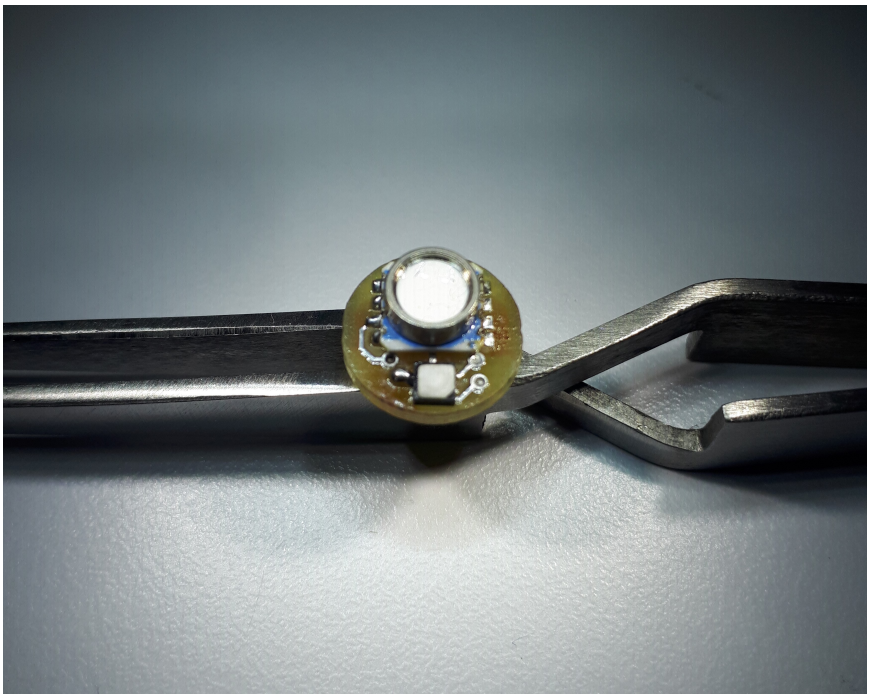

Figure A.1 – Prototype of custom PCB assembled with SHT35 and MS5803-01BA sensors

thermal expansion causing electrical contacts to crack or de-laminate from the PCB. In some instances, communication could be restored by leaving the sensors overnight, suggesting they can recover provided they have an opportunity to dry thoroughly and cool down.

Addressing each of the possible causes sequentially, operating at lower temperatures ($\approx 70°C$) did not alleviate the sensor failures. Nor did coating all the electrical contacts with a dielectric grease. It has since been speculated that thermal cycles caused the soldered junctions to either crack, creep, or otherwise shift resulting in a loss of connectivity. In some cases, resetting the sensors after a brief exposure to hot air temporarily restored communication suggesting poor connectivity at the PCB junctions. Communication was often lost shortly after re-exposure to the hot humid gas inside the sensor housing.

Table A.3 – Prototype sensor board water collection results

	Amount
Prediction	139.59 g
Measurements	139.68 g
Collected	138.79 g

Improving upon the soldered junctions is difficult. The equipment available in the Electronics Department is insufficient to follow the strict soldering instructions, such as prescribed temperature ramps and hold times, outlined by each manufacturer. Furthermore, the size of the sensors complicates the assembly process.

Further development of the sensor board is required before the benefits of the improved setup can be realized. TE Connectivity has recently released an improved version of their MS5803 series pressure sensors that are unfortunately only available in large bulk quantities. The MS5803-01BA07 offers improved reliability in extreme condition with only minor sacrifices in accuracy as can be seen in Table A.2. Adopting this pressure sensor would address any shortcomings associated with high temperatures and humidities. Alternatively, Sensirion intends to release a PCB mounted SHT35 with a compatible software sometime in late 2018-early 2019.

Appendix B

Residence Time

The sampling rate of the sensors was set to match the approximate resident time of the gas inside the sensor housing, illustrated in Figure B.1. It is best described as a cylinder with an inner diameter of 18 mm and a length of 56.5 mm, with the sensors positioned in the middle of the cylinder, immersed in the streamlines, and extending 5 mm from the cylinder wall.

The Reynolds number, determining the flow regime, was then found using the following equation,

$$\mathrm{Re} = \frac{\rho v d}{\mu} \tag{B.1}$$

where ρ is the density of the gas, v is the velocity, d is the cylinder diameter, and μ is the viscosity. Because the flow rate is prescribed in standard litres per minute, slpm, the dependency of the velocity and density on the temperature and pressure compensate each other (note, despite its nomenclature, standard litres per minute are always corrected to a standard temperature and pressure and are therefore a unit of mass flow rate not volume flow rate). Equation (B.1) can then be simplified knowing,

$$v = \frac{\dot{V}}{A}\frac{T}{T_o}\frac{P_o}{P_\infty} \tag{B.2}$$

$$A = \frac{\pi d^2}{4} \tag{B.3}$$

$$\rho = \frac{P_\infty M}{RT} \tag{B.4}$$

where $\dot{V}$ is the flow rate in slpm, P_∞ is the local pressure, T is the local temperature, M is the molar mass of the gas, and P_o and T_o are the standard conditions of the flow controllers, to

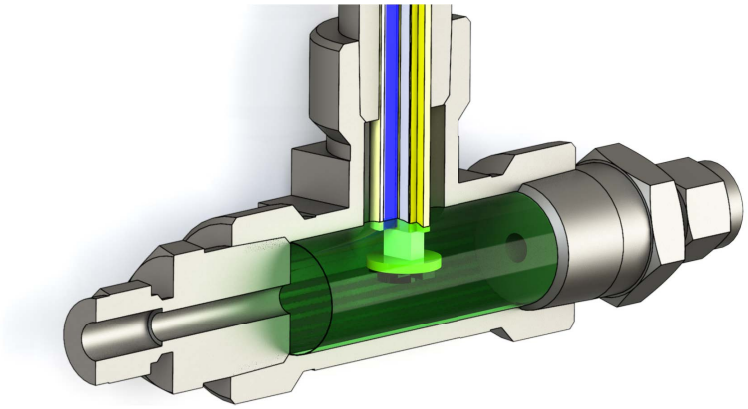

Figure B.1 – Section view of feed through. Green shaded area is approximation of the sensor control volume

$$\mathrm{Re} = \frac{4M\dot{V}P_o}{\pi dR\mu T_o} \tag{B.5}$$

Given those dimensions and the expected operational limits, the highest Reynolds number that can be achieved will occur when air is passing through the cathode at 1.75 slpm. Viscosity increases as temperature drops and pressure increases (albeit to a negligible degree). Therefore the highest viscosity would be expected when the system is operating at a pressure of 100 kPa(g) and 65°C which C. Beal [93] determined for air to be 18.08×10^{-6} Pa·s. This calculates to be a Reynolds number of 147 which is well below 2300, indicating the flow to be laminar [94]. For the anode, the flow rate is much lower and the working gas is hydrogen, so it can be concluded the anode is also well within the laminar flow regime. As such, there is no mixing between streamlines. The resident time can then be found from equation (B.6).

From observation, the shortest resident time will occur at high flow rates and temperatures and at low pressures, corresponding to 0.4 slpm, 85°C and 91 kPa(a) respectively. Given those conditions, the residence time will always be greater than,

$$t = \frac{l}{v} = l\,\frac{A}{\dot{V}}\frac{T_o}{T}\frac{P_\infty}{P_o} \geq 1.48 \text{ sec} \tag{B.6}$$

A sampling rate of one second is therefore sufficient to capture, at minimum, one measurement for each transient event that passes the sensors. For long duration experiments, such as those in Chapters 4 and 5, a sampling rate of one second is memory intensive. Equation (B.6) can be used to estimate more appropriate sampling times. Another notable set of operating conditions is 0.4 slpm, 70°C, and 140 kPa(a). At these conditions, a sampling rate of two seconds is sufficient.

Appendix C

Characterization Protocols

Unless mentioned otherwise, these are the protocols used to characterize every cell assembled as part of this work. All tests were performed with a Scribner 850e Fuel Cell Test Station.

Extrapolating Hydrogen Crossover from a CV

A common method of measuring hydrogen crossover is to use linear sweep voltammetry (LSV) [95]. The cathode, acting as the working electrode, is purged with an inert gas such as nitrogen and then exposed to a sweep of potentials that would instantaneously oxidize hydrogen. Any measurable current is then attributed to the presence of hydrogen in the cathode that is reasonably assumed to have crossed the membrane from the anode. MEAs in good condition exhibit a limiting current driven by the hydrogen permeability of the membrane whereas an increasing current indicates the presence of a hole. The flux of hydrogen crossing the membrane, $J_{H_2,crossover}$, is then calculated as per,

$$J_{H_2,crossover}\ [\text{mol/cm}^2\ \text{s}] = \frac{i_{lim}}{nF} \tag{C.1}$$

where i_{lim} is the limiting current density, n is the number of electrons released as part of the reaction (2 for hydrogen oxidation), and F is Faraday's constant.

Cyclic voltammetry differs from LSV in that the potential is cycled from 0 to 1.2 V and returned to 0 V. This complete profile of potentials captures different adsorption and desorption processes on the catalyst surface, one of which is discussed later to approximate the electrochemical surface area. However none of these processes occur near a potential of 0.4 V [96]. It is assumed any faradiac current generated by the cell at this potential arises from the hydrogen oxidation reaction occurring at the cathode. To determine the hydrogen crossover from a CV, the average current between the front and back voltage sweep measured at 0.4 V is taken to be the limiting

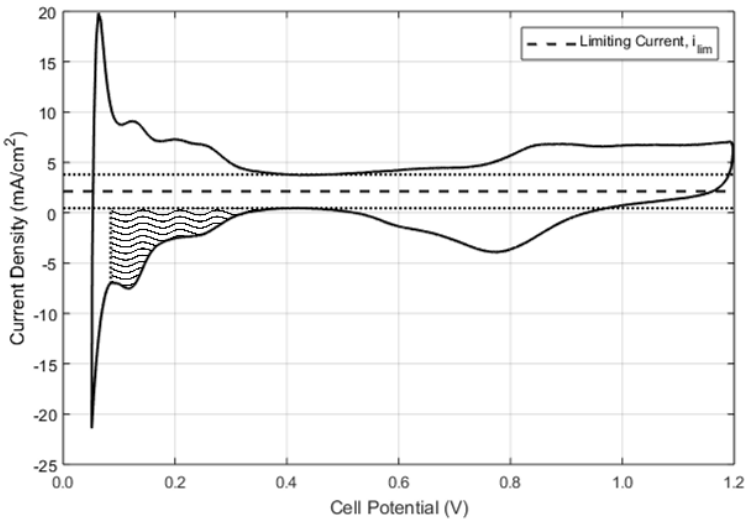

Figure C.1 – CV illustrating regions used to calculate hydrogen crossover and ECSA

current, i_{lim}, from equation (C.1). An example can be seen in Figure C.1.

Extrapolating ECSA from a CV

The electrochemical surface area (ECSA) can be approximated by noting the capacitive charge required for hydrogen to adsorb onto platinum activation sites [97],

$$Pt - H_{ads} \leftrightharpoons Pt + H^+ + e^- \tag{C.2}$$

This adsorption reaction occurs as the potential is cycled from high to low potentials. The corresponding region is indicated by the etching in Figure C.1. It is vertically bounded by the same current density measured at 0.4 V corresponding to the double layer charging of the working electrode. The lower potential limit is defined by the peak prior to the asymptotic drop in current density which corresponds to a change in the reaction from the hydrogen adsorption to hydrogen evolution. The ECSA is calculated as per,

$$ECSA\ [\mathrm{cm}^2_{Pt}/\mathrm{g}_{Pt}] = \frac{Q_{Pt}}{(0.210\ \mathrm{mC/cm}^2_{Pt})\ w_{Pt}\ \delta} \tag{C.3}$$

where Q_{pt} is the hydrogen adsorption charge calculated from the integral of the area etched in Figure C.1, 0.210 mC/cm$^2_{Pt}$ is the charge required to adsorb protons on platinum, w_{Pt} is the platinum loading of the electrode, and δ is the voltage scan rate of the CV.

Table C.1 – Standard ESDLab Conditioning Protocol

Operating Condition	**Values**
Cell Temperature	80 °C
Anode Humidity	80%
Cathode Humidity	80%
Anode Flow Rate	Hydrogen @ 0.2 slpm
Cathode Flow Rate	Air @ 0.4 slpm
Back Pressure	0 kPa(g)
Applied Current	1 hr @ 0.02 A/cm^2
OCV	30 sec
Applied Current	1 hr @ 0.02 A/cm^2
OCV	30 sec
Applied Current	1 hr @ 0.05 A/cm^2
OCV	30 sec
Applied Current	1 hr @ 0.05 A/cm^2
OCV	30 sec
Applied Current	1 hr @ 0.1 A/cm^2
OCV	30 sec
Applied Current	1 hr @ 0.1 A/cm^2
OCV	30 sec
Applied Current	1 hr @ 0.2 A/cm^2
OCV	30 sec
Applied Current	1 hr @ 0.2 A/cm^2
OCV	30 sec
Applied Current	1 hr @ 0.4 A/cm^2
OCV	30 sec
Applied Current	1 hr @ 0.4 A/cm^2
OCV	30 sec
Anode Flow Rate	0.3 slpm
Cathode Flow Rate	0.6 slpm
Applied Current	1 hr @ 0.7 A/cm^2
OCV	30 sec
Applied Current	1 hr @ 0.7 A/cm^2
OCV	30 sec
Applied Current	1 hr @ 0.9 A/cm^2
OCV	30 sec
Applied Current	1 hr @ 0.9 A/cm^2
OCV	30 sec
Applied Current	1 hr @ 1.0 A/cm^2
OCV	30 sec
Applied Current	1 hr @ 1.0 A/cm^2
OCV	30 sec

Table C.2 – Standard ESDLab Polarization Curve Protocol

Operating Condition	**Values**
Cell Temperature	80 °C
Minimum Anode Flow Rate	Hydrogen @ 0.2 slpm
Anode Stoich Ratio	Wet 2.0
Minimum Cathode Flow Rate	Air @ 0.4 slpm
Cathode Stoich Ratio	Wet 6.0
Back Pressure	50 kPa(g)
Repeat three times	
Anode Humidity	50%
Cathode Humidity	50%
Scan Current	0.1 A/pt, 45 sec/pt
	Reverse Scan @ 0.2 V
Repeat three times	
Anode Humidity	70%
Cathode Humidity	70%
Scan Current	0.15 A/pt, 45 sec/pt
	Reverse Scan @ 0.2 V
Repeat three times	
Anode Humidity	90%
Cathode Humidity	90%
Scan Current	0.2 A/pt, 45 sec/pt
	Reverse Scan @ 0.2 V

Table C.3 – Standard ESDLab CV Protocol

Operating Condition	**Values**
Cell Temperature	30 °C
Anode Humidity	100%
Cathode Humidity	100%
Anode Flow Rate	Hydrogen @ 0.2 slpm
Cathode Flow Rate	Nitrogen @ 0.005 slpm
Back Pressure	0 kPa(g)
Repeat ten times	
Potential Range	0 V to 1.2 V
Scan Rate	40 mV/s
Current Range	2 A

Appendix D

Calibration Documents

OMEGA ENGINEERING INC.

PRESSURE TRANSDUCER
FINAL CALIBRATION

0.00 - 100.00 KPAA
Excitation 24.000 Vdc

Job: WHS0022121 Serial: 488638
Model: MMA015V10K2C0T4A6CE Tested By: GRS
Date: 3/27/2018 Temperature Range: -40 to +220
Calibrated: 0.00 - 100.00 KPAA Specfile: MMV10A

Pressure KPAA	Unit Data Vdc
0.00	0.022
50.00	5.012
100.00	10.004
50.00	5.012
0.00	0.021

Balance 0.022 Vdc
Sensitivity 9.982 Vdc

ELECTRICAL LEAKAGE: PASS
PRESSURE CONNECTION/FITTING: 1/4-18 NPT Male
ELECTRICAL WIRING/CONNECTOR: BLACK = - EXCITATION
WHITE = + OUTPUT
GREEN = N/C
RED = + EXCITATION

This Calibration was performed using Instruments and Standards that are traceable to the United States National Institute of Standards Technology.

S/N	Description	Range	Reference	Cal Cert
1047	PPC3 30 PSI AUTO	0 - 100.00 KPAA	C-1954	C-1954
US37001431	Agilent 34970A	Unit Under Test	C-2445	C-2445

Q.A. Representative : *Gary Smith* Date: 3/27/2018

This transducer is tested to & meets published specifications. After final calibration our products are stored in a controlled stock room & considered in bonded storage. Depending on environment & severity of use factory calibration is recommended every one to three years after initial service installation date.

Omega Engineering Inc., One Omega Drive, Stamford, CT 06907
http://www.omega.com email: info@omega.com phone (800) 826-6342

OMEGA ENGINEERING INC.

PRESSURE TRANSDUCER
FINAL CALIBRATION

0.00 - 200.00 KPAA
Excitation 24.000 Vdc

Job: WHS0022345 Serial: 490111
Model: MMA030V10K2C0T4A6CE Tested By: LDG
Date: 4/5/2018 Temperature Range: -40 to +220
Calibrated: 0.00 - 200.00 KPAA Specfile: MMV10A

Pressure KPAA	Unit Data Vdc
0.00	0.000
100.00	5.003
200.00	10.009
100.00	5.003
0.00	0.000

Balance 0.000 Vdc
Sensitivity 10.009 Vdc

ELECTRICAL LEAKAGE: PASS
PRESSURE CONNECTION/FITTING: 1/4-18 NPT Male
ELECTRICAL WIRING/CONNECTOR: BLACK = - EXCITATION
WHITE = + OUTPUT
GREEN = N/C
RED = + EXCITATION

This Calibration was performed using Instruments and Standards that are traceable to the United States National Institute of Standards Technology.

S/N	Description	Range	Reference	Cal Cert
1047	PPC3 30 PSI AUTO	0 - 200.00 KPAA	C-1954	C-1954
US37001431	Agilent 34970A	Unit Under Test	C-2445	C-2445

Q.A. Representative : *Larry Gaedrich* Date: 4/5/2018

This transducer is tested to & meets published specifications. After final calibration our products are stored in a controlled stock room & considered in bonded storage. Depending on environment & severity of use factory calibration is recommended every one to three years after initial service installation date.

Omega Engineering Inc., One Omega Drive, Stamford, CT 06907
http://www.omega.com email: info@omega.com phone (800) 826-6342